Drop Formation from axi-symmetric fluid jets

Theo Driessen

Drop formation from axi-symmetric fluid jets

Theo Driessen

Samenstelling promotiecommissie:

Voorzitter:	prof. dr. G. van der Steenhoven
Promotor:	prof. dr. D. Lohse
Copromotor:	prof. dr. F. Toschi (TU/e)
Assistent-Promotor:	dr. ir. R. Jeurissen (TU/e)
Leden:	prof. I. Hutchings (University of Cambridge)
	prof. dr. J. Benschop
	prof. dr. J. F. Dijksman
Referent:	dr. ir. H. Wijshoff (Océ Technologies B.V.)
Deskundige:	Ir. H. Reinten (Océ Technologies B.V.)

This research has been co-financed by the Dutch ministry of economical affairs, Limburg Province, Overijssel Province, Noord-Brabant Province, the partnership region Eindhoven and by Océ Technologies NV. This research was done at the research and development department of Océ, at the Physics of Fluids group at the University of Twente, and at the Fluid Dynamics Lab at the Eindhoven University of technology.

Nederlandse titel: Druppelvorming uit axi-symmetrische vloeistof jets

Publisher:
Theo Driessen, Physics of Fluids, University of Twente,
P.O. box 217, 7500 AE Enschede, the Netherlands
pof.tnw.utwente.nl

Cover illustration: Snapshot of drop formation of 4 successive actuations in a drop-on-demand setup. Simulation data by Theo Driessen, 3D rendering by Wolter van de Velde.
Print: Gildeprint

ISBN 978-90-365-3578-6

DROP FORMATION FROM AXI-SYMMETRIC FLUID JETS

PROEFSCHRIFT

ter verkrijging van
de graad van doctor aan de Universiteit Twente,
op gezag van de rector magnificus,
Prof. Dr. H. Brinksma,
volgens besluit van het College voor Promoties
in het openbaar te verdedigen
op vrijdag 20 december 2013 om 16.45 uur

door

Theodorus Wilhelmus Driessen
geboren op 14 december 1984
te Deurne

Dit proefschrift is goedgekeurd door de promotor:

Prof. dr. rer. nat. Detlef Lohse

de co-promotor:

Prof. dr. Federico Toschi

en de assistent promotor:

Dr. ir. Roger Jeurissen

Contents

1 | Introduction

The research in this thesis is directed towards a better understanding of droplet formation in inkjet printing. Inkjet printing technology was initially developed and used for the digital printing of text and images. Recently, this technology has been introduced in many other applications, e.g. in the production of solar cells [1], and in the fabrication of 3D printed biological tissue [2], to name a few. For these applications, one goes to the extreme: smaller and faster droplets, using complex fluids that may contain particles or living cells. For the development of these new applications of inkjet printing, understanding of the drop formation process is essential. The experiments at small length scale, combined with fast dynamics, become challenging. Therefore, numerical models are important tools for the development of the new printing applications. This thesis is a step in the direction of understanding the drop formation under these extreme conditions.

The two most common forms of inkjet printing are "Continuous inkjet" and "Drop on Demand" (DoD) inkjet [3]. The main focus of this thesis is on the drop formation in piezo actuated DoD inkjet printing, in which a piezo actuator is used for the droplet generation. The piezoelectric actuator transforms an electrical signal into a pressure wave in the ink, which travels towards the nozzle. At the nozzle, the ink is accelerated by this pressure wave, forming an ink jet. The ejection velocity of the ink scales with the amplitude of the actuation signal. For high speed DoD inkjet printing, the challenge is to achieve large droplet velocities, while maintaining control over the drop formation. The details of the DoD inkjet operation can be found in the review article by Herman Wijshoff [3].

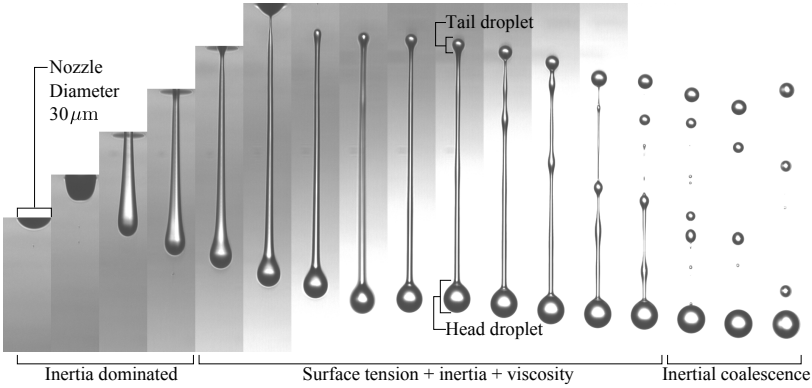

Figure 1.1: The genesis of a ink droplet ejected from a nozzle with a diameter of 30 μm at a speed of 25m/s. This figure shows single flash recordings of separate droplets, generated from the same nozzle with the same actuation pulse. To visualize the droplet evolution, the delay between the actuation pulse and the recording increases for each snapshot. The ink has a viscosity ten times larger than that of water. Just after the ink is ejected, inertia dominates. Later, surface tension and viscosity are relevant for the drop contraction and break-up. The filament finally breaks up into several unequally sized droplets due to the Rayleigh-Plateau instability. The experimental data for this figure was provided by Marc van den Berg.

1.1 Drop formation in DoD inkjet printing

After the ejection of the jet, and before the droplets hit the substrate, the drop formation process can be divided into two regimes. The first regime is governed by inertia, whereas the second is governed by a balance between inertia and surface tension with a minor contribution of the viscosity (see figure 1.1). The velocity gradient causes a substantial elongation of the jet in the former regime. In the latter regime, the filament starts to deform due to surface tension. The effect of surface tension can be seen from the formation of tail droplets and the breakup of the filament due to the Rayleigh-Plateau instability [4]. The viscosity stabilizes the contraction and the Rayleigh-Plateau instability [5].

Typical jetting velocities in inkjet printing are in approximately 10 meter per second, whereas the relevant length scales can be smaller than a micrometer. To accurately measure the droplet dynamics, high-speed high-resolution photography is needed, which is challenging.

For the investigation of drop formation, we use a hydrodynamic model whose origin goes back as far as to Lord Rayleigh [6]. This model provides insights into the dynamics that are not accessible from an experimental point of view. Furthermore, it is very useful to be able to predict the drop formation of a newly designed printhead. The challenge for such a hydrodynamic model is the pinchoff singularity which occurs whenever the jet radius goes to zero. This pinchoff singularity was ascribed in detail by Jens Eggers in [7]. In this thesis, we present and use a novel implementation of the hydrodynamic model, in which we regularize the singular events by a modification of the surface tension term.

1.2 Guide through the thesis

This thesis has been organized in the following way:

In chapter 2 we present a new numerical implementation of the slender jet approximation [8]. In this implementation, we introduce a regularization term to remove the pinchoff singularity. The new regularized model can successfully simulate the evolution of a liquid jet beyond the first pinchoff.

In chapter 3 we determine the contraction velocity of a viscous ligament. The results of the analysis are obtained using four different methods, namely a force balance method, the lattice Boltzmann method, a volume of fluid model (FLOW3D), and the numerical model presented in chapter 2. From the analysis, we conclude that the contraction velocity of the viscous filament is given by $u_\sigma = \sqrt{\sigma/(\rho R_0)}$.

In chapter 4 we develop a theory for the stability of the viscous filament. We find that the transition to unstable filaments is governed by end pinching for low viscous filaments, and by the Rayleigh-Plateau instability for more viscous filaments. For the latter transition, the initial distortion of the filament surface is a relevant parameter.

In chapter 5 we demonstrate an experimental method to measure the fluid velocity inside a flying inkjet droplet. The determined velocity is validated using our numerical model, presented in chapter 2

In chapter 6 we present a method to generate a stream of widely-spaced droplets. We perturb a continuous liquid jet with two Rayleigh-Plateau-unstable modes simultaneously. The interference pattern of the two growing modes induces coalescence after the jet breaks up into small droplets. The final droplet spacing is given by the shortest common wavelength of the two distortions. We demonstrate that the droplet evolution is governed solely by the two distortions at the nozzle, using a quantitative comparison with the numerical model of chapter 2.

The thesis ends with general conclusions and an outlook to further work.

2 | Axisymmetric drop formation model*

The breakup of an axisymmetric viscous jet is considered in the lubrication approximation. The discretized equations are solved on a fixed equidistant one-dimensional Eulerian grid. The governing equations are implemented in a conservative second order accurate TVD scheme, preventing the numerical diffusivity. Singularities that occur at pinchoff and coalescence are regularized by a small modification on the surface tension. The modification is of the order of the spatial step Δx. This regularization ensures that the solution of the presented numerical model converges to the exact solution of the breakup of a jet in the lubrication approximation.

2.1 Introduction

The breakup of laminar jets is applied in many different industries to generate droplets ([9]). Some fields of application are: inkjet printing ([3]), mono disperse powder production ([10]) and localized drug delivery in the human body ([11]). These industrial applications generally demand control over the droplet properties. The properties of the resulting droplets are controlled by tuning the flow characteristics at the nozzle, such as the flow rate, the nozzle shape and size, and the liquid properties. Numerical models are used to tune the design parameters of the droplet production systems. The objective is to induce droplet

*Published as: Theo Driessen and Roger Jeurissen, "A regularised one-dimensional drop formation and coalescence model using a total variation diminishing (TVD) scheme on a single Eulerian grid", Int. J. Comp. Fluid Dyn. **25**, 333-343 (2011).

pinchoff at the right place and at the right time, and to let unwanted smaller droplets coalesce with the larger ones. Both coalescence and pinchoff are essential phenomena in these applications, but these phenomena are notoriously difficult to incorporate in a numerical model ([8] and [12]).

In the usual approximation, where a continuum with a sharp interface is assumed, a singularity develops at every pinchoff and at every coalescence. These singularities have been studied extensively ([5]). The velocity diverges as the radius at the thinnest point goes to zero. Due to the Courant-Friedrich-Lewy (CFL) condition of the temporal step size, these singularities cannot be simulated within a finite number of time steps. In a numerical model, these singularities require special treatment. There is ample recent research on the treatment of these singularities. Full 3D numerical models such as the Volume Of Fluid method ([13]), or 2D axi symmetric VOF method ([14]), and the Level set method ([15],[16]) are capable of representing the free surface dynamics. The 1D axisymmetrical lubrication approximation of the dynamics of slender jets has proved to be sufficiently accurate in many applications ([8], [17], [18], [19] and [20]), for the evolution of the system between singularities.

In order to calculate the evolution of a system that contains singular events, the flow between these singularities must be calculated. When a singularity occurs, the system state after the singularity must be inferred from the system state before the singularity. The distinction between the evolution between singularities and the evolution across singularities is arbitrary, but it is made explicitly in existing numerical models based on the lubrication approximation ([18], [8] and [17]). This distinction implies that the model should know at what radius a droplet breaks up. Furthermore, a choice should be made to define the curvature at the end of the droplet. Since the pinchoff can display a variety of shapes on different length scales, [21], the choice of curvature right after pinchoff can be difficult.

At the transfer of the system state over the singularity, the mass and momentum are chosen to be conserved in the presented model. Instead of treating the singularities as discrete points in time and space, they are regularized by a small modification of the momentum flux. This regularization limits the length- and time scale of the singularities from below. By refining the grid, the solution converges towards the exact solution of the non regularized system.

2.2 Integral formulation

The dynamics of an axisymmetric free surface jet can be calculated accurately in the lubrication approximation. The existing numerical models use the lubrication approximation derived in [[8]].

$$\partial_t R = -u\partial_x R - \frac{1}{2}R\partial_x u, \tag{2.1a}$$

$$\partial_t u = -u\partial_x u - \frac{1}{\rho}\partial_x P_{Lap} + 3\nu\partial_x(R^2\partial_x u)R^{-2}, \tag{2.1b}$$

$$P_{Lap} = \sigma\left\{R^{-1}[1+(\partial_x R)^2]^{-1/2} - [1+(\partial_x R)^2]^{-3/2}\partial_x^2 R\right\},$$

where R is the radius, u is the axial velocity, x is the axial coordinate, t is the time, P_{Lap} is the Laplace pressure, σ is the surface tension, ρ is the density, and ν is the kinematic viscosity. The solutions to these equations are singular at each pinchoff ([8]), and at each collision of liquid bodies.

It is desirable to construct a numerical model that converges to an exact solution of a physical system, including the singularity that occurs at pinchoff and coalescence. To obtain a solution that converges, point wise, to the exact solution, it is essential to use a conservative numerical scheme ([12]). A conservation equation of a hyperbolic system of equations is given by a time derivative of the conserved quantity, and the spatial derivative of the flux of the conserved quantity.

$$\partial_t a(x,t) + \partial_x f\left(a(x,t)\right) = 0, \tag{2.2}$$

where a is the conserved quantity, and $f\left(a(x,t)\right)$ is the flux function of this conserved quantity. Equation 2.1a is rewritten to conservative form, by multiplying the balance with πR on both sides:

$$\partial_t(\rho A) + \partial_x(\rho u A) = 0. \tag{2.3}$$

Equation 2.1b is integrated over the cross section of the jet, to obtain the conservation of momentum equation. The differential form of the conservation of momentum is

$$\partial_t(\rho A u) + \partial_x(\rho A u^2) = \partial_x(\tau_\mu + \tau_\sigma) \tag{2.4}$$

where A is the cross sectional area of the jet, and the sum of the viscous tension τ_μ and capillary tension τ_σ is the momentum flux due

to capillary interaction. The viscous tension τ_μ is given by

$$\tau_\mu = 3\mu A \partial_x u, \tag{2.5}$$

where μ is the dynamic viscosity. The capillary tension τ_σ is given by the integral of the capillary stress over the cross sectional area. To obtain the conservative form, this integral is rewritten as a momentum flux. This flux is given by the sum of the Laplace pressure integrated over the cross sectional area, and the force exerted on the contour of the jet in the axial direction,

$$\partial_x \tau_\sigma = \partial_x \left\{ A P_{Lap} - \sigma 2\pi R [1 + (\partial_x R)^2]^{-1/2} \right\}. \tag{2.6}$$

These equations govern the evolution of a slender axisymmetric liquid body.

2.2.1 Regularization

To allow the described physical system to transfer across the singularities that occur at pinchoff and coalescence, the surface tension term is regularized by a modification at radii of the order of the cutoff radius R_c. The cutoff radius is a control parameter of the regularization, and is chosen to scale with the spatial step.

$$R_c \sim \Delta x \tag{2.7}$$

Due to the regularization, the capillary tension goes to a finite value when the jet radius goes to zero. The finite capillary tension allows a stable liquid column between the free floating liquid bodies, since the surface minimization is now bounded from below. When the spatial step goes to zero, the radius at which the regularization kicks in is reduced so that the solution of the regularized system converges to the analytical solution.

The regularization is implemented on the entire domain. The capillary tension term τ_σ is replaced by a weighted average between the physical capillary tension τ_σ and a cutoff capillary tension τ_c.

$$\tau_{\sigma reg} = R(R + R_c)^{-1} \tau_\sigma + R_c (R + R_c)^{-1} \tau_c, \tag{2.8}$$

where the cutoff capillary tension $\tau_c = -\sigma \pi R_c$ is the surface tension in a cylinder with a radius equal to the cutoff radius R_c. The cutoff radius

R_c scales with the spatial step, hence the influence of the regularization vanishes as the spatial step goes to zero. When the $R \gg R_c$, the regularized capillary tension behaves like the physical capillary tension. In the case of $R \ll R_c$, the regularized capillary tension behaves like the constant capillary tension of a liquid column of radius R_c.

Since the cell width in a simulation is not infinitesimal; and since the radius of the stable cylinder scales with the grid size, the radius of the stable column remains finite. Hence a body of fluid, traveling through the one dimensional grid, is connected to the stable cylinder outside the fluid. A finite force of magnitude τ_c is exerted on both sides of the liquid body by the regularization, in opposite directions. The connection between the liquid body and the stable cylinder induces waves in the stable column. Since the finite force τ_c scales with (Δx), the influence of these regularization artifacts on the main dynamics vanishes quickly.

2.2.2 Integral formulation

With all forces and fluxes defined, the governing equations can be written in integral form. First, we rewrite the momentum equation, equation 2.4, to separate $\partial_t u$ term from the $\partial_t(uA)$, such that the result of the simulation contains an array for $A(x)$ and an array for $u(x)$.

$$A\partial_t u = -\partial_x A u^2 - u\partial_t A + \frac{1}{\rho}\partial_x(\tau_\mu + \tau_\sigma). \tag{2.9}$$

Now the integral forms of the conservation equations for mass and momentum are

$$\int_{\Delta x} \partial_t A \,\mathrm{d}x = -[Au]_{\Delta x} \tag{2.10a}$$

$$\int_{\Delta x} (A\partial_t u)\,\mathrm{d}x = -[Au^2]_{\Delta x} - \int_{\Delta x} u\partial_t A \,\mathrm{d}x + \frac{1}{\rho}[\tau_\mu + \tau_\sigma]_{\Delta x}, \tag{2.10b}$$

where Δ_x is the cell width after discretization. At the sides of the integration domain, the fluxes are well defined. In the next section, it is shown how these equations can be implemented in a conservative numerical scheme.

2.3 Numerical implementation

The singularities that occur at pinchoff are regularized in the governing equations. As a result, the problem in the numerical implementation is not the handling of the singularities. The solution of the numerical model converges to the exact solution with singularities, hence large velocity gradients are to be expected. Therefore, numerical diffusivity should be limited in order to allow the physical viscosity to dominate the approach of the singularity. A single fixed Eulerian grid is used, since it allows a straightforward implementation of the conservation laws. Since the grid does not move with the free floating bodies, the velocity gradients at the sides of the liquid bodies will be large. A second order accurate scheme is necessary to prevent numerical diffusivity.

The tension terms can be implemented by a standard central differencing scheme, since they do not depend on the direction of the flow. Using central differencing to evaluate the mass and momentum flux will introduce unphysical oscillations. A TVD scheme with a flux limiter prevents the unwanted oscillations, and still gives a second order accurate result ([12]).

2.3.1 Discretization

The liquid jet is discretized on a staggered one dimensional finite volume grid, see figure 2.1. The cross section of the jet is approximated by a series of functions that are piecewise constant on intervals centered on the integer nodes x_i. The base functions of the momentum are similarly centered at $x_{i+1/2}$. By the mass and velocity approximations, the momentum in a momentum cell, $P_{i+1/2}$, are precisely determined.

$$P_{i+1/2} = \rho \frac{1}{2}(A_i + A_{i+1})u_{i+1/2} \tag{2.11}$$

The discretization contains the necessary information on the correct locations, therefore, no interpolation of velocities is necessary for the calculation of the advective fluxes.

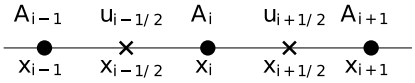

Figure 2.1: A sketch of the staggered grid.

2.3.2 Implementation of the tension terms

The forces that act on the mass cell are discretized by a central differencing scheme. The discrete viscous tension is given by

$$\tau_{\mu,i} = 3\mu A_i \frac{\vec{u}_{i-\frac{1}{2}} - \vec{u}_{i+\frac{1}{2}}}{\Delta x} \tag{2.12}$$

The discrete capillary tension before regularization is given by

$$\tau_{\sigma,i} = \sigma\pi \left\{ -R_i \left[1 + (\partial_x R_i)^2\right]^{-1/2} - R_i^2 \left[1 + (\partial_x R_i)^2\right]^{-3/2} \partial_x^2 R_i \right\} \tag{2.13}$$

where the curvature and slopes are found by a standard central differencing scheme.

2.3.3 Implementation of the fluxes

The method used in the presented numerical model is a Total Variation Diminishing (TVD) scheme using flux limiters to prevent the numerical oscillations. The mathematical background of the TVD scheme can be found in ([12]). For this research, the most important fact is that a second order TVD scheme is monotonicity preserving, because the cross-sectional area is a positive definite quantity.

The implementation of the TVD scheme on the volume flux is described here. The implementation of the momentum flux is analogous. The volume flux F in the governing equations is given by

$$F = uA. \tag{2.14}$$

For the implementation of the TVD scheme, the first order upwind flux

and the central differencing flux are determined first.

$$F_{\text{upwind},i+\frac{1}{2}} = \begin{cases} u_{i+\frac{1}{2}} A_i & (u_{i+\frac{1}{2}} < 0) \\ \\ u_{i+\frac{1}{2}} A_{i+1} & (u_{i+\frac{1}{2}} > 0) \end{cases}, \tag{2.15}$$

$$F_{\text{central},i+\frac{1}{2}} = \frac{1}{2} u_{i+\frac{1}{2}} \left(A_i + A_{i+1} \right). \tag{2.16}$$

A ratio Θ is constructed to quantify the smoothness of the solution for the mass distribution. If the interface on the left of the cell, towards negative position, is upwind, Θ_i is

$$\Theta_i = \frac{A_i - A_{i-1}}{A_{i+1} - A_i}. \tag{2.17}$$

If the interface on the right of the cell, towards positive position, is upwind, Θ_i is

$$\Theta_i = \frac{A_{i+1} - A_i}{A_i - A_{i-1}}. \tag{2.18}$$

When both neighboring cells are upwind, $\Theta_i = 0$ is chosen. When both slopes vanish, Θ_i is undetermined by the equations above, and $\Theta_i = 0$ is chosen. The ratio for the gradient, Θ, is used for the flux limiter function. The flux limiter ψ is a function of the smoothness ratio in the cell that is upwind of the interface where the flux is to be determined. The flux limiter ψ is defined at each cell interface. The flux limiter has to be continuous in $[\psi, \Theta] = 1$ for second order accuracy, and preferably continuously differentiable. The van Leer limiter meets both requirements. The van Leer flux limiter is given by:

$$\psi = \frac{|\Theta_{\text{upwind}}| + \Theta_{\text{upwind}}}{1 + |\Theta_{\text{upwind}}|}, \tag{2.19}$$

as shown in figure 2.2. The second order accurate TVD mass flux is now found by using the flux limiter as a regulator for the upwind, downwind and central differencing flux.

$$F_{i+\frac{1}{2}} = F_{\text{upwind},i+\frac{1}{2}} - \psi \left(F_{\text{upwind},i+\frac{1}{2}} - F_{\text{central},i+\frac{1}{2}} \right) \tag{2.20}$$

Combined with the momentum flux, which is calculated in a similar way, and the tension, the dynamics of the axisymmetric liquid jet with a flat flow profile can now be calculated with second order accuracy.

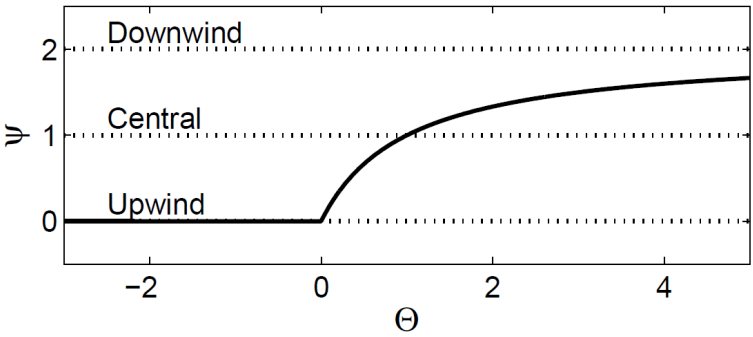

Figure 2.2: The van Leer flux limiter. This flux limiter is smooth and continuously differentiable in $[\psi, \Theta] = 1$*. When the solution is smooth* $(\Theta = 1)$*, the flux limiter selects central differencing. For negative values of the smoothness, the flux limiter* ψ *selects the downwind flux, whereas for large positive values of the smoothness, the flux limiter* ψ *chooses the upwind flux.*

2.4 Validation

To assess the validity of the numerical model, we compare the calculated results with exact solutions and experimental results. First, the steady state of the regularized system is validated. When the regularization is implemented correctly, the solution converges to the analytical solution for decreasing cell width. Then the dynamics of the model are validated by the use of the Rayleigh-Plateau instability. The Rayleigh-Plateau instability has been studied for many years, which makes it a suitable benchmark case. An example of a Rayleigh-Plateau instability is shown in figure 2.3.

2.4.1 Steady states

The influence of the regularization on the governing equations is investigated by examining the steady states. Surface tension is the driving force of the governing equations. In a steady state, the capillary tension is constant. In a steady state, the capillary tension is constant

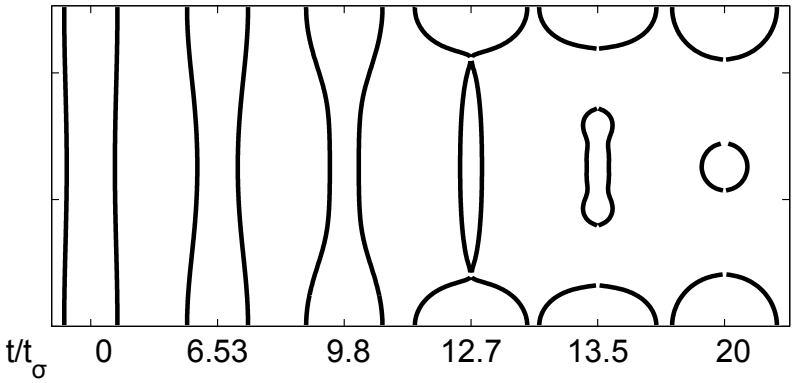

Figure 2.3: Example of an evolution of the Rayleigh-Plateau instability for an Ohnesorge number $Oh = 0.1$ for $\chi = \sqrt{1/2}$. Only the parts of the solution with a radius larger than R_c are displayed. Due to the Rayleigh-Plateau instability, the cylinder breaks up into separate droplets. At the chosen parameter values, multiple droplet sizes result. The largest is called the main droplet. The second largest is dubbed the satellite droplet. Even smaller droplets might also arise, but these are smaller than R_c, so that they are not plotted in this figure.

and imposing a constant capillary tension in the regularized governing equations yields an ODE in the radius

$$\begin{aligned} \partial_x^2 R &= -\frac{\left(\frac{\tau_c}{\pi\sigma} + \frac{R_c^2}{R+R_c}\right)\frac{R+R_c}{R} + R\lambda}{R^2\lambda^3} \\ \lambda &= \frac{1}{\sqrt{1+(\partial_x R)^2}} \\ \tau_c &= \sigma\pi R_c. \end{aligned} \tag{2.21}$$

The initial values for a sphere are $R(x=0)=1$ and $\partial_x R(x=0)=0$. This results in an initial value problem of the radius as a function of axial position. This initial value problem is solved with the Dormand-Prince Runge Kutta solver, of which the results are shown in figure 2.4. The points in $x=|1|$ are singular points of the exact solution. These singular points in the exact solution result in a neck in the regularized approximation, which connects to another sphere adjacent to the first. The radius of the neck connecting the spheres scales with R_c. The calculated steady states converge point wise to the exact solution as the cutoff radius R_c goes to zero.

2.4.2 Rayleigh-Plateau instability

The Rayleigh-Plateau instability is used to validate the dynamics of the numerical model. The onset of the Rayleigh-Plateau instability can be analyzed with a linear stability analysis, and there is ample experimental work on the evolution and final state of the phenomenon ([22], [23], [24], [25] and [26]). The dispersion relation of a growing perturbation in the linear regime is compared to the analytical solution. Furthermore, the calculated final droplet sizes of the Rayleigh-Plateau instability are compared to existing experimental and numerical results.

In the next section, the initial conditions for a symmetric Rayleigh-Plateau instability are derived for the regularized governing equations. In the existing literature on the modeling of a Rayleigh-Plateau instability, it is customary to find the growth rate of the instability in the small amplitude domain. As an initial condition generally the radius is perturbed by a small amplitude sinusoid ([22], [27], [8], [19] and [28]). In the linear regime, where the perturbation amplitude is still small, the perturbation in the radius is coupled with a perturbation in the velocity. The relation between the perturbation in the radius and in

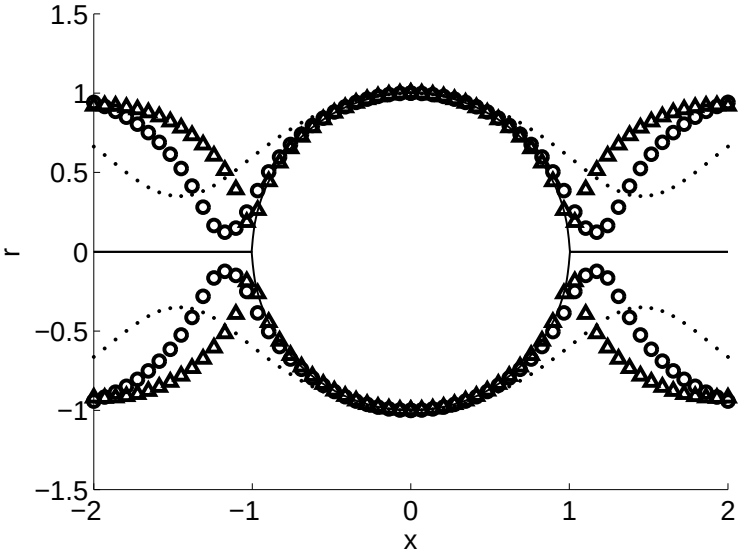

Figure 2.4: Steady state solution of the radius versus axial position, exact solution (solid line) and regularized approximations for decreasing values of R_c. The exact solution is a sphere of radius $R = 1$. The values of the regularization radius R_c are 0.5 (•), 0.2 (∘) and 0.01 (△). On the interval $-1 < x < 1$, the regularized approximation of the steady state converges to the exact solution as the cutoff radius R_c goes to zero.

the velocity is defined by the eigenvectors of the linearized governing equations. For the validation of the model, it is convenient to use an initial condition for which an analytical solution is available.

We distinguish between a symmetric Rayleigh-Plateau instability, which is easier to analyze analytically, and an asymmetric Rayleigh-Plateau instability, which is easier to generate experimentally and is the more relevant situation in current technical applications. Whether the Rayleigh-Plateau instability is symmetric, asymmetric, or just traveling waves, depends on the imposed disturbance in the velocity and radius. This is specified by the complex wave number of the initial

disturbance. The other parameter of the problem is the dimensionless viscosity, the Ohnesorge number. The Ohnesorge number is defined by $Oh = \mu/\sqrt{\rho\sigma R_0}$. For the validation of the numerical method, the symmetric Rayleigh-Plateau instability is used. An example of a symmetric Rayleigh-Plateau instability evolution is shown in figure 2.3. Due to the fact that the model is 1 dimensional, the double cone structure that is found for a low viscosity pinchoff ($Oh < 0.1$), cannot be resolved with the presented model.

2.4.3 Linear analysis of a Rayleigh-Plateau instability

The onset of the Rayleigh-Plateau instability can be calculated analytically using a linearization. The solution to the linearized problem gives the eigenvalues and eigenvectors in the limit of small perturbation amplitudes. The eigenvalues give the wavenumber dependent growth rates, and the corresponding eigenvectors give the relations between the perturbation in the radius and in the velocity. The parameters of the governing equations are non dimensionalized as follows:

Time:$\theta = t/t_\sigma$ with $t_\sigma = \sqrt{\rho R_0^3/\sigma}$	Space: $\chi = x/R_0$.
Radius: $r = R/R_0$	Velocity: $v = ut_\sigma/R_0$

In the case of small amplitude perturbations, the gradients are small: $\partial_\chi r \ll 1$. The non dimensional governing equations in the small amplitude approximation are given by ([5], paragraph 3.5.1):

$$\partial_\theta r^2 = -\partial_\chi \left(r^2 v\right), \tag{2.22a}$$

$$\partial_\theta \left(r^2 v\right) = 3Oh\partial_\chi \left(r^2 \partial_\chi v\right) - \partial_\chi \left(r + r^2 \partial_\chi^2 r\right). \tag{2.22b}$$

These equations are linearized using small perturbations on the dimensionless radius and velocity: $\tilde{r} < \epsilon \ll 1$ and $\tilde{v} < \epsilon \ll 1$. The perturbed dimensionless radius and velocity are then given by $r = 1 + \tilde{r}$ and $v = \tilde{v}$. Substituting the perturbed radius and velocity in the governing equations then gives

$$\partial_\theta \tilde{r} = -\frac{1}{2}\partial_\chi \left(\tilde{v}\right) \tag{2.23a}$$

$$\partial_\theta \tilde{v} = 3Oh\partial_\chi^2 \tilde{v} - \left(\partial_\chi \tilde{r} + \partial_\chi^3 \tilde{r}\right). \tag{2.23b}$$

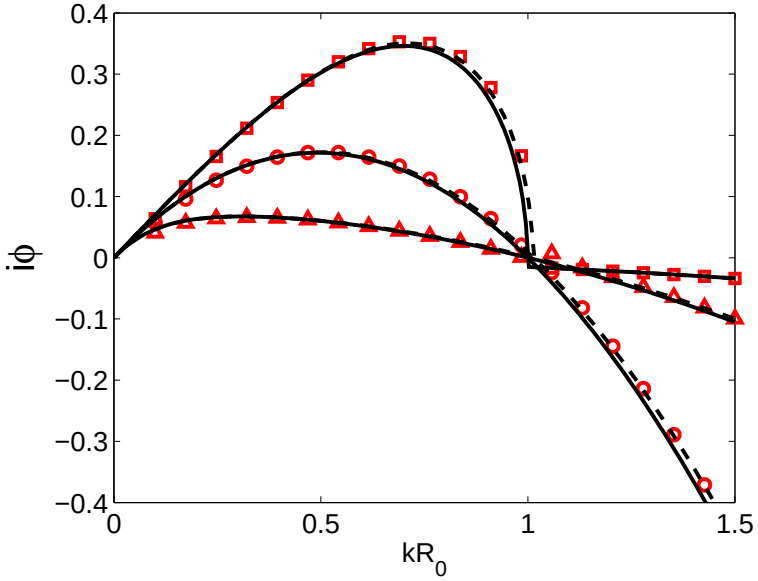

Figure 2.5: Dimensionless growth rate of a viscous Rayleigh-Plateau instability as a function of the dimensionless wavenumber for different Ohnesorge numbers. The exact solution is shown by the solid line, the dashed line represents the exact solution of the regularized model for 150 nodes. The symbols indicate the result of the growth rate calculated with the numerical model for given grid size. The different Ohnesorge numbers are given by: $Oh(\square) = 0.01$, $Oh(\circ) = 0.5$, $Oh(\triangle) = 2$. The result of the simulation coincide with the exact solution of the regularized system. This exact solution in turn agrees with the exact solution of the Rayleigh-Plateau instability for the fastest growing wavelengths. The regularization influences for what value of the non dimensional wavenumber the eigenvalue crosses zero, which will be shown quantitatively in figure 2.7.

Now we can make an Ansatz for the perturbations in radius and velocity: $\tilde{r} = \tilde{r}_a e^{i(\chi\chi+\phi\theta)}$ and $\tilde{v} = \tilde{v}_a e^{i(\chi\chi+\phi\theta)}$, where $\chi = kR_0$ is the dimensionless wavenumber and $\phi = \omega t_\sigma$ is the dimensionless frequency. Subscript 'a' denotes amplitude. The right hand side of the linearized equations (equations 2.23a and 2.23b) are rewritten to the frequency domain,

$$\partial_\theta \tilde{r}_a = -\frac{i\chi}{2}\tilde{v}_a \tag{2.24a}$$

$$\partial_\theta \tilde{v}_a = -3Oh\chi^2\tilde{v}_a + i\left(-\chi\tilde{r}_a + \chi^3\tilde{r}_a\right). \tag{2.24b}$$

Write this system of equations in matrix form:

$$i\phi \begin{bmatrix} \tilde{r_a} \\ \tilde{v_a} \end{bmatrix} = \begin{bmatrix} 0 & -\frac{i\chi}{2} \\ -i(\chi-\chi^3) & -3Oh\chi^2 \end{bmatrix} \begin{bmatrix} \tilde{r_a} \\ \tilde{v_a} \end{bmatrix} \tag{2.25}$$

The eigenvalues of the matrix on the right hand side are the dimensionless growthrate multiplied by i:

$$i\phi_\pm = -\frac{3}{2}Oh\chi^2 \pm \left[\frac{9}{4}Oh^2\chi^4 + \frac{1}{2}(\chi^2-\chi^4)\right]^{\frac{1}{2}}. \tag{2.26}$$

Note that both the positive and negative root of the surface tension part of the solution are physically possible. One can impose a growing or a decreasing Rayleigh-Plateau instability, by changing the phase in the perturbation on the radius and the velocity. When the negative root is chosen, the perturbation will exactly cancel out in $t = \infty$ in the theoretical case without viscosity and in the absence of other perturbations due to any source of noise. The perturbation will be growing when the positive root is chosen. The eigenvectors satisfy the relation

$$2i\phi_\pm\tilde{r}_a - i\chi\tilde{v}_a = 0, \tag{2.27}$$

which is the relation between the amplitude in the radial perturbation and the amplitude in the perturbation on the velocity. This solution is complex. In order to obtain a physically relevant solution, we impose the condition that the solution is real. Since the equation is linear, two solutions can be added to obtain another solution. By choosing two solutions that are each others' complex conjugate, we obtain a real valued solution. Choosing the positive root, the well known growing Rayleigh-Plateau instability is found.

$$2i\phi_+\tilde{r}_a cos(\chi\chi) - i\chi\tilde{v}_a sin(\chi\chi) = 0. \tag{2.28}$$

Dimensionless wavenumber $[kR_0]$	Main droplet size $[\frac{R_{main}}{R_0}]$	Satellite droplet size $[\frac{R_{sat}}{R_0}]$
0.2	2.53	1.94
0.3	2.31	1.51
0.4	2.16	1.18
0.5	2.06	0.91
0.6	1.96	0.66
0.7	1.88	0.47
0.8	1.80	0.33
0.9	1.74	0.22

Table 2.1: Relative final droplet sizes as function of the dimensionless wavenumber for $Oh^{-1} = 10$.

The surface tension is regularized in the model; hence the eigenvalues and eigenvectors are derived also for the regularized equations. The results of the model converge towards the regularized solution with decreasing Δx, and at the same time the regularized solution converges to the analytical solution due to the decreasing R_c. The eigenvalues and eigenvector for the regularized system can be derived in the same way as the exact eigenvalues and eigenvector. The critical radius R_c is nondimensionalized by the cylinder radius R_0: $r_c = R_c/R_0$. The eigenvalues for the regularized system are

$$i\phi_{\pm reg} = -\frac{3}{2}Oh\chi^2 \pm \left\{\frac{9}{4}Oh^2\chi^4 + \frac{1}{2}\left[(1 - \frac{2r_c^2}{(r_c+1)^2})\chi^2 - \frac{1}{r_c+1}\chi^4\right]\right\}^{\frac{1}{2}}, \tag{2.29}$$

and the eigenvectors for the regularized system are

$$2i\phi_{\pm reg}\tilde{r}_a - i\chi\tilde{v}_a = 0. \tag{2.30}$$

To simulate the Rayleigh-Plateau instability, a finite amplitude of perturbation is chosen at $t = 0$. For the demonstration of the symmetric Rayleigh-Plateau instability in figure 2.3, this dimensionless amplitude is $\tilde{r}_a, \tilde{v}_a = 0.05$, whereas the amplitude is chosen to be $\tilde{r}_a, \tilde{v}_a = 0.001$ for the detailed convergence calculations.

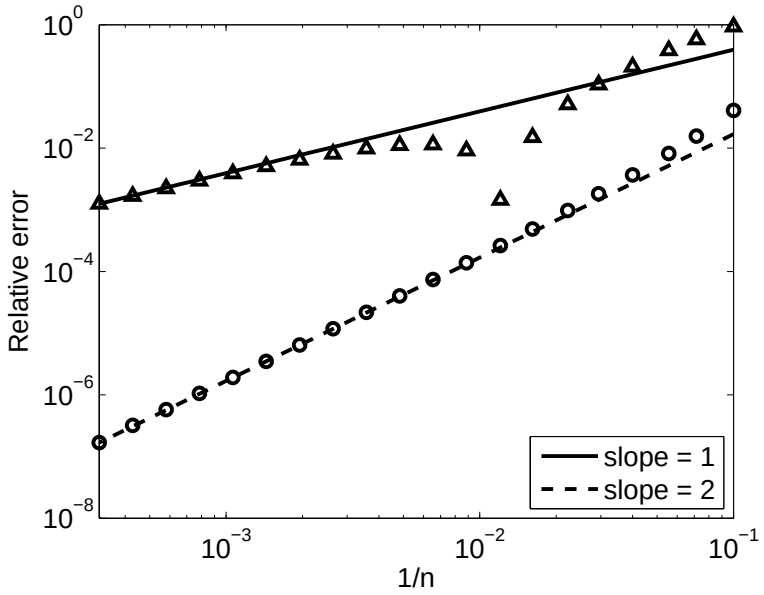

Figure 2.6: Relative error of the perturbation growth rate in a simulation of a Rayleigh-Plateau instability in the linear regime, plotted versus the dimensionless element size $\Delta x/R_0$. The relative error with respect to the exact solution with regularization is plotted with ($\circ$) circles. the triangles ($\triangle$) are the graph of the relative error with respect to the exact solution without regularization. The solution of the model converges with first order accuracy to the analytical solution without regularization, and with second order accuracy to the solution with regularization.

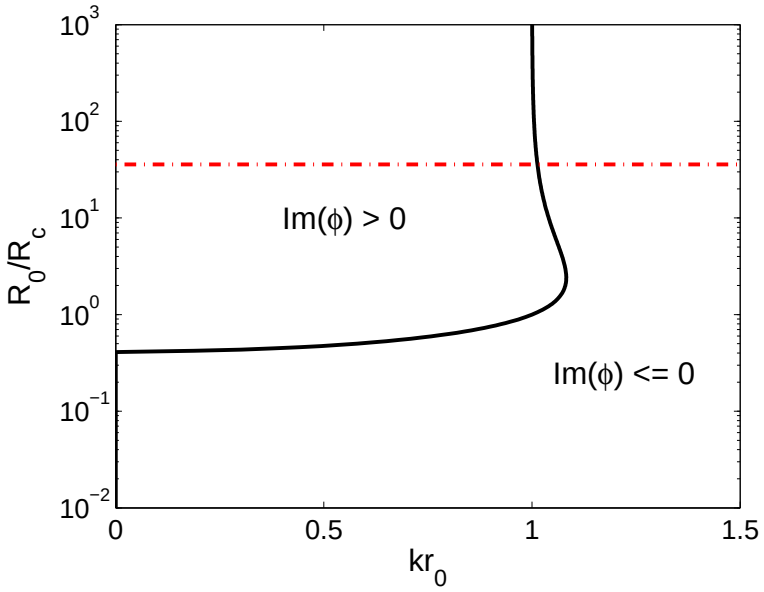

Figure 2.7: Graph of the line where the imaginary part of the eigenvalue crosses zero. The dashed line indicates the parameter values for which the graphs of figure 2.5 were calculated. For any finite value of the viscosity, perturbations with a dimensionless wavenumber below 1 have an eigenvalue with a positive imaginary part. Perturbations with a dimensionless wavenumber above 1 have only eigenvalues with a negative imaginary part, leading to damped surface waves. The graph shows that the regularization has no influence on the dispersion relation when $R_0/R_c \gg 1$. Furthermore it shows that the radius of the cylinder is bounded from below at $R_0/R_c = (\sqrt{2} - 1)$ for the Rayleigh-Plateau instability.

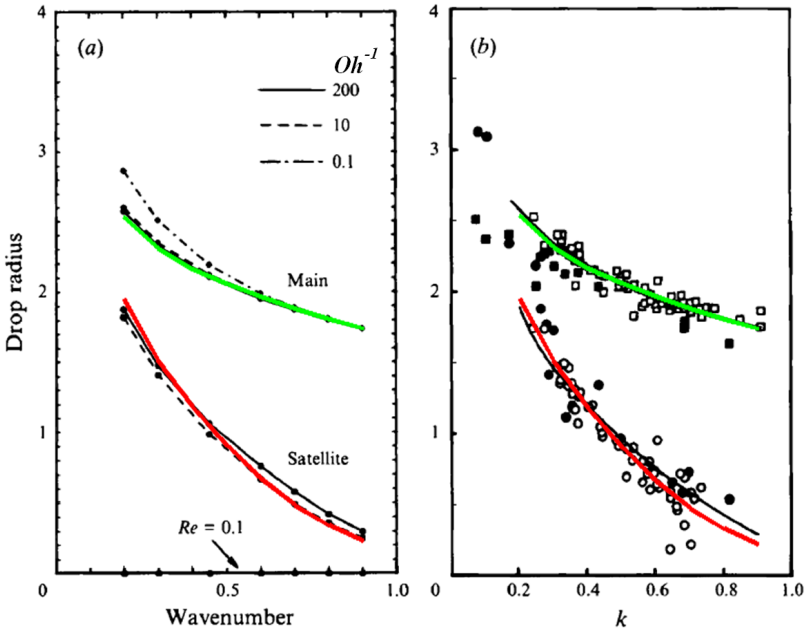

Figure 2.8: Comparison of the final state of the Rayleigh-Plateau instability, as a function of the dimensionless wavenumber (color online). (a) Comparison with the numerical work [19]. The black lines are the 3D axisymmetric FEM results for different Ohnesorge numbers, the thick colored lines are the 1D lubrication approximation results for $Oh^{-1} = 10$. It can be seen that the viscosity has only small influence on the final drop size at a low Ohnesorge number. (b) Comparison with the experimental work of [24] (main: ■, satellite: •) and [23] (main: □, satellite: ○). The solid black lines are the 3D axisymmetric FEM result for $Oh^{-1} = 200$, the thick colored lines are the result of the 1D lubrication approximation model of $Oh^{-1} = 10$. The lubrication approximation model results agree with the experimental results.

2.4.4 Grid convergence

To prevent numerical viscosity and unphysical smearing of the mass distribution, a second order accurate numerical scheme is used in the spatial discretization. To validate the order of accuracy of the im-

plemented scheme, the relative error as a function of the grid size is calculated. The relative error E of the model is found by comparing the growth rate of the amplitude of the perturbation in the velocity to the analytical solutions with and without regularization.

$$E = \left| \frac{C[\phi] - \phi}{\phi} \right| \tag{2.31}$$

where $C[\phi]$ is the numerical approximation of the dimensionless growth rate. In the previous section, the analytical linearized solutions for the Rayleigh-Plateau instability are given. The critical radius is proportional to the cell width, hence the regularized solution converges with first order towards the exact solution. The regularized solution of the model converges with second order accuracy towards the regularized analytical solution of the linearized governing equations. The relative error is shown for an Ohnesorge number of 1, and a perturbation wavelength of $2\sqrt{2}\pi R_0$ in figure 2.6. The scheme avoids numerical diffusivity, as required, since it converges with second order accuracy towards its exact solution. The exact solution of the regularized model converges with first order towards the exact solution without regularization. Hence, for the physical aspects of the solution, such as the tail drop velocity or the growth rate of perturbations, the model should be regarded as first order accurate. The error in the time integration remains within a chosen tolerance due to the adaptive stepsize of the chosen Runge-Kutta method.

To demonstrate the accuracy for different cases, the growth rate for different dimensionless wavelengths and Ohnesorge numbers is compared to the analytical solution. These dispersion relations are shown in figure 2.5. For this calculation, a grid of 150 nodes is used. The Ohnesorge number and the dimensionless wavelength are related to the radius of the liquid cylinder. When this radius changes due to stretching or other phenomena, these parameters also change. Since the model is accurate for all Ohnesorge numbers and dimensionless wavelengths, the linear dynamics of the break up of a liquid jet will be simulated accurately in all stages of breakup.

To test the influence of the regularization on the dispersion relation, the growth rate is calculated as a function of the non dimensional regularization parameter R_0/R_c and the non dimensional wavelength χ. In figure 2.7, the line is plotted, where the imaginary part of the dimensionless frequency goes through zero. The imaginary part of the

frequency is the growth rate. A positive growth rate indicates a growing perturbation. On the high wavenumber side of this line, the growth rate is negative.

The influence of the regularization vanishes when $R_0/R_c >> 1$. The regularization imposes a lower bound on the radius, which does not depend on the Ohnesorge number. The dimensionless value of this lower bound is $R_0/R_c = (\sqrt{2} - 1)$, which is the minimum of the regularized capillary tension of a cylinder, as a function of the radius R_0 of the cylinder.

2.4.5 Satellite droplets

The final state of the Rayleigh-Plateau instability consists of main and satellite droplets. The satellite droplet is defined as the droplet that arises at the trough of the initial radial perturbation. The final droplet sizes of the presented numerical model are compared to existing experimental and numerical work. In the experiments, an axisymmetric laminar jet is perturbed with wavelengths longer then its circumference ([24], [23]). The amplitude of the perturbation is constant at the nozzle, hence the instability is asymmetric in space. The amplitude of the perturbation on the jet depends on the distance that the liquid has traveled from the nozzle. The compared numerical work ([19]) is a 3D axisymmetric finite element method (FEM). In this FEM, the velocity is a function of the radial coordinate, and a nonzero radial velocity is permitted, as opposed to the presented lubrication approximation model.

The Ohnesorge number in the experimental work is low, $Oh \approx 5 \cdot 10^{-3}$, which means that the pinchoff cannot be represented on a 1 dimensional axisymmetric grid due to the overturning of the free surface ([29]). At low Ohnesorge numbers, the viscosity only has a small influence on the satellite sizes ([19]). Therefore, the droplet sizes for an Ohnesorge number of 0.1 can be compared to the experimental and numerical work from literature in figure 2.8. The final droplet sizes predicted by the presented model for an Ohnesorge number of 0.1 are given in table 2.1.

To demonstrate the practical strength of the presented numerical model, a collapsing cylinder with spherical caps is shown in figure 2.9. The simulation is started with a single finite quiescent cylinder. The cylinder is simulated with symmetrical boundary conditions at $x = 0$,

a low viscosity has been chosen to allow capillary waves ahead of the tail droplet ($Oh \approx 0.04$). The tail drop speed can be estimated. In a frame of reference that travels with the tail drop, a force is exerted by the surface tension, and an advective momentum flux into the droplet is present due to the flow of mass into the tail droplet. The force exerted by the surface tension on the tail droplet is $\tau_\sigma = \pi\sigma R_0$, and the momentum flux into the tail droplet is given by $\tau_{mom} = \rho\pi u^2 R_0^2$. By balancing these forces, the tail droplet velocity is found:

$$u = \sqrt{\frac{\sigma}{\rho R_0}} = \frac{R_0}{t_\sigma} \tag{2.32}$$

The length of the cylinder, from the symmetry plane to the end, is initially 48 times the radius of the liquid cylinder. Therefore, it should take about 48 times the capillary time for the tail droplet to reach the symmetry plane, which agrees with the simulation results, as can be seen in figure 2.9.

2.5 Conclusions

We have developed a numerical model for the evolution of a slender liquid jet, based on the lubrication approximation. The novel feature of this model is the way in which coalescence and pinchoff are treated. The transfer of the system over the singular events is consistent and conserves both mass and momentum.

In the continuum approximation, and assuming a sharp interface, pinchoff and coalescence are singularities. In our model, we regularize these events by a modification of the capillary force in the model. This modification conserves mass and momentum. It converges to the unmodified capillary force in the limit where the spatial step size goes to zero, with first order convergence. Without this modification, the model is second order accurate.

This model accurately predicts the growth rate of viscous Rayleigh-Plateau instabilities and the size distribution of droplets that result from the breakup of a liquid jet due to a Rayleigh-Plateau instability. The velocity of an end droplet that forms on a liquid column is correctly predicted. The model can be used to simulate applications such as inkjet printing or monodisperse droplet production.

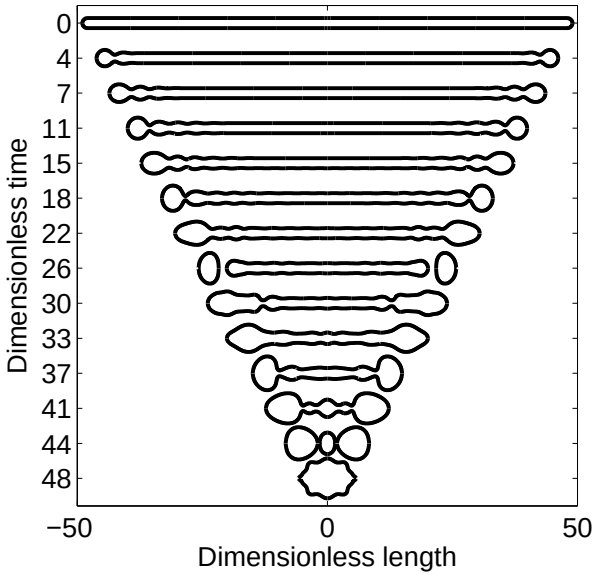

Figure 2.9: Surface tension driven collapse of a low viscous, $Oh \approx 0.04$, liquid cylinder with spherical caps. The cylinder is plane symmetric in $x = 0$. The timescale is non dimensionalized by the capillary time. The length scale is non dimensionalized by the initial radius of the cylinder. This figure shows that the model can be used to simulate breakup and coalescence.

2.6 Discussion

The influence of the regularization goes to zero with a vanishing cell width. In practice, this is limited by the presence of the singularities in the exact solution. When the regularization radius R_c goes to zero, the velocity close to the singularities diverges rapidly. The regularization allows us to cross the singularities, at the cost of detail in the pinchoff and coalescence structures ([30]).

The model presented in this paper is especially suitable for the investigation of pinchoff and merging of droplets in a spatially asymmetrical

liquid jet and the resulting asymmetric Rayleigh-Plateau instability. More detailed information can also be extracted from this kind of simulations, such as capillary waves induced by the pinchoff, interaction of different perturbations, and the oscillation frequency of the resulting droplets.

3 | Lattice Boltzmann Method to study the contraction of a viscous ligament*

We employ a recently formulated axisymmetric version of the multiphase Shan-Chen (SC) lattice Boltzmann method (LBM) [Srivastava et al., in preparation (2013)] to simulate the contraction of a liquid ligament. We compare the axisymmetric LBM simulation against the slender jet (SJ) approximation model [T. Driessen and R. Jeurissen, IJCFD **25***, 333 (2011)]. We compare the retraction dynamics of the tail-end of the liquid ligament from the LBM simulation, the SJ model, Flow3D simulations and a simple model based on the force balance (FB). We find good agreement between the theoretical prediction (FB), the SJ model, and the LBM simulations.*

3.1 Introduction

The formation of liquid filaments is ubiquitous, it happens whenever there is a droplet fragmentation [31]. Examples of fragmentation processes are the breakup of a liquid filament stretched from a bath or the collapse of a liquid film [32, 33]. The formation of these liquid filaments is very common in the breakup of ocean spume where they influence the properties of the marine aerosols [34]. In industry, the dynamics

*Published as: Sudhir Strivastava, Theo Driessen, Roger Jeurissen, Herman Wijshoff and Federico Toschi, "Lattice Boltzmann Method to study the contraction of a viscous ligament", Int. J. Mod. Phys. C. **24**, 12, 2013. The part related to the force balance (FB) model and the slender jet (SJ) model are part of the present thesis. The Lattice Boltzmann simulations were done by Sudhir Srivastava, the Flow3D simulations were done by Herman Wijshoff.

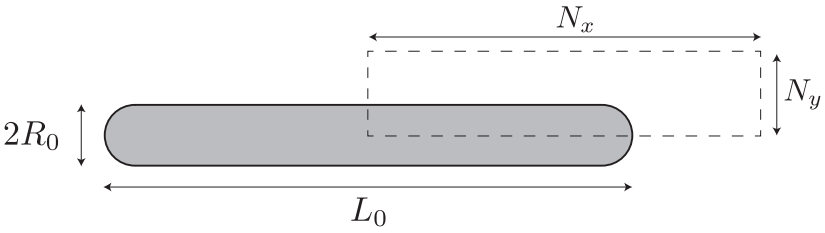

Figure 3.1: A schematic of the initial configuration of the axisymmetric viscous ligament. The rectangular dotted box of size $N_x \times N_y$ represents the domain for LBM simulation.

of filaments is a key issue for the print quality in inkjet printing [3], where elongated liquid filaments are ejected from the nozzle (see figure 3.1). For optimal print quality, the filaments should contract to a single droplet before they hit the paper. Depending on the fluid properties, size and shape of the filament, it may collapse into a single droplet (stable contraction), or it may break up into several droplets (unstable contraction)[35]. The stability of the contraction of a smooth filament crucially depends on the Ohnesorge number,$\mathrm{Oh} = \nu_l \sqrt{\rho_l/(\gamma_{lg} R_0)}$ [36, 37, 38], where ν_l, ρ_l,γ_{lg}, and R_0 are the kinematic viscosity, fluid density, surface tension and radius of the filament, respectively. When $\mathrm{Oh} > \mathcal{O}(0.1)$, the viscous dissipation dominates and there is no energy left to deform the surface of the filament, hence the contraction always remains stable. On the other hand when $\mathrm{Oh} < \mathcal{O}(0.1)$, low viscous dissipation allows for large surface deformation that may result in the breakup of the filament. Notz et al. found that the stability of contraction for $\mathrm{Oh} < \mathcal{O}(0.1)$ depends on the aspect ratio of the filament, $\Gamma_0 = L_0/(2R_0)$, where L_0 is the initial length of the filament, and for $\mathrm{Oh} = \mathcal{O}(0.1)$ the contraction of the filament is stable and independent Γ_0 [38]. In this chapter we use the axisymmetric multiphase LBM to simulate the stable contraction of the filament [39]. We validate the LBM model by comparing it against the 1D numerical slender jet (SJ) model by Driessen & Jeurissen [40], an analytic model based on force balance (FB), and the Flow3D† simulation.

†Flow3D™ is CFD software developed by Flow Science Inc., Santa Fe, New Mexico.

3.1.1 Lattice Boltzmann method

In this section we prescribe a brief description of the axisymmetric LBM for multiphase flow [39]. The model is defined on the Cartesian two-dimensional (2D) lattice by means of the nine-speeds, $\mathbf{c}_i \equiv (c_{ix}, c_{iy})$, and distribution function, f_i:

$$f_i(\mathbf{x} + \mathbf{c}_i\delta t, t + \delta t) = f_i(\mathbf{x}, t) - \frac{1}{\tau}\big(f_i(\mathbf{x}, t) - f_i^{\mathrm{eq}}(\rho, \mathbf{u}^{\mathrm{eq}})\big) + \delta t\, h_i\,, \quad (3.1)$$

where $\mathbf{x} = (x, y)$ is the position vector, t is time and δt is the time step. In the above expression we have made use of the BGK approximation to let the distribution relax to the equilibrium distribution, f_i^{eq}. The bulk viscosity, μ, of the fluid is related to the relaxation parameter, τ, as $\mu = \rho c_{\mathrm{s}}^2 \delta t\,(\tau - 0.5)$, where $c_{\mathrm{s}} = \sqrt{3}$ is the speed of sound in the LB model. The fluid density, ρ and velocity $\mathbf{u} \equiv (u, v)$ are defined as:

$$\rho = \sum_i f_i\,, \qquad\qquad \mathbf{u} = \frac{1}{\rho}\sum_i \mathbf{c}_i f_i\,, \quad (3.2)$$

respectively. In absence of any external force $\mathbf{u}^{\mathrm{eq}} = \mathbf{u}$. The additional term h_i in equation (3.1) has the following form:

$$h_i = W_i\Big(-\frac{\rho v}{y} + \frac{1}{y c_s^2}\big(c_{ix}h_{ix} + c_{iy}h_{iy}\big)\Big), \quad (3.3)$$

where $(h_{ix},\, h_{iy}) = \Big(c_{ix}\big(\mu\big(\partial_y u + \partial_x v\big) - \rho uv\big),\, c_{iy}\big(2\mu\big(\partial_y v - y^{-1}v\big) - \rho v^2\big)\Big)$ and W_i's are the lattice dependent weights. The Chapmann-Enskog expansion of equation (3.1) gives the axisymmetric continuity and Navier-Stokes' equations (NS):

$$\partial_t \rho + \nabla\cdot(\rho\mathbf{u}) = -y^{-1}\rho v, \quad (3.4)$$

and

$$\partial_t\big(\rho\mathbf{u}\big) + \nabla\cdot\big(\rho\mathbf{u}\mathbf{u}\big) = -\nabla p + \nabla\cdot\big(\mu\big(\nabla\mathbf{u} + \nabla\mathbf{u}^T\big)\big) + \mathbf{f}, \quad (3.5)$$

$$\text{where}\quad \mathbf{f} = y^{-1}\Big(\mu\big(\partial_y u + \partial_x v\big) - \rho uv\,,\, 2\mu\big(\partial_y v - y^{-1}v\big) - \rho v^2\Big),$$

and ∇ is the 2D divergence operator in the Cartesian coordinate system [39, 41]. In this manuscript, symbols x and y represent the axial and

radial distances, respectively. The equations (3.4) and (3.5) are written in a form to emphasize the 2D continuity and NS equation. The additional term $-y^{-1}\rho v$ and $\mathbf{f}$ on R.H.S. of equation (3.4) and (3.5), respectively, arise due to axisymmetry.

The long-range interaction force, $\mathbf{F}$, in the Shan-Chen (SC) model is defined as:

$$\mathbf{F} = -Gc_s^2\,\delta t\,\psi\hat{\nabla}\psi - \frac{G}{2}c_s^4\,(\delta t)^3\,\psi\hat{\nabla}(\hat{\nabla}^2\psi) + \mathcal{O}((\delta t)^5), \tag{3.6}$$

where G is the interaction strength between two phases and $\hat{\nabla}, \hat{\nabla}^2$ are the gradient and Laplace operators, respectively in the 3D Cartesian coordinate system [42, 43]. The equation (3.6) for axisymmetric cylindrical polar coordinate is given by:

$$\mathbf{F} = -Gc_s^2\,\delta t\,\psi\nabla\psi - \frac{G}{2}c_s^4\,(\delta t)^3\,\psi\nabla\Big(\nabla^2\psi + y^{-1}\partial_y\psi\Big) + \mathcal{O}((\delta t)^5), \tag{3.7}$$

where ∇^2 is the 2D Laplace operator in the Cartesian coordinate system. The axisymmetric contribution in addition to the 2D SC force comes from second term of the equation (3.6) and it is given by

$$-\frac{G}{2}c_s^4(\delta t)^3\psi\nabla(y^{-1}\partial_y\psi) \tag{3.8}$$

.

The force $\mathbf{F}$ given by equation (3.7) is added in to the system by shifting the equilibrium velocity as $\mathbf{u}^{\mathrm{eq}} = \frac{1}{\rho}\left(\sum_i \boldsymbol{c}_i f_i + \tau\mathbf{F}\right)$, and the fluid velocity is defined as $\mathbf{u} = \frac{1}{\rho}\left(\sum_i \mathbf{c}_i f_i + \frac{\delta t}{2}\mathbf{F}\right)$. The finite difference approximations used for the derivatives in equations (3.3), (3.7) are isotropic and fifth-order accurate. This is necessary in order to minimize the truncation error that appears in the long- wavelength and in the small Mach number limit of equation (3.1). The non-ideal pressure, $p_{NI} = c_s^2\rho + \frac{c_s^2 G}{2}\psi^2$ in the axisymmetric multiphase LBM is same as the non-ideal pressure for 3D LBM [44]. Our choice of the effective density functional is $\psi(\rho) = \rho_0\big(1 - \exp(-\rho/\rho_0)\big)$, where ρ_0 is a reference density.

3.1.2 Lubrication Theory model

We are using the slender jet approximation to model the stability of an axisymmetric viscous liquid filament [38, 40, 8, 45, 46, 29, 47]. In

the slender jet approximation, the fluid flow in the axial direction is assumed to be dominant. Therefore, radial inertia is neglected and the axial velocity is assumed to be uniform in the radial direction. As a result, the fluid interface is a well defined, single valued function of the axial coordinate, from which the full curvature of the interface can be calculated. If we use the initial radius of filament, R_0, as the length scale and the capillary time, $t_{cap} = \sqrt{\rho_l R_0^3/\gamma_{lg}}$ as the time scale, then the SJ model in the dimensionless form is given by:

$$\partial_t h = -u\partial_x h - \frac{1}{2}h\partial_x u, \quad \partial_t u = -u\partial_x u - \partial_x p_{\text{Lap}} + 3\,\text{Oh}\, h^{-2}\partial_x(h^2\partial_x u), \tag{3.9}$$

$$p_{\text{Lap}} = h^{-1}\Big(1 + (\partial_x h)^2\Big)^{-1/2} - \partial_{xx} h\Big(1 + (\partial_x h)^2\Big)^{-3/2},$$

where h, u, x, t and p_{Lap} are dimensionless, and represent the radius of the jet, axial velocity, axial coordinate, time, and Laplace pressure, respectively. For this study we use the numerical model developed by Driessen and Jeurissen to solve equation (3.9) [40]. The solutions to these equations are singular at each pinch-off, and at each collision of liquid bodies [8]. To allow the described physical system to transfer across the singularities that occur at pinch-off and coalescence, the surface tension term is regularized by a modification at a radius of the order of the cutoff radius, h_c. The cutoff radius, h_c is a control parameter of the regularization, and is chosen to scale with the spatial step. For the SJ simulations presented in this manuscript $h_c = R_0/60$.

3.2 Results and discussion

In this section we show the comparison of simulation from LBM and SJ for the contraction of liquid filament. The LBM simulation is carried out for the following parameters (LBM units): system size, $N_x \times N_y = 1600 \times 256$, $L_0 = 2000$, $R_0 = 49.5$, relaxation parameter, $\tau = 1$, kinematic viscosity, $\nu_l = 0.17$, Shan-Chen interaction parameter, $G = -5$, liquid density, $\rho_l = 1.95$, vapor density, $\rho_g = 0.16$, and surface tension, $\gamma_{lg} = 0.0568$. For above LBM parameters we have $\text{Oh} = 0.14$, $\Gamma_0 = 20$. This parameter choice is suitable for simulating the stable contraction of a smooth filament. For our study it is sufficient to simulate only half of the liquid filament (see figure 3.1). We use

the symmetry boundary condition at left, right and bottom boundaries and the free slip at the top boundary [48].

In order to make a comparison between the two models we need to have a common system for measuring the physical quantities and we opted for expressing quantities in dimensionless units. We choose the initial radius of the filament, R_0, and the capillary time, t_{cap}, to scale length and time in LBM simulations. For SJ simulations we use the aspect ratio, $\Gamma_0 = 20$, and the $\mathrm{Oh} = 0.14$.

First, we compare the time evolution of the filament shape obtained from the LBM and the SJ simulation (see the right panel of figure 3.2). During the collapse, there is a perfect agreement of all the models. When the tail droplets merge into one big droplet, the simulation results start to differ; in the LB simulation, the maximum radial extent of the droplet is larger and dimples form on both sides of the droplet. We hypothesize that this is due to the lubrication approximation in the SJ model. When the tail droplets merge, $\partial_y u$ becomes significant, while it is neglected in the SJ model. When the radial extent of the droplet reaches its maximum, the kinetic energy is mostly converted into surface energy. A smaller radial extent indicates that the dissipation was larger. The origin of this numerical dissipation is similar to the dissipation in a shock in gas dynamics, or a hydraulic jump in hydraulic engineering; momentum is conserved, but energy is dissipated in a shock. The concave drop shape obtained in the LB simulation indicates that the lubrication approximation causes dissipation here. This shape cannot be represented as a single valued function in the one dimensional space of the SJ model, and the numerical dissipation in the SJ model is the effect that prevents the formation of these dimples.

For the second validation we compare our LBM results to the SJ model and the Flow3D simulation. Additionally, we estimate the position of the tail-end of the filament by an analytical model based on the force balance (FB).

In the FB model the rate of change of the mass, m, and momentum, $P = mu$, of the tail-drop is given by:

$$\frac{dx}{dt} = u, \qquad \frac{dm}{dt} = \rho_l \pi R^2 u, \qquad \frac{dP}{dt} = -\pi R^2 \frac{\gamma_{lg}}{R} = -\pi \gamma_{lg} R \tag{3.10}$$

where u is the velocity of the tail-drop, $2x$ is the length and R is the radius of the filament. The solution of equation (3.10) subject to the initial conditions: $x(0) = 0.5L_0 - R_0$, $m(0) = (2\pi/3)\rho_l R_0^3$ and

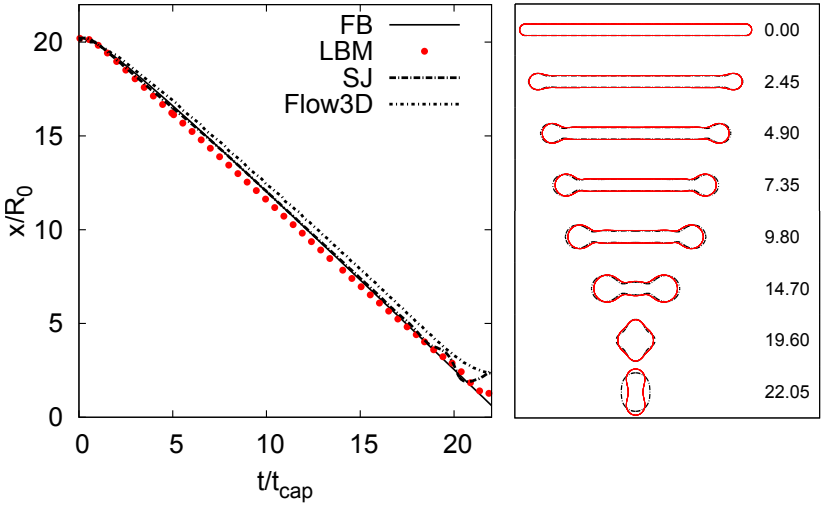

Figure 3.2: Left panel: The tip location of the collapsing filament as a function of time in the presented models. The difference between the LBM simulation, SJ simulation and FB model is smaller than the interface thickness in the LBM simulation. The simulations and the analytical result agree with each other, up to the moment when the tail droplets merge. Right panel: Time evolution of interface profile of the liquid filament. The labels on the figure show the dimensionless time, t/t_{cap}. The data points from the LBM simulation are shown in red color, whereas the data from SJ model are shown in black color.

$P(0) = 0$, gives us the length of the filament in time, $2x(t)$ ($R_0 = R(0)$). In this force balance the tail velocity converges to the capillary velocity, $u_{cap} = \sqrt{\gamma_{lg}/(\rho_l R)}$ [49]. The solutions from FB model, SJ model, Flow3D simulation and LBM simulation are in very good agreement with each other (See figure 3.2, right panel).

3.3 Conclusion

The axisymmetric multiphase SC LBM has been validated on the test problem of the stable contraction of liquid filament [39]. For this val-

idation the LBM simulations was compared to SJ, FB models, and Flow3D simulations. Furthermore the position of the tail-end of the drop was compared with a model based on the balance of forces. We found that the proposed axisymmetric multiphase SC LBM can accurately simulate the collapse of viscous liquid filament [39].

4 | Stability of viscous long liquid filaments*

We study the collapse of an axisymmetric liquid filament both analytically and by means of a numerical model. The liquid filament, also known as ligament, may either collapse stably into a single droplet or break up into multiple droplets. The dynamics of the filament are governed by the viscosity and the aspect ratio, and the initial perturbations of its surface. We find that the instability of long viscous filaments can be completely explained by the Rayleigh-Plateau instability, whereas a low viscous filament can also break up due to end pinching. We analytically derive the transition between stable collapse and breakup in the Ohnesorge number versus aspect ratio phase space. Our result is confirmed by numerical simulations based on the slender jet approximation and explains recent experimental findings by Castréjon-Pita et al., PRL ***108****, 074506 (2012).*

4.1 Introduction

The formation of liquid filaments is ubiquitous. It happens whenever there is droplet fragmentation [31]. Examples of fragmentation are the breakup of a liquid filament stretched from a bath [32], or the collapse of a liquid film [33]. The formation of these liquid filaments is very common in the breakup of ocean spume, where they influence the properties of the marine aerosols [34]. In industry, the dynamics of filaments are a key issue for the print quality in inkjet printing [3], where

*Published as: Theo Driessen, Roger Jeurissen, Herman Wijshoff, Federico Toschi and Detlef Lohse, "Stability of viscous long liquid filaments", Phys. Fluids **25**, 062109 (2013)

elongated liquid filaments are ejected from the nozzle. For optimal print quality, the filaments should contract to a single droplet before they hit the paper. Therefore we study the details of the dynamics of these filaments.

Depending on the viscosity, size and shape of the filament, it may collapse into a single droplet, or it may break up into multiple smaller droplets [5]. A filament collapse resulting in a single droplet is called stable. A filament collapse into multiple droplets is called unstable. The stability of the filament influences the number of droplets and their size distribution, after the collapse of the filament.

Since filaments are essentially finite liquid jets, the stability of liquid jets is relevant here. The earliest reported observations of the stability of liquid jets were done by Savart in 1833, who observed that a continuous liquid jet breaks up into distinct droplets [50]. Plateau reported that a varicose perturbation of the liquid jet is unstable, if the wavelength of the perturbation is larger then the circumference of the jet [51]. In 1878, Lord Rayleigh derived the dispersion relation for an infinite jet with a small periodical perturbation [4].

The classical Rayleigh-Plateau instability assumes a sinusoidal perturbation with a time dependent amplitude

$$R(x,t) = R_0 + \tilde{R}(t)\cos\left(\chi\frac{x}{R_0}\right), \tag{4.1}$$

where x is the axial position on the cylinder, and χ is the dimensionless wavenumber of the varicose perturbation on the surface of the cylinder. The wavenumber is nondimensionalized by the relevant length scale of the problem, namely the unperturbed radius of the cylinder, R_0: $\chi = 2\pi R_0\lambda^{-1}$. In this linear approximation, the amplitude of the perturbation $\tilde{R}(t)$ grows exponentially with time,

$$\tilde{R}(t) = \delta e^{\omega(t-t_0)}, \tag{4.2}$$

where ω is the growth rate of the perturbation amplitude, and δ is the amplitude of the perturbation at $t = t_0$. In the inviscid theory by Rayleigh, ω is inversely proportional to the capillary time $t_{cap} = \sqrt{\frac{\rho R_0^3}{\sigma}}$, where ρ and σ are respectively the density and surface tension of the liquid.

Weber derived the dispersion relation for the Rayleigh-Plateau instability including the influence of viscosity [52]. The relevant dimen-

sionless group for the dynamics of the viscous Rayleigh-Plateau instability on an infinite cylinder is the Ohnesorge number

$$\mathrm{Oh}_R = \frac{\mu}{\sqrt{\rho\sigma R_0}}, \tag{4.3}$$

where μ is the dynamic viscosity. The Ohnesorge number is the ratio of the viscous timescale over the capillary time scale. The stability of the jet decreases with a decreasing Ohnesorge number. Weber showed in the same paper that the linearized dispersion relation of the Rayleigh-Plateau instability gives a very good approximation of the exact result. The linearized growth rate of the viscous Rayleigh-Plateau instability ω is [52]

$$\omega t_{cap} = \sqrt{\frac{1}{2}(\chi^2 - \chi^4) + \frac{9}{4}\mathrm{Oh}_R^2\chi^4} - \frac{3}{2}\mathrm{Oh}_R\chi^2. \tag{4.4}$$

For each value of Oh, one dimensionless wave number has the highest growth rate: $\chi_{max} = (2 + 3\sqrt{2}\mathrm{Oh}_R)^{-1/2}$. In this study we assume that the surface of the filament has a random varicose perturbation at $t = t_0$. A Rayleigh-Plateau instability originating from noise is dominated by χ_{max}. Substituting χ_{max} into the dispersion relation, equation (4.4), we find that the growth rate of the fastest growing mode ω_{max} is a function of Oh_R only. When $\tilde{R}$ has grown to $\tilde{R} \approx R_0$, the filament breaks. Substituting $\tilde{R} = R_0$ and $\omega(\chi, \mathrm{Oh}_R) = \omega_{max}(\mathrm{Oh}_R)$ into equation (4.2) gives the breakup time t_B,

$$t_B = t_0 + \frac{1}{\omega_{max}(\mathrm{Oh}_R)} \log\left(\frac{R_0}{\delta}\right). \tag{4.5}$$

Experiments have shown that the linear approximation for the breakup time is a very good approximation [26].

In practice, liquid jets are never infinitely long. With the advance of computational power and experimental techniques, investigating the stability of liquid filaments became possible. Using a numerical model, Schulkes found that above a certain Oh_R, the filament collapse is always stable [36]. Later Notz & Basaran refined this result by showing that the stability of the filament collapse depends on both Oh_R and the aspect ratio $\Gamma = 0.5L/R$ of the filament [38], where L is the length of the filament. So-called end pinching, first observed by Stone [37], is the cause of the breakup in both studies.

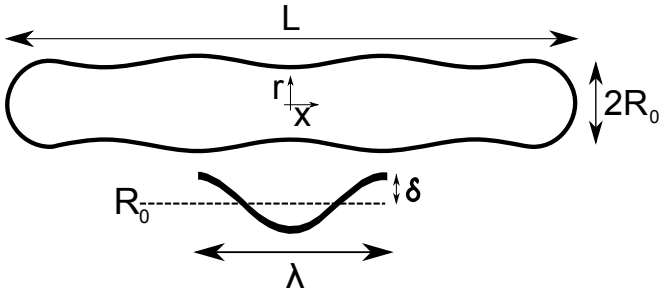

Figure 4.1: Shape of the filament at t_0, just after the filament has pinched off from e.g. a film or a large filament. The surface is perturbed, with an assumed sinusoidal perturbation superposed on R_0. The wavelength of the perturbation is λ. The amplitude of the perturbation at t_0 is δ. The filament considered is symmetric in the $x = 0$ plane.

In a recent experimental study, Castréjon-Pita *et al.* [53] validated the numerical results by Notz & Basaran [38] in the regime of $\mathrm{Oh}_R < 0.1$, where end pinching is the dominant breakup mechanism. The experiments however showed unstable filaments up to $\mathrm{Oh}_R \approx 1$. In the regime of long viscous filaments, the breakup occurs simultaneously along the entire axis of the jet, which is characteristic for the Rayleigh-Plateau instability on an infinite jet (figure 4.2). In the existing numerical studies on the collapse of the finite liquid filament [36, 38], the initial amplitude of the Rayleigh-Plateau instability has been set to zero. However, the breakup of the circular cylindrical part of the filament occurs within finite time, hence δ must be nonzero at t_0. However, the experiments show that the circular cylindrical part of the filament breaks up. Hence δ is finite at t_0. The dynamics of the liquid filament are governed by three dimensionless groups, namely Γ, Oh_R and the relative initial distortion $\epsilon = \delta/R_0$.

In this chapter, the stability of long viscous filaments is predicted with the linear theory from [4, 52]. The critical aspect ratio Γ_c, above which the filament breaks up due to the Rayleigh-Plateau instability before it merges, depends on Oh_R and ϵ. The results of the linear theory are validated against the experimental data [53] and a drop formation model in the slender jet approximation [40] . For very high viscosity,

an analogy is found with the viscosity dominated contraction of viscous sheets.

4.2 Critical aspect ratio

The critical aspect ratio Γ_c is defined as the aspect ratio above which the filament collapses due to the Rayleigh-Plateau instability. This aspect ratio is found by comparing the breakup time due to the Rayleigh-Plateau instability with the time that the filament needs to merge into a spherical droplet. The analysis of the collapse of the liquid filament starts at t_0, when the filament pinches off from another body of liquid at both sides. The filament contracts due to the surface tension. As the filament contracts, bulges will form at the end of the filament. These bulges are called tail droplets. The fluid that has not yet been entrained by the tail droplets remains stationary. For low to moderate viscosities, the typical velocity of these tail droplets can be found from balancing the momentum flux into the tail droplet with the capillary forces act on it. This typical velocity is called the capillary velocity, $u_{cap} = \sqrt{\frac{\sigma}{\rho R_0}}$ [49].

When the collapse of the filament is stable, the tail droplets move towards the center of mass, where they merge into one droplet. The distance that the tips of the jets have to travel is given by half the length of the filament minus the diameter of the tail droplet $2R_d$ at the moment of merging. The minimal time for the tail droplets to merge is called the merge time t_M

$$t_M = \frac{0.5L - 2R_d}{u_{cap}}, \tag{4.6}$$

where R_d is the radius of the tail droplets at the merge time t_M. At that time, each of the two tail droplets has accumulated half of the initial volume of the liquid filament. This results in the tail droplet radius

$$R_d = \left(\frac{3}{4}\Gamma\right)^{1/3} R_0. \tag{4.7}$$

In the calculation of R_d the filament is considered as a circular cylinder of length L. The merge time t_M is rewritten as a function of Γ and

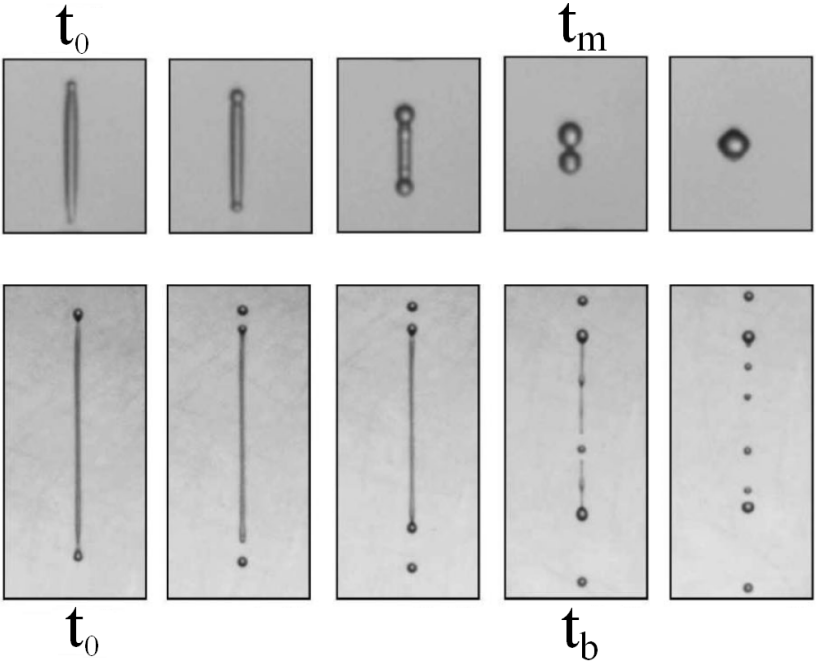

Figure 4.2: Sequences of the contraction of a liquid filaments, taken from [53] with permission. The upper sequence shows from left to right the stable collapse of a low viscous ligament. We call the moment when the tail droplets are in contact, t_M. The lower sequence shows the unstable collapse of a longer, more viscous ligament. At t_0 the filament breaks off from the big tail droplets. We call the moment when the filament breaks up everywhere t_B. The initial properties are $\Gamma = 9$ and $\mathrm{Oh}_R = 0.04$ for filament the upper filament, and $\Gamma = 29.2$ and $\mathrm{Oh}_R = 0.18$ for the lower filament.

t_{cap}, using equation (4.6), (4.7), and $u_{cap} = \dfrac{R_0}{t_{cap}}$:

$$t_M = t_{cap}\left[\Gamma - (6\Gamma)^{1/3}\right], \tag{4.8}$$

this shows that t_M is nearly proportional to Γ, with a small correction since the tail droplets have a finite radius.

The Rayleigh-Plateau instability causes a filament to break up when $t_B < t_M$. When $t_B = t_M$, a slightly longer or less viscous filament would collapse into two or more droplets, rendering the collapse unstable. From this balance, the critical aspect ratio Γ_c can be found. An expression for the critical aspect ratio Γ_c as a function of $\omega_{max}(\mathrm{Oh}_R)$ and ϵ is found by balancing equations (4.5) and (4.8), putting $t_0 = 0$.

$$\frac{\log(\epsilon)}{t_{cap}\omega_{max}(\mathrm{Oh}_R)} + (6\Gamma_c)^{\frac{1}{3}} - \Gamma_c = 0. \tag{4.9}$$

In Fig. 4.3 this critical aspect ratio is shown in the phase diagram of Γ versus Oh_R, for $\epsilon = 0.01$.

When the viscosity dominates, the filament contraction is stable. Eggers & Fontelos showed that isolated inertialess droplets cannot break up [54]. In the absence of inertia, the Rayleigh-Plateau instability no longer causes the filament to break up. Since the presented theory uses the Rayleigh-Plateau instability to find Γ_c, it is of interest to find the upper viscous limit where the filament can still break up. An analogy with the capillary contraction of a liquid filament is the capillary contraction of a liquid sheet [55, 56]. During the contraction, a liquid rim forms at the edge of the sheet, analogue to the tail droplet that forms in the contraction of a liquid jet. Brenner & Gueyffier showed that the spatial extent of this rim can be estimated with the Stokes length, $L_\mu = \mu^2/(\rho\sigma)$ [57]. When L_μ is larger than the length of the sheet, the rim does not form and the sheet contracts homogeneously. We expect that the axial extend of the tail droplets on the viscous filaments is also the Stokes length. Viscosity dominates the contraction of a viscous filament when the Stokes length is larger than half the filament length, since the filament has two ends. The ratio between the Stokes length and half the length of the filament can be written as the length-based Ohnesorge number, Oh_L, with

$$\mathrm{Oh}_L^2 = \frac{\mu^2}{\rho\sigma}\frac{2}{L}, \tag{4.10}$$

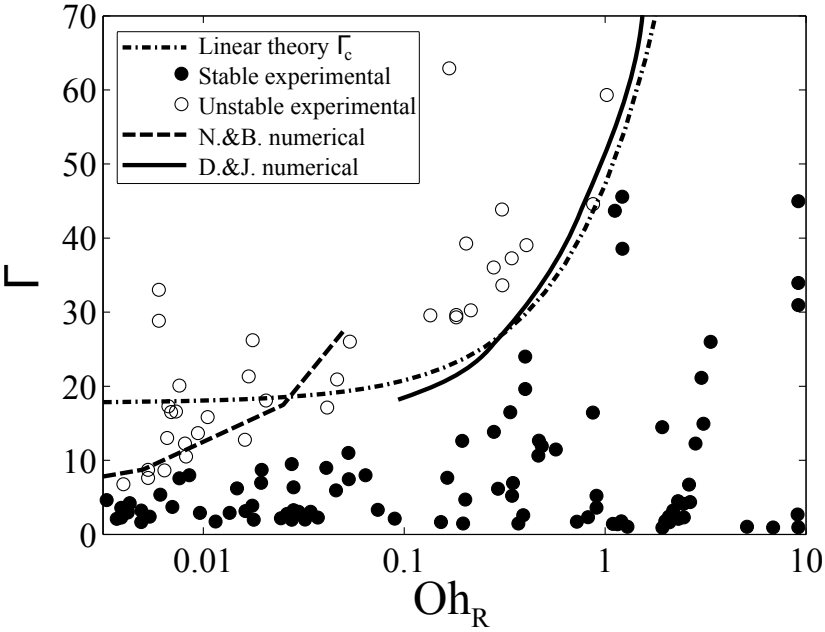

Figure 4.3: Parameter study of the stability of the contraction of a filament. The result of the linear theory, Γ_c, is shown for $\epsilon = 0.01$ in the dashed dotted line. The linear theory is confirmed by the results of the numerical model [40], solid line. Stability of low viscous filaments has been studied numerically by Notz & Basaran [38], dashed line. The experimental results by [53] are shown (circles for unstable, disks for stable regime). Linear theory correctly predicts the critical aspect ratio for filaments of $Oh > 0.1$.

where the first factor on the right-hand side is the Stokes length. When $\mathrm{Oh}_L \ll 1$, the Stokes length is much smaller than the length of the filament; this means that the influence of the axial extend of the tail droplet on the stability of the filament is negligible. The highest value of Oh_L in the unstable region in the phase diagram of Fig. 4.3 is 0.03, which shows that the stabilizing effect found by [54] is not significant in this part of the phase space.

4.3 Numerical results

We use a numerical model to validate the presented linear theory. Equation (4.8) shows that for large Γ, the merging occurs after many t_{cap}, which is the timescale of the growth of perturbations. Even very small perturbations may cause a breakup before $t = t_M$ in the case of long filaments. The visualization of the small initial perturbation demands a very high optical resolution. Dedicated experimental setups have been built to measure the initial perturbation amplitude of a stimulated Rayleigh-Plateau instability, such as [26, 58]. Since the Rayleigh-Plateau instability on the long viscous filaments grows from noise, the breakup events are different for all filaments. As a result, this phenomenon cannot be observed stroboscopically. In a numerical model on the other hand, the initial perturbation can be chosen with great precision. Therefore we use a numerical model to validate the linear theory.

The stability of an axisymmetric viscous liquid filament is modeled using the slender jet approximation [8, 46, 29, 38, 45, 40]. For this study we use the previously developed numerical model by Driessen & Jeurissen [40]. In this model the singularities that occur at pinchoff and coalescence, are regularized below a radius that scales with the grid resolution; the influence of the regularization vanishes in the limit of vanishing spatial step size. For this research, this cut-off radius is set at $R_0/30$. The initial condition of the calculation is shown schematically in Fig. 4.1. The grid is moving along with the center of mass of the filament. The filament is considered to be axisymmetric and initially at rest. The perturbation is applied both on the radius and the axial velocity of the jet, using the linearized solution of the Rayleigh-Plateau

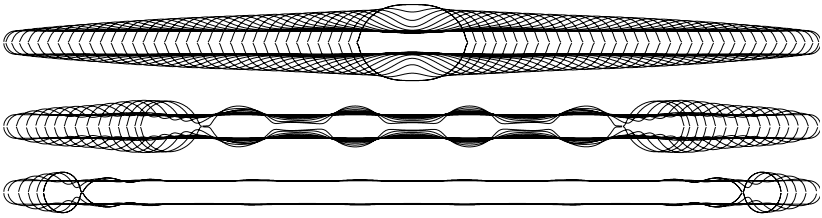

Figure 4.4: Demonstration of the three different regimes, from top to bottom: Stable contraction, breakup due to the Rayleigh-Plateau instability, and breakup due to end pinching. For these numerical simulations, the Ohnesorge numbers are respectively 1, 0.1 and 0.01. The aspect ratio and the perturbation amplitude are kept constant at resp. $\Gamma = 35$ *and* $\epsilon = 0.01$*. The time between the consecutive contours is* t_{cap}*.*

instability [52],

$$R(0,x) = R_0 - \delta \cos\left(\chi_{max}\frac{x}{R_0}\right), \tag{4.11}$$

$$u(0,x) = \frac{2\omega_{max}}{\chi_{max}}\delta \sin\left(\chi_{max}\frac{x}{R_0}\right). \tag{4.12}$$

The radial perturbation is symmetric in the origin, whereas the velocity fluctuation is anti-symmetric. The parameter scan is performed on the regime where the Rayleigh-Plateau instability is expected to dominate the breakup, $15 < \Gamma < 70$ and $0.05 < \mathrm{Oh}_R < 2$. The value for ϵ is 0.01. This value has been chosen such that the result of the linear stability analysis matches with the stability results of the experimental data. Due to the experimental restrictions it is not possible to retrieve the values for ϵ for every separate experiment. Each filament is simulated from t_0 to $t = t_M$. At the latter time, the tail droplets have merged in case of stable contraction. When the filament has broken up at any point in time before the end of the simulation, it is called unstable. The transition between the stable and unstable regime is shown in Fig. 4.3. With the results of the numerical model, it is shown that the stability of a viscous filament can indeed be predicted with linear theory, for a given ϵ.

There are slight differences between the numerical results and the linear theory. Here we explain these deviations qualitatively. At high

viscosity, the numerical results are more stable than the linear theory. We hypothesize that this is due to the influence of the tail droplets on the liquid thread through viscosity. The linear theory assumes that the tail droplets are spherical when they merge. As can be seen in Fig. 4.4, this assumption is inaccurate for high viscous threads. The viscous dissipation that occurs in the tail droplet at low viscosity is smeared out over a larger region of the filament at high viscosity [57]. When these regions overlap, they stabilize the merging. For low viscosity, the numerical model gives a less stable filament, since the capillary waves emitted by the tail droplets destabilize the merging [37]. These capillary waves are not included in the linear theory.

According to [36, 38, 53], one expects that the filament remains stable when $\mathrm{Oh}_R \geq 1$, since end pinching does not occur in that region. This, however, does not mean that a filament with $\mathrm{Oh}_R \geq 1$ is intrinsically stable. A high viscous filament might break up due to the Rayleigh-Plateau instability, as we show here by the linear theory and the numerical model.

4.4 Discussion

As the initial noise amplitude has not been measured directly, δ can only be found indirectly from t_B. It is assumed to be the same for all experiments. To remove this limitation of the analysis, the noise amplitude must be studied with a dedicated setup.

At low viscosities, $\mathrm{Oh}_R \ll 0.1$, the pinchoff resembles the shape of a double cone, in which one side bends back over the other with an internal angle larger than 90^o [59, 60]. This geometry can not be described in the slender jet approximation, which requires the radius to be a single valued function of the axial position. However, resolving this complicated geometry is not necessary to show that the stability of long viscous filaments is determined by Γ, Oh_R and ϵ, which was the objective of this chapter.

4.5 Conclusion

A liquid filament either merges into a single droplet, or breaks up into multiple droplets. Breakup occurs if the aspect ratio Γ is larger than a

critical value, which depends on the Ohnesorge number Oh_R and the relative perturbation amplitude ϵ. We provide a theoretical explanation of the filament stability in the regime of long viscous filaments, based on the Rayleigh-Plateau instability. At low viscosity, $\mathrm{Oh}_R < 0.1$, the critical aspect ratio is small due to end pinching. At higher viscosity, $\mathrm{Oh}_R > 0.1$, end pinching will not occur, but the filament may still break up due to the Rayleigh-Plateau instability. At very high viscosity, $\mathrm{Oh}_L \gg 1$, the filament collapse is stable. The transition to this regime is given by $\Gamma_L = \mathrm{Oh}_R^2$.

5 | Velocity profiles inside piezo-acoustic inkjet droplets in flight: Comparison between experiments and numerical simulations *

Inkjet printing deposits droplets with a well-controlled narrow size distribution. This chapter is aimed at improving experimental and numerical methods for the optimizing of drop formation. We introduce a method to extract the velocity profile inside a single during drop formation. A novel experimental approach is used to capture two detailed images of the very same droplet with a small time delay. By accurately determining the volume from the droplet images the velocity within the droplet can be resolved. The obtained velocity profiles are compared to a numerical simulation based on the lubrication approximation of the Navier-Stokes equation where we find very good agreement.

5.1 Introduction

Inkjet printing is well known for its impressive reproducibility of the drop formation [3, 61, 62]. This has made inkjet printing technology a reliable technique for drop deposition of liquids for broad range of

*To be submitted as: Arjan van der Bos, Mark-Jan van der Meulen, Theo Driessen, Marc van den Berg, Hans Reinten, Herman Wijshoff, Michel Versluis and Detlef Lohse, "Velocity Profile inside piezo-acoustic inkjet droplets: Comparison between experiments and numerical simulations", to Phys. Rev. Appl. The comparison with numerical results is part of this thesis. The experimental work in this chapter was done by Arjan van der Bos, Mark-Jan van der Meulen and Marc van den Berg.

applications [63]. By increasing the deposition accuracy and reducing the droplet sizes, new applications become feasible [64, 65].

Numerical models for free surface flows, e.g. finite element, finite volume and boundary integral methods are used to develop printheads for these applications [19, 9, 66]. One very successful model is the lubrication approximation of the Navier-Stokes equation [8]. It has been shown to be fast and reliable for modelling of drops [8, 46] and sprays [45] and incorporates break-up dynamics and coalescence of the drops (Driessen and Jeurissen [40]). The low CPU time requirements of such a model, which are of the order of minutes on a PC, allows for rapid exploration of a large parameter space in short time.

The experimental validation of the numerical models becomes increasingly challenging [67, 29, 3], as a result of decreasing droplet volumes and high droplet velocities. Visualizing fast inkjet droplets requires ultra-high speed imaging at frame rates exceeding 1 million frames per second [45, 68, 69], or stroboscopic techniques with very short illumination times (< 20 ns) to freeze the motion of the droplets [61, 70, 62]. Even then the results are limited to global estimates such as the overall drop velocity, drop volume and number of satellites. In contrast, numerical models reveal detailed local information on tail formation, velocity development and fluid dynamics throughout the entire drop formation.

In this chapter we present an experimental method that reaches beyond current ones: we will extract the full local and global drop dynamics during the entire formation of a single picoliter droplet. We introduce an advanced imaging technique that provides two snapshot images of the very same droplet with extremely high temporal and spatial resolution. The image pair is analyzed by extracting the contour of the droplet, and subsequently by calculating the volume distribution over the droplet. The velocity inside the droplet is given by the small displacements in the volume distribution over the time between the two recordings.

Our novel method allows for a fully quantitative comparison of the measured drop dynamics with numerical models. Here we compare the experimental data with the results obtained from the lubrication approximation. The volume and velocity distribution obtained from experiment are used as initial condition for the numerical simulation and the time evolution of the droplet then be used to validate the experimental and numerical approach.

5.2 Experimental setup

Figure 5.1 shows a schematic overview of the experimental setup, which consists of four components: printhead, light source, imaging system and the timing control hardware. Figure 5.1 shows a schematic overview of the configuration of the light source and the imaging system.

The inkjet printhead is developed by Océ Technologies [71, 72, 73, 74]. The piezo inkjet printhead consists of 256 similar ink channels with an inverted trumpet shape nozzle with an opening radius of 15 μm. The printhead is distinguished by an extremely reproducible drop formation [71, 3] and has negligible angular distortion. Applying an actuation pulse of 30 V to the piezo actuator results in 11 pl droplets with a final velocity of 4 m/s. Much higher velocities, up to 15 m/s, occur during the formation of the droplet at the meniscus and in the tail of the droplet.

Silicone oil was used in our experiment, which has several advantages. First, the temperature dependence of the viscosity is less than 1%/K, hence the viscosity can be assumed to be constant during the drop formation. Secondly, the surface tension of silicone oil is not easily affected by contamination, hence the surface tension can also be assumed to be constant during the drop formation. The silicone oil that was used is AK10 of Wacker-Chemie GmbH, which has a viscosity of 9.3 mPas, a surface tension of 20.2 mN/m, and a density of 930 kg/m^3.

A dual-cavity Nd:YAG laser (λ = 532 nm, Litron Nano-S) creates a 7 ns laser pulse with high intensity and is coupled into a fluorescent diffuser. The fluorescence light generated in the diffuser remains short (approximately 8 ns) and intense, while both the temporal and spatial coherence have been lost (Bos et al. [75, 76, 77]), making it highly suitable for imaging purposes in the absence of speckle and interference fringes. The residual laser light, which could distort the image or even damage the CCD sensor, is removed with a notch filter. To ensure optimal coupling in to the imaging system, the fluorescence light is collimated with an a-spherical lens such that the numerical aperture closely matches that of the microscope, NA=0.4 [78].

To image the picoliter droplets a microscope is connected to a dual-frame PIV camera (PCO Sensicam QE Double Shutter). The minimum delay between two consecutive images can be set as low as 500 ns. The microscope is an in-line assembly microscope (InfiniTube®) equipped with a 20× objective with a NA of 0.42. This results in an imaging reso-

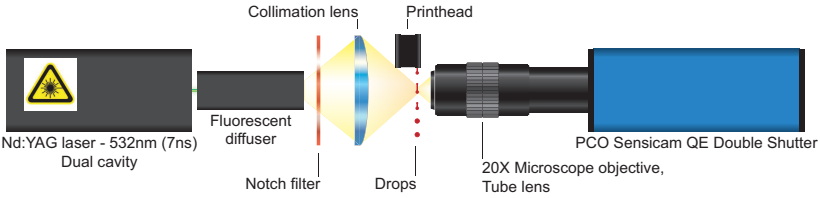

Figure 5.1: In the experimental setup the laser pulse from the Nd:YAG laser illuminates the fluorescent diffuser, which emits a fluorescence light pulse of 8 ns *at high intensity. The fluorescence is focused by an aspherical condenser lens onto the droplets. A notch filter placed between the condenser lens and the droplets prevents any residual laser light from reaching the CCD sensor. The images are recorded using an in-line assembly microscope with a dual frame camera.*

lution of approximately 365 nm/pixel, which is well below the Nyquist criterium for the smallest features in the drop formation [75]. The images are corrected for the pincushion distortion of the imaging objective, using a high-resolution calibration grid. A typical high-quality image obtained with our system is illustrated in figure 5.2, which shows a time series of drop formation.

The timing is controlled by a high-precision delay generator (BNC 575, Berkeley Nucleonics) which triggers the camera, laser, and printhead. The illumination time and the delay between two flashes is verified using a high-speed photodetector (Thorlabs-DET 210) which has a typical rise and fall time of 1.2 ns.

5.3 Experimental methods

5.3.1 High-resolution imaging

The micron-sized droplets move with a velocity of several meters per second, therefore detailed imaging of drop formation in inkjet printing (and in flight) is very challenging. It requires a high degree of spatial and temporal resolution, and is offered by a combination of large numerical aperture high optical quality imaging systems with sensitive high-resolution cameras with a small pixel size to keep magnification

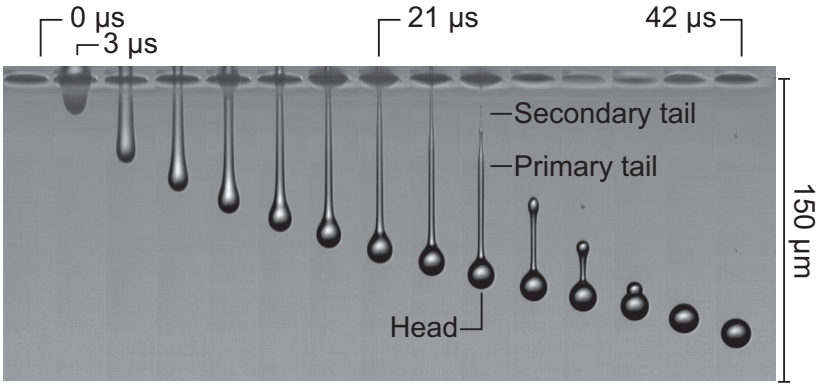

Figure 5.2: Time series of droplets recorded with single-flash photography. From left to right, multiple images of single droplets with a delay of 3 µs between the individual droplets. Here the width of the droplet is 23 µm, the tail is about 4 µm and the secondary tail has a width below 1 µm. The figure illustrates the imaging quality of the setup, and the absence of motion blur due to the use of the 8 ns iLIF illumination.

to a minimum as it may severely distort the image quality. Equally important is the time duration that the CCD sensor is exposed. This time duration can be the exposure time of the camera or, in case of a short flash, the duration of the flash. The exposure needs to be optimized such that sufficient contrast is obtained while minimizing the motion blur. The following criterion is used to calculate the maximal allowable exposure time (τ) [58]:

$$\tau \leq \frac{pixel\ size}{u \cdot M_{eff}}, \tag{5.1}$$

where u is the velocity of the droplet. The spatial resolution of the images is given by the magnification of the optics (M_{eff}) and the pixel size of the CCD sensor. In our experiment the fastest fluid element is displaced with a velocity of 20 m/s. Following equation (5.1) the maximal allowable illumination time is 18 ns. Here we use a flash of approximately 8 ns, thus for the present setup the motion blur is reduced to less than should be less then half a pixel size.

5.3.2 Dual imaging of drop formation in flight

As inkjet printing is extremely reproducible, stroboscopic imaging or single flash imaging would suffice for a statistical analysis. However, the aim is to visualize the internal dynamics during drop formation, which requires at least two images of the very same droplet. Although, it may seem straightforward to use time-resolved high-speed imaging techniques, the time and length scales in this problem would require ultra-high-speed imaging systems running at several million frames per second, e.g. the Brandaris 128 camera [79, 68], with the added complexity of optical configuration, triggering and illumination.

Our approach creates a time series of the entire drop formation by shifting the delay of the flash (t_{drop}) with respect to the start of drop formation. The result of such a stroboscopic technique is very similar to a time series obtained in time-resolved high-speed imaging as a result of the high degree of reproducibility of the inkjet system [69, 68]. Here we add functionality by recording at each time step two consecutive images of one single droplet with the double-shutter camera and the dual-cavity laser. This is done by using a double shutter camera together with a dual cavity laser. It is key to have the delay (τ_f) between the two consecutive images, denoted frame A and frame B, such that lowest possible detectable displacement is obtained. The delay is limited in two ways. First its lower limit is given by hardware limitations of the CCD sensor, 500 ns. And second, the upper limit comes from a fluid dynamical point of view. For the determination of the velocity along the axis of symmetry of the droplet, we assume that the motion is dominated by the inertia of the fluid. To meet this assumption, τ_f must be smaller than the visco-capillary timescale τ_{vc}, given by

$$\tau_{vc} = \frac{\mu R}{\sigma}. \tag{5.2}$$

In the experiments with silicone oil the smallest radius R is approximately 5 μm giving an upper limit for τ_f of approximately ≈ 2 μs.

5.3.3 Image processing

The experimental setup delivers detailed high-resolution images, from which the volume distribution of the droplet is determined. It requires accurate sub-pixel edge detection independent of the contrast of the image. Part of the printhead blocks the illumination, causing an uneven

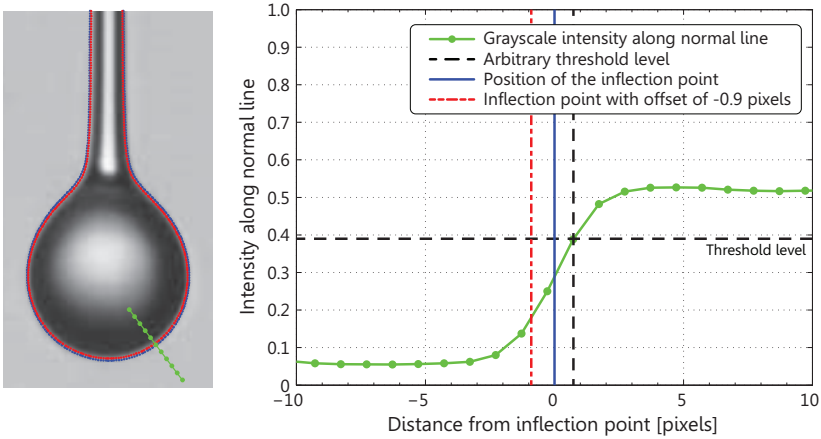

Figure 5.3: Accurate sub-pixel edge detection is required, independent of the contrast in the image. On the left a region of interest of the drop image is shown. First the edge is determined using a standard threshold method (data not shown). From this trace the normal lines along the boundary of the drop are calculated (dotted green line). By calculating the inflection point along the normal lines the intensity independent contour is determined (blue). The red line shows the corrected position of the surface, which is determined by volume conservation arguments, see section 5.3.4. The right part shows the intensity curve along the normal line (green dotted line).

intensity distribution in the images. In addition, the intensity of the light source fluctuates. With standard (fast) edge detection techniques the precise location of the edge is very sensitive to these fluctuations. This problem is solved by using a two-pass edge detection method, illustrated in figure 5.3. The first pass consists of a conventional contour tracing routine (Mathworks Matlab). The second pass determines the intensity curve along the normal of the contour. By calculating the inflection point along these normal lines the intensity independent contour is found.

To verify the validity of this method, a spherical droplet is imaged at a constant delay (t_{drop}) while gradually increasing the background intensity of the image within the dynamic range of the camera. From

each of the images the radius of the droplet is calculated using the proposed method and using conventional contour tracing. Figure 5.4 shows the drop radius for increasing background intensity and it shows that, while the conventional method proves unreliable, our proposed method performs very well over the entire dynamic range of the camera. Only when the background is overexposed the method fails. This method allows for an accurate and intensity-independent contour determination

5.3.4 Droplet volume

From the contours of the droplet the volume of the droplets can be determined, assuming axial symmetry around the central axis of the droplet. The radius, determined in section 5.3.3, is then given by $R(x, t_{drop})$, where x is the axis of symmetry and t_{drop} is the time with respect to the start of the drop formation. The volume of a droplet is calculated by integration over x,

$$V_{drop}(t_{drop}) = \pi \int_{x_0}^{x_{tip}} R(x, t_{drop})^2 dx. \tag{5.3}$$

Here x_0 is the nozzle position and x_{tip} the tip of the drop. Due to the sub-pixel edge detection, the discrete x values are non-equidistant values. We assume that the radius varies linearly over the jet segments with a width smaller then the pixel size. The volume of each segment becomes a truncated cone with finite width of Δx_i (illustrated in figure 5.5), where each cone has a volume

$$v_i = \pi \frac{(r_i^2 + r_{i+1}^2 + r_i\, r_{i+1})}{3} \Delta x_i. \tag{5.4}$$

This gives the total drop volume at time t_{drop},

$$V_{drop}(t_{drop}) = \pi \sum_{i=0}^{i=N} \frac{(r_i^2 + r_{i+1}^2 + r_i\, r_{i+1})}{3} \Delta x_i. \tag{5.5}$$

This method is used to determine the volumes of all droplets in a time series, as shown in figure 5.6. The blue data shows the volume, assuming the physical edge at at the inflection point, as described in the previous section. At $t_{drop} = 60\mu$s the droplet detaches from the

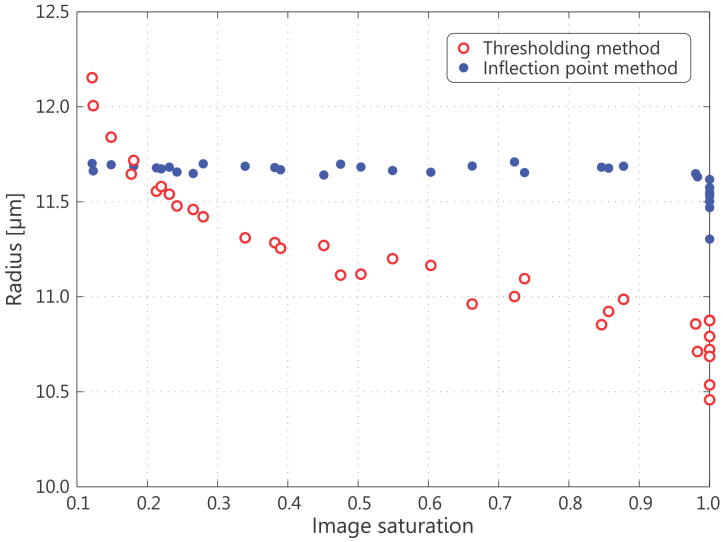

Figure 5.4: A spherical droplet is imaged while gradually increasing the intensity of the illumination over the dynamic range of the camera. The radius is determined both using a thresholding method (○) and by determining the inflection point along the normal lines (●). The radii from the threshold images change by 30% for increasing intensity, while the proposed method shows less than 1% variation. The remaining variation is primarily caused by the residual variation in the reproducibility of the drop formation (as shown in the insert of figure 5.6)

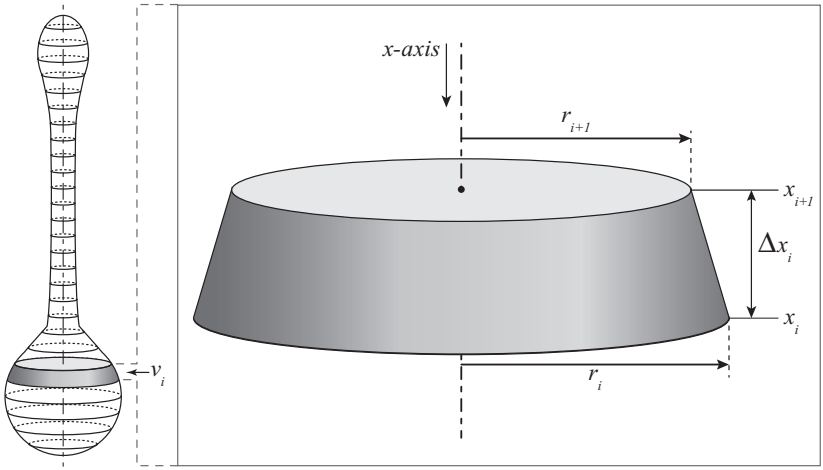

Figure 5.5: For each droplet the contour was determined with sub-pixel accuracy. To calculate the volume distribution the drop is assumed to be axisymmetric. The volume (v_i) of element i of the drop is estimated by truncated cones with radii r_i and r_{i+1} and a height Δx_i

nozzle. After this point in time, the volume of the droplet must remain constant. In figure 5.6 (blue data) however, we see that the volume decreases after the pinchoff from the meniscus. The origin of this overestimation lies in the physical surface not being at the inflection point. To compensate for this inaccuracy, an inward shift of a value of 330 nm with respect to the inflection point along the normal is introduced to the edge detection method. The red data in figure 5.6 confirms the accomplishment of above correction. To confirm that the stability is time independent, the figure displays two full drop evolutions, recorded at different times, displayed on top of each other.

By displaying the volume in frame A against the volumes in frame B over a time series (inset in figure 5.6), it is possible to estimate both the accuracy of the method and the reproducibility of the drop formation. The droplet reproducibility is given by the mean along the axis of unity and for this experiment we find $V_0 = 11.02$ pl. The accuracy of the method (ΔV_{drop}) is given by the perpendicular distance from the linear regression line,

$$\Delta V_{drop} = ||V_{drop}(t)_A - V_{drop}(t)_B||_\infty. \tag{5.6}$$

Here $V_{drop}(t)_A$ is the drop volume at t_{drop} for frame A, and $V_{drop}(t)_B$ is the drop volume of the very same droplet in frame B. After elimination of the outliers we find that the volume fluctuates by $\Delta V \leq 15$ fl, which is less than 0.14%.

5.3.5 Droplet velocity

To determine the velocity within the droplet at time t_{drop} the displacement of the volume elements (v_i) is determined with a Lagrangian method. An image pair is captured for each single droplet; frame A at a drop delay t_{drop} and frame B at $t_{drop} + \tau_f$. Here the time difference between the two frames (τ_f) was set to 600 ns. First, the volume distribution is determined for both frames individually. Then, starting at the tip of the drop, the volume of each element in frame A is mapped to the volume elements in frame B (illustrated in figure 5.7). Here we define $\overline{x}_A(i)$ as the center of mass of the volume element in frame A, and $\overline{x}_B(i)$ as its mapped counterpart. The velocity is then determined by calculating the displacement of the center of mass of each element,

$$U_i = \frac{\overline{x}_A(i) - \overline{x}_B(i)}{\tau_f}. \tag{5.7}$$

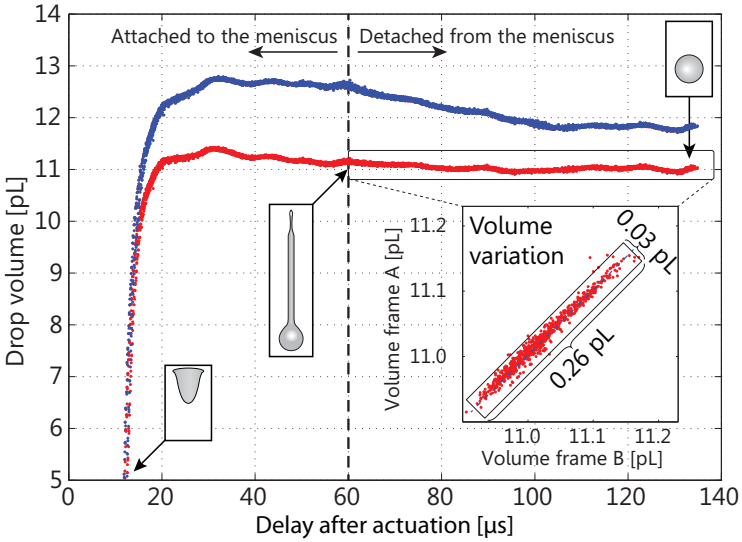

Figure 5.6: The total volume V_{drop} of each ejected droplet, as extracted from the recordings, given as function of the delay time. For each delay the information of two image pairs, i.e. four images, are displayed. The second pair is recorded one full drop formation period after the first to confirm stability at longer timescale. After a delay of 10 µs the meniscus starts moving outward, and at approximately 60 µs the droplets are detached from the meniscus. The blue data gives the uncorrected volume following the inflection point method, while the red point gives volume after correcting using volume conservation. The inlet shows the calculated volume in frame A against the volume in frame B, which illustrates the volume reproducibility ($V_{drop} = 11.02 \pm 0.15$ pl) and the accuracy of the method ($\Delta V_{drop} = \pm 0.015$ pl).

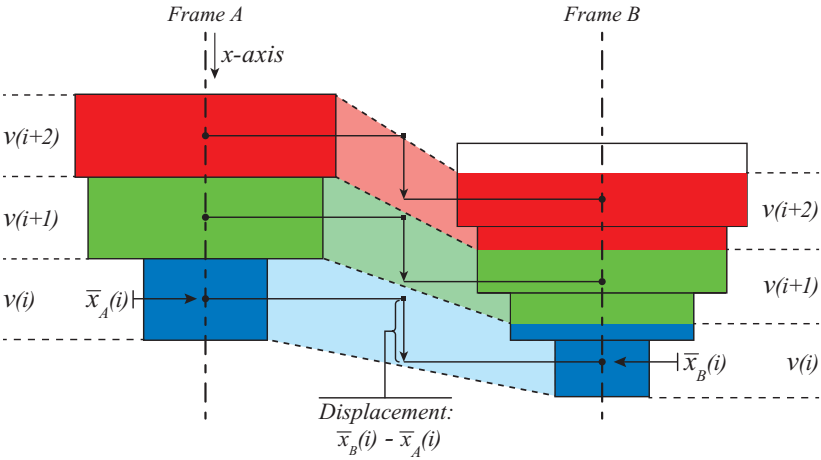

Figure 5.7: The volume distribution is calculated for frames A and B. The volume per element of the first time step is mapped to the volume elements in the second time step. The displacement of the corresponding center of masses divided by the time interval between the recordings gives the mean velocity of the volume elements.

Thus, for a given delay t_{drop}, this method reveals the average velocity U_i of each element $\overline{x}_A(i)$ throughout the droplet. This is illustrated in figure 5.8, where the left part shows the image pair, the middle part shows the volume of the droplets in the image pair, and the right part shows the calculated velocity.

5.4 Validation of the experimental methods

With the velocity and volume distribution known at any given time, we can also simulate the drop formation numerically. For this, the velocity and mass distribution obtained from the experiment are used as initial conditions for the numerical simulation. The drop formation is simulated in a lubrication approximation; a systematic reduction of the Navier-Stokes equations, based on the slenderness of the stretched

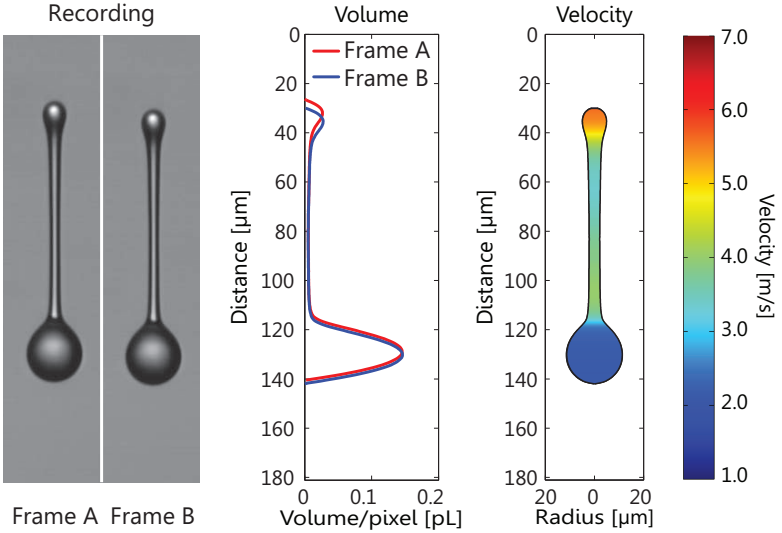

Figure 5.8: The different steps in the experimental procedure. From left to right: a) First two recordings of the same droplet are made, with a delay of 600 ns *between the two frames. b) For both images the volume distribution over the droplet is calculated with sub-pixel accuracy. c) The velocity inside the droplet is determined by calculating the displacement of the volume elements. The velocity is represented by the color scale.*

droplet. It has been shown that this approximation gives accurate results for the evolution of a slender jet [8, 46, 29, 38, 45, 40]. Here the previously developed discretization model by Driessen & Jeurissen [40] is used. In this discretization model the singularities that occur at pinch-off and coalescence are removed by a adding a regularization to the surface tension term. As the regularization scales with the detail of the simulation, its influence vanishes in the limit of an infinitesimal spatial step size.

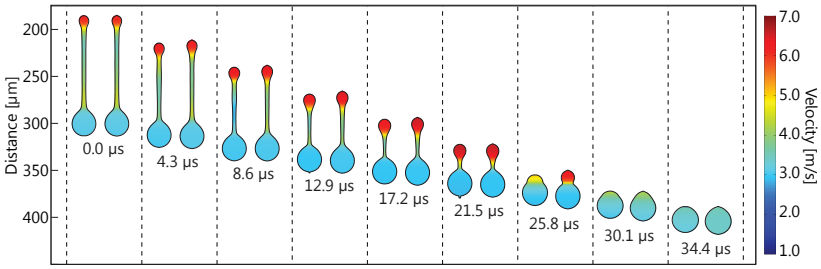

Figure 5.9: Comparison between the experimental and numerical result. At different times, we show both the experimental result (left) and the numerical result (right). The experimental result is obtained from a different droplet each time, whereas the numerical droplet is calculated from the initial volume and velocity distributions from experiment, shown at $t = 0$ µs. The velocity is represented by the color scale.

For the validation two different cases were used. The first case is the evolution of a single droplet under normal jetting conditions, ejected at a droplet-on-demand frequency of 10 kHz. For the start of the numerical simulation, the experimentally obtained velocity and mass distribution, after the drop has detached from the meniscus, were used as initial conditions. Additionally, the density, viscosity and surface tension of the silicone oil were used as input parameters. Figure 5.9 shows the evolution of the droplet for the experiment and the numerical simulation, where we find excellent agreement. The tail droplet merges with the head droplet, and the connecting filament between tail and head remains stable during the entire contraction, i.e. it doesn't break up due to capillary forcing. Also the quantitative agreement of both the

magnitude and distribution of the velocity during the full dynamical process is very good.

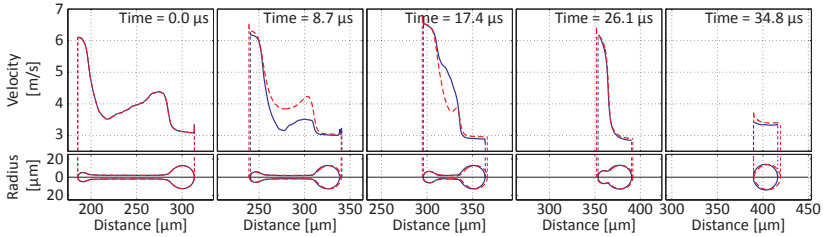

Figure 5.10: Detailed comparison between the experimental result (blue) and the numerical result (dashed red) at five times. The top row shows the velocity distribution, whereas the bottom row shows the volume distribution in time. The experimental and the numerical volume distributions are nearly identical. The Rayleigh-Plateau instability causes the velocity inside the tail to vary from droplet to droplet. During the contraction of the droplet there is very good agreement between the velocities of the head and tail droplet.

To compare the results in more detail figure 5.10 shows the velocity and radius at five different times. For each time step we show the experimental result (solid blue line) and the numerical result (dashed red line). The experimental and the numerical volume distributions are nearly identical. However, there is a small distortion in the velocity in the tail of the droplet over the different experimental results. As the experimental results are obtained from a different droplet each time, the Rayleigh-Plateau instability causes the velocity inside the tail to vary from drop to drop. To support this, we show the experimental data of the stroboscopic recording with a high temporal resolution in figure 5.11. It shows the momentum distribution over the droplet for all drops in the experiment (top) as compared to the numerical result (bottom). The momentum inside the tail droplet increases over time, whereas the momentum inside the cylindrical part of the droplet remains negligible during the complete contraction. Although the droplet volume is highly reproducible according to the volume analysis of figure 5.6, we can see in figure 5.11 that the droplet trajectory slightly varies between the different droplets. This can be observed from

the fluctuating position of the tail droplet, and from the uncorrelated perturbations on the cylindrical part of the contracting droplet.

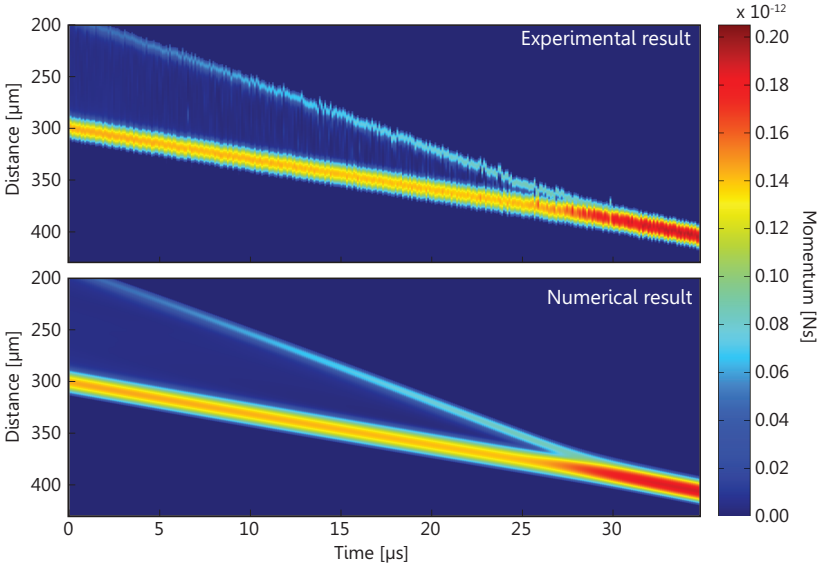

Figure 5.11: The momentum distribution over the droplet for all drops in the experiment (top) and the numerical simulation (bottom). There is a delay of 100 ns *between each subsequent droplet in experiment. In the experimental result it can be seen that the position of the tail and the momentum in the tail vary slightly between different droplets due to the Rayleigh breakup in the tail.*

To demonstrate that the method to determine the velocity also works for separated liquid bodies, we apply it to a second case where two droplets are jetted from the same nozzle with a short time delay in between. The trailing droplet is ejected with a higher velocity, causing the two droplets to collide at approximately 300 μm downstream from the nozzle. Figure 5.12 shows the experimental and the numerical results side by side and again we obtain excellent agreement. We do, however, observe small erratic behavior in the experiments. The momentum distribution as a function of time, displayed in figure 5.13, shows these disturbances more clearly. It shows that the reproducibil-

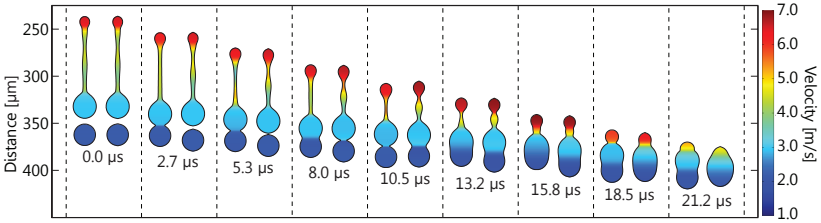

Figure 5.12: Comparison between the experimental and numerical result for a case of colliding droplets. We show the experimental evolution (left) and the numerical results (right) at different times. The numerical droplet evolution is calculated from the experimental volume and velocity distributions at $t = 0$ µs. The color code represents the velocity.

ity of the set of colliding droplets is lower than for the single droplet of the case of figure 5.11. Nevertheless, even for this second case of the colliding droplets the overall agreement is excellent.

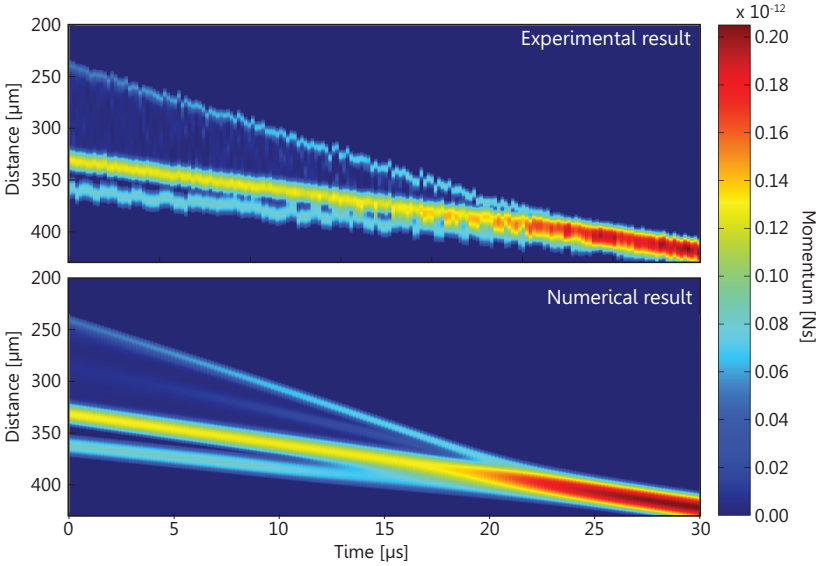

Figure 5.13: The momentum distribution for the colliding droplets in experiment (top) and numerical simulation (bottom) showing overall good agreement but with an apparent lower experimental reproducibility in the droplet behavior.

5.5 Conclusion & Outlook

This work presents a novel method to quantitatively and in flight analyze the internal flow inside the jetted inkjet droplets. Droplets are imaged using iLIF laser-induced fluorescence illumination, with a very short illumination time, allowing for detailed images without motion blur. The images are analyzed and the volume is calculated. The reproducibility of inkjet printing allows for the estimation of the accuracy of the method, where we find an accuracy in the volume estimate of approximately 15 fl. It is a dual frame setup, which records two images of a single droplet, which allows to extract the velocity inside the droplet. Validation of the experimental method with a numerical model shows excellent agreement, confirming the applicability of the method.

The presented method is intended to study drop formation, in order to verify numerical methods and to increase numerical utilization. This method may be extended towards drop formation in jetting of complex fluids with non-Newtonian rheology, quantitatively extracting non-Newtonian parameters from such a comparison.

With two recordings of the same droplet, it is only possible to measure its position and velocity. Technically it would be feasible to expand the setup, such that a series of images of a single droplet are captured at high spatial and temporal resolution. A third recording of the same droplet would in principle already suffice to extract also the acceleration of the fluid. From the acceleration and the contour of the droplet, the forces that act on the liquid can be calculated. The capillary forces can be calculated from the droplet curvature, therefore the local viscosity can be obtained. This method therefore can be used as an extensometer to measure non-Newtonian properties and also ink rheology at high-speeds and high-stretch rates encountered during inkjet drop formation.

6 | Controlling jet breakup by a superposition of two Rayleigh-Plateau-unstable modes*

We experimentally, numerically, and theoretically demonstrate a novel method of producing a stream of widely spaced high-velocity droplets by imposing a superposition of two Rayleigh-Plateau-unstable modes on a liquid jet. The wavelengths of the two modes are chosen close to the wavelength of the most unstable mode. The interference pattern of the two superimposed modes causes local asymmetries in the capillary tension. The velocity of the initial droplets depends on these local asymmetries. Due to their different velocities, the droplets coalesce to produce a stream of larger droplets spaced at a much larger distance than the initial droplets. We analytically derive the perturbations that robustly induce this process and investigate the influence of the non-linear interactions of the two Rayleigh-Plateau-unstable modes on the coalescence process. Experiments and numerical simulations demonstrate that the jet breakup and the subsequent droplet merging are fully governed by the selected modes.

6.1 Introduction

Droplets spawn and perish continuously. The splashing of rain or the generation of aerosols during the breaking of waves are examples of

*Submitted as: Theo Driessen, Pascal Sleutel, Roger Jeurissen, Frits Dijksman, Detlef Lohse, "Controlling jet breakup by a superposition of two Rayleigh-Plateau-plateau-unstable modes", to J. Fluid Mech. The experimental work in this chapter was done in cooperation with Pascal Sleutel.

drop formation in nature. In industry, droplets serve the need for controlled delivery of material. Drop formation is used in the production of powders, where the liquid fraction of the droplets of a suspension is evaporated to obtain a powder [80]. Droplet generators are also used in the dispersion of respiratory medicines, where the droplet size determines where in the lungs the medicines are deposited [11]. In inkjet printing droplets are deposited for graphical purposes or as functional materials [3]. These three examples have in common that the underlying processes can be optimized when the droplet size and spacing are controlled. In this chapter we investigate a method to produce a continuous stream of droplets from a periodically perturbed continuous jet, where we control the size and spacing of the resulting droplets.

Drop formation has been studied for a long time. Savart was the first to report that a continuous liquid jet breaks up into a stream of droplets [50]. Later, Plateau observed that a varicose perturbation of the jet grows if its wavelength is longer than the circumference of the jet [51]. In the literature, a distinction is made between an infinite jet, and a jet that is ejected from a nozzle. The infinite jet with a periodical varicose perturbation is an academic case, used to study the stability of a liquid jet. A jet that is ejected from a nozzle is finite, and ages with the distance it has traveled from the nozzle. Growing perturbations on the ejected jet are not periodic in space. Lord Rayleigh derived the dispersion relation for an infinite jet with a periodical perturbation [4]. Later, he extended the theory by adding viscous effects [6]. In his paper on the instability of a liquid jet ejected from a nozzle, Weber reported a linear approximation for the theory by Rayleigh which has a solution that is almost identical to the original one [52]. In the same paper Weber discussed the influence of air on a laminar jet. Much later, Keller studied the spatial instability of a liquid jet in more detail [81]. Keller derived the complex eigenvalues of the dispersion relation as a function of the Weber number of the jet. He found that when the jet is ejected at high Weber number, the spatial asymmetry of the perturbations that grow on the jet is small. This implies that the growing perturbations on a fast jet move along with the jet, as is the case for growing perturbations on an infinite jet with periodical perturbations. Hence, the spatial growth-rate of a Rayleigh-Plateau-unstable mode on a fast jet is related to the temporal growth-rate by the jet velocity. Mathematically speaking, this is reflected in the feature that the imaginary part of the wavenumber that describes the spatial

instability is small in the case of a high Weber number.

Experiments have shown that the system indeed behaves according to the Rayleigh-Plateau instability analysis. When a periodical perturbation is applied at the nozzle, the jet breaks up according to the theory. A Rayleigh-Plateau-unstable mode can be triggered by different means. Two common perturbation methods are a pressure perturbation inside the nozzle [24], and an undulating electric field around the liquid jet [26]. For the perturbation to be triggered by an electric field, the liquid needs to be conductive. With the pressure perturbation, only the velocity is perturbed. With the electric field on the other hand, only the radius of the jet is perturbed. A perturbation of either the velocity or the radius not immediately results in a single Rayleigh-Plateau-unstable mode, since a single Rayleigh-Plateau-unstable mode consists of a perturbation both in velocity and in radius. A Rayleigh-Plateau-unstable mode has both a growing and a decaying mode at the same wavenumber. When the velocity is directed away from the troughs in the varicose perturbation, the mode is growing. In the decaying mode, the velocity is directed towards the troughs. By simultaneously applying both the growing and decaying mode of the same Rayleigh-Plateau-unstable mode, the resulting jet can have a perturbation either in the radius, or in the velocity alone, depending on the phase difference between the two modes. Garcia and Gonzalez investigated how the different perturbation mechanisms affect the onset of the Rayleigh-Plateau instability [47]. When the perturbation amplitude at the nozzle is small, the decaying mode has a negligible influence on the Rayleigh-Plateau instability [47].

When the perturbation amplitude approaches the jet radius, nonlinear interactions in the perturbation cause satellite droplet formation [82, 23]. The relative size of the satellite droplets increases when the perturbation wavelength increases [24]; experiments show that below a dimensionless wavenumber $kR_0 \approx 0.2$ the volume contained in the satellite droplet is even larger than the main droplet. By adding higher harmonics to the actuation signal, the size and speed of the satellite droplet can be influenced [83, 84]. Another way to reduce or eliminate the satellite droplets is to induce coalescence between multiple main droplets. Orme pioneered this field by using an amplitude modulated (AM) pressure perturbation at the nozzle [85, 86, 87]. The spectrum of the AM signal consists of a carrier frequency and two sidebands. The sidebands are mirrored into the carrier frequency. The fastest growing

Rayleigh-Plateau-unstable mode is chosen as the carrier frequency. The interference of the side bands causes the modulation. The modulation frequency determines the wavelength of the modulation envelope. The droplets in one perturbation envelope merge into one large droplet per modulation envelope.

In this chapter, we present an efficient and robust method to generate a periodic stream of droplets from a continuous jet, in such a way that we are able to precisely control the droplet size and inter-droplet distance. The basic features of the method are introduced in the next section. Section 6.3 is dedicated to the theoretical analysis and we explain the selection of the perturbation wavenumbers and investigate the influence of nonlinear interactions on the initial droplet formation and the final coalescence process. With the theoretical concept known, we then introduce our experimental setup (section 6.4). The technical details of the operation of the setup are given in Appendix 6.A. The numerical scheme is explained in section 6.5. By comparing the experimental results with the results from the numerical analysis, we show that the evolution of the jet into a stream of widely spaced droplets is fully determined by the perturbation signal composed of two sinusoidal perturbations (section 6.6). The chapter ends with conclusions and an outlook (section 6.7).

6.2 The concept

Put in a nutshell, the idea is as follows: We simultaneously impose two sinusoidal perturbations of the pressure drop across the nozzle. These two perturbation modes are chosen such that they are both Rayleigh-Plateau-unstable modes, see figure 6.1. The interference of these two modes causes the droplets to merge into one droplet per shortest common period of the two perturbations. By means of the two small pressure perturbations at the nozzle, we thus control the droplet size and the spacing between the droplets.

The breakup and coalescence resulting from the superposition of the two Rayleigh-Plateau-unstable modes is shown in figure 6.2. This figure shows the breakup and coalescence for three differently chosen combinations of perturbations. To demonstrate the basic idea, we show the numerical results for the case with a constant amplitude in space. The constant amplitude in space allows us to use periodic boundary

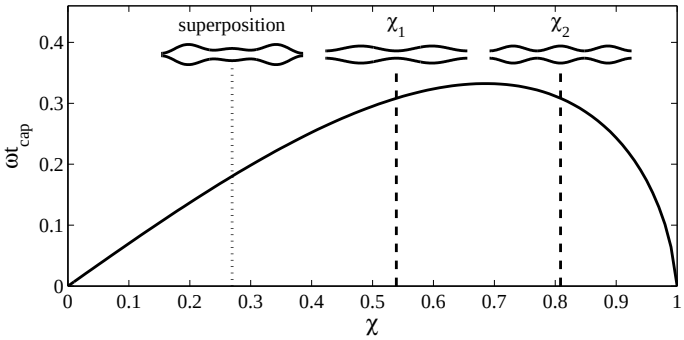

Figure 6.1: The dispersion relation of the Rayleigh-Plateau instability, for We $\gg 1$*, and* Oh $\ll 1$*. The dimensionless growth-rate* ωt_{cap} *is shown versus the dimensionless wavenumber* χ*. The dimensionless wavenumbers* χ_1 *and* χ_2 *represent the different perturbation wavenumbers that we induce on the jet. The contours show their individual radius perturbations. The superposition of mode* χ_1 *and mode* χ_2 *is also shown, at the wavenumber that corresponds to the shortest common period of* χ_1 *and* χ_2*. Since* χ_1 *and* χ_2 *grow equally fast, the shape of the superposition is conserved in the regime where the perturbation amplitude is small compared to the jet radius.*

conditions, with the same periodicity as the perturbation. In this case, the periodic boundary conditions are set at the anti-nodes of the beat signal. Note that the satellite droplets remain stationary at the anti-nodes. In our experiments however, the perturbation grows in space. The jet ages as it moves away from the nozzle, hence the amplitude increases with the distance the jet has traveled. This spatial asymmetry will be discussed in detail in this chapter.

The initial relative amplitude of the two Rayleigh-Plateau-unstable modes is small. In the limit of small amplitudes, we can use a linear model to describe the growth of the Rayleigh-Plateau-unstable modes. The superposition of the two separate perturbations gives the total perturbation, until the amplitude has grown to be of the order of the jet radius R_0. At large amplitudes there are significant non-linear interactions in the perturbation. We will demonstrate the region of validity of the linear approximation and the influence of the non-linear modes on the jet-breakup in detail.

The superposition of the two Rayleigh-Plateau-unstable modes results in a beat signal of the radius perturbation along the jet, and thus also in the difference $R(x,t) - R_0$ between the perturbed jet radius $R(x,t)$ and the unperturbed radius R_0. The perturbation wavelengths are chosen such that the growth-rate of the two modes is equal, hence the beat signal shape is maintained until the non-linear interactions become significant. The jet breaks first at the anti-node of the beat signal, and last at the node of the beat signal. The beat signal causes a difference in radius between the front and the back of a pinching droplet. Since the tension applied by capillarity decreases with the jet radius at the pinch-off location, this difference causes a net force acting on the pinching droplet. Over time, this force accelerates the pinching droplets away from the thinnest point, which is at the anti-node of the beat signal. After pinch-off, all droplets formed between two adjacent anti-nodes move towards the node of the beat envelope. This convergent motion results in coalescence of the small droplets into one large droplet per shortest common wavelength of the perturbations. We call the difference between the breakup time of the jet and the time at which the last small droplet merges the merge time t_{merge}.

With the superposition of two fast growing modes, we have access to small (dimensionless) wavenumbers that otherwise suffer from noise [88] and large satellite droplets [24]. We use the properties of the Rayleigh-Plateau instability to select the wavenumbers for the beat signal. In the

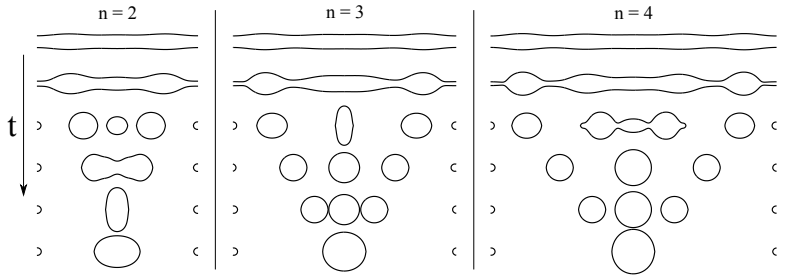

Figure 6.2: A small initial perturbation triggers jet-breakup and subsequent coalescence. The final droplet spacing is given by the shortest common wavelength of the two perturbations. The small perturbation consists of the superposition of two Rayleigh-Plateau-unstable modes. From left to right, the shortest common wavelength of the two perturbations increases. The method used to choose the wavenumbers of the two Rayleigh-Plateau-unstable modes is described in section 6.3.2. From top to bottom we show the different stages in the evolution of one shortest common period of the two Rayleigh-Plateau-unstable modes. The time between the consecutive contours is respectively 5, 20 and 55 times t_{cap}, where $t_{cap} = \sqrt{\rho R_0^3/\sigma}$. The beat signal wavelength is 22.9, 31.8, and 40.8 times R_0 for $n = 2$, $n = 3$, and $n = 4$. Until the breakup, the tips of the ligaments are accelerated by surface tension away from the point where the jet breaks first. The results shown in figure 6.2 have been generated using a numerical model, see section 6.5. For this demonstration, periodic boundary conditions were chosen. At $t = 0$ we impose the two Rayleigh-Plateau-unstable modes. The initial amplitudes of both radial perturbations is 0.005 R_0. The velocity perturbations are set accordingly, see equations (6.5), (6.6), and (6.7).

next section we will explain the wavenumber selection in more detail.

6.3 Analysis

6.3.1 Linear theory

A laminar liquid jet is subject to the Rayleigh-Plateau instability. We demonstrate how the superposition of two Rayleigh-Plateau-unstable modes is employed to achieve a robust drop formation method with a controllable droplet size. The Rayleigh-Plateau instability is approximated in the slender jet approximation [8, 5], which is a systematic reduction of the Navier-Stokes equation for an axisymmetric jet, and which turned out to be extremely valuable in inkjet printing, cf. [45], [89], [90], and [35]. The slender jet approximation in conservative form is given by (cf. [40]),

$$\partial_t A + \partial_x(Au) = 0 \tag{6.1}$$

$$\partial_t(\rho Au) + \partial_x(\rho Au) = \partial_x(\bar{\bar{\sigma}}_\sigma + \bar{\bar{\sigma}}_\mu) \tag{6.2}$$

where $A = A(x,t)$ is the cross sectional area along the jet, $u = u(x,t)$ is the axial velocity along the jet, ρ is the density of the fluid, and $\bar{\bar{\sigma}}_\sigma = \bar{\bar{\sigma}}_\sigma(x,t)$ and $\bar{\bar{\sigma}}_\mu = \bar{\bar{\sigma}}_\mu(x,t)$ are respectively the capillary and the viscous tension. For an axi-symmetric liquid jet, the capillary tension $\bar{\bar{\sigma}}_\sigma$ acting on the jet is given by [91]

$$\tau_\sigma = -\pi\sigma\left(\frac{R}{\sqrt{1+(\partial_x R)^2}} + \frac{R^2\partial_{xx}R}{(1+(\partial_x R)^2)^{3/2}}\right). \tag{6.3}$$

The viscous tension $\bar{\bar{\sigma}}_\mu$ is given by the extensional viscosity in an axisymmetric jet (cf. [8]),

$$\bar{\bar{\sigma}}_\mu = 3\mu A\partial_x u. \tag{6.4}$$

The ratio between the capillary and viscous forces is called the Ohnesorge number $\mathrm{Oh} = \mu/\sqrt{\rho R_0\sigma}$. In our experiments $\mathrm{Oh} = 0.03$, hence for the stability of our jet the capillary effects are dominant. After coalescence however, viscosity plays an important role. When two droplets merge, the excess surface energy causes oscillatory modes on the resulting droplet. Each time another droplet merges with the oscillating droplet, more excess surface energy is added to the oscillating droplet.

Due to the presence of viscosity, this excess energy is dissipated over time. Neglecting viscosity means that the droplet oscillations do not dampen out, which may cause unnatural droplet breakup after coalescence. Therefore, we included $\bar{\bar{\sigma}}_\mu$ in our slender jet approximation model.

In the analysis of a Rayleigh-Plateau instability, the following ansatz for the perturbation is used:

$$R(x,t) = R_0 + R_a \cos(kx)\exp(\omega t), \tag{6.5}$$

$$u(x,t) = u_0 - u_a \sin(kx)\exp(\omega t), \tag{6.6}$$

where u_0 is the unperturbed velocity, R_a and u_a are the initial perturbation amplitudes, k is the perturbation wavenumber, and ω is the growth-rate of the perturbation. From equations (6.1)-(6.2) it follows that the value of u_a is related to R_a by

$$u_a = \frac{2\omega}{k}\frac{R_a}{R_0}. \tag{6.7}$$

As the unstable modes have a wavelength that is longer than the circumference of the jet, the long wavelength approximation is sufficiently accurate for describing the jet evolution [52]. The dispersion relation for the Rayleigh-Plateau instability in the long wavelength approximation is found by substituting the ansatz into the slender jet approximation, equations (6.1)-(6.2), giving

$$\omega = \frac{1}{t_{cap}}\left(\sqrt{\frac{1}{2}(\chi^2 - \chi^4) + \frac{9}{4}\mathrm{Oh}^2\chi^4} - \frac{3}{2}\mathrm{Oh}\chi^2\right), \tag{6.8}$$

where $\chi = kR_0$ is the dimensionless wavenumber and $t_{cap} = \sqrt{\dfrac{\rho R_0^3}{\sigma}}$ is the capillary timescale.

A continuous jet ejected from a nozzle is obviously not an infinite jet. On a continuous jet with a periodical perturbation, both the perturbation amplitude at the nozzle and the breakup length are constant. This implies that the amplitude of the Rayleigh-Plateau instability on a continuous jet grows in space. The spatial growth-rate is governed by the Weber number, which gives the balance between inertia and surface tension, $\mathrm{We} = \rho u_0^2 R_0/\sigma$. Keller showed that the wavenumber is a complex number at low Weber numbers [81]. This implies that when

the spatial asymmetry of the Rayleigh-Plateau instability is large, a growing perturbation also travels over the surface of the jet. In our experiments the Weber number is above 100, hence we can assume that the perturbation grows like on an infinite jet. Mathematically speaking, this means that both the temporal growth-rate and the spatial wave number of the growing instabilities are real valued numbers: The growing perturbations have no velocity relative to the fluid jet.

The amplitude of a Rayleigh-Plateau-unstable mode on a finite jet only grows in space, and the phase travels along with the jet. We rewrite the ansatz for a Rayleigh-Plateau-unstable mode on an infinite cylinder (equations (6.5)-(6.6)) to a Rayleigh-Plateau-unstable mode on a jet ejected by a nozzle:

$$R(x,t) = R_0 + R_a \cos\left(k(x - u_0 t)\right) \exp\left(\omega \frac{x}{u_0}\right), \tag{6.9}$$

$$u(x,t) = u_0 - u_a \sin\left(k(x - u_0 t)\right) \exp\left(\omega \frac{x}{u_0}\right), \tag{6.10}$$

where R_a and u_a are the radius and velocity perturbation at the nozzle, where $x = 0$. At high Weber number the perturbations move along with the jet, and their amplitudes grow with the distance the jet has propagated from the nozzle. As long as the amplitudes of the two Rayleigh-Plateau-unstable modes are small, linear superposition of the two perturbations is justified. The superposition of two Rayleigh-Plateau-unstable modes with different wavelengths leads to an interference pattern with a growing amplitude.

6.3.2 Wavenumber selection

The goal of the method is to obtain a robust stream of droplets, using only a small amplitude perturbation on the pressure drop over the nozzle. In principle, any combination of two different growing modes leads to a beat signal in the radius perturbation, but when the growth-rate of the noise is much higher than that of the applied perturbations, it induces a random fluctuation in the droplet velocities [88]. Therefore, for the selection of the wavenumbers we take the properties of the dispersion relation of the Rayleigh-Plateau instability into account. For a robust stream of droplets, it is important that the signal to noise ratio remains large throughout the entire droplet formation process. When

we carefully select two wavenumbers with equal growth-rates, close to the maximum growth-rate, we can use a very small perturbation amplitude. The energy needed for the coalescence of the droplets is then provided by the available surface energy in the cylindrical jet, which makes the method very efficient.

Using two selection criteria we select the fastest growing combination of wavenumbers for a given shortest common period. The first criterion is that the growth-rate of both modes is equal. In this case, a beat signal applied at the nozzle will grow in amplitude, but maintain its shape until the non-linear interactions emerge. The perturbation amplitudes of both modes will still be the same near pinch-off. When the two perturbations have an equal growth-rate, we can apply them at nearly the same small amplitude to obtain a fully modulated beat signal.

For the stream of droplets to be periodic, the shortest common wavelength of the two superimposed perturbations should be finite. A finite shortest common wavelength is guaranteed when both dimensionless wavenumbers are an integer multiple of the dimensionless base wavenumber, χ_0. The second criterion is given by $(n+1)\chi_1 = n\chi_2$, where n is integer. For any combination of two growing modes with a given shortest common wavelength, this is the combination that has the highest growth-rate for the given shortest common wavelength.

The two selection criteria lead to a unique combination of wavenumbers. For the case of $Oh \ll 1$ this combination is given by:

$$\chi_1 = \frac{\left(\frac{n}{n+1}\right)}{1+\left(\frac{n}{n+1}\right)^2} \tag{6.11}$$

$$\chi_2 = \frac{1}{1+\left(\frac{n}{n+1}\right)^2} \tag{6.12}$$

Since the dispersion relation of the Rayleigh-Plateau instability is concave, the wavenumbers of the two chosen Rayleigh-Plateau-unstable modes approach the wavenumber with the highest growth-rate as n increases.

Figure 6.3: Superposition of two Rayleigh-Plateau-unstable modes on a liquid jet. The linear approximation (dashed line) and the numerical simulation (solid line) agree very well, until the satellite droplets start to form. The Weber number of this jet is 300, the value of $n = 2$. This figure shows that linear superposition of the two perturbations gives a good approximation when the perturbation amplitude is small.

6.3.3 Non-linear interactions

When the amplitude of the Rayleigh-Plateau-unstable modes approaches the jet radius, the non-linear terms emerge in the perturbation spectrum [82]. Taub demonstrated experimentally that the non-linear analysis on an infinite cylinder is valid for a continuous jet with a high Weber number [92], as expected by Keller [81]. To illustrate the validity range of the linear approximation, we show the linear ansatz for the spatial instability equations (6.9)-(6.10) versus a numerical simulation that contains the non-linear terms in figure 6.3. The dimensionless wavenumbers for this comparison are selected for $n = 2$. We obtained the non-linear evolution of the perturbed jet numerically by solving the slender jet approximation in the implementation as explained in [40]. The linear approximation is valid until satellite droplets start to form.

The growth of the beat signal ends with the jet-breakup. As explained in the conceptional section (sec. 6.2) the jet breaks first at the anti-nodes of the beat signal. One by one, the transient droplets break up from the jet, see figure 6.2. Each transient droplet pinches first at the anti-node side, and later at the node side. Orme proposed that this asymmetry results in a net capillary force on the pinching transient droplet, and that the relative velocity of these droplets can be calculated by integrating the capillary forces in the linear approximation during the breakup process [93]. The success of the method depends on the modulation of the beat signal near breakup. The asymmetry that causes the capillary forcing is largest just before pinch-off. We now compare the results, from the full nonlinear model and the linear approximation thereof. This comparison will show that the non-

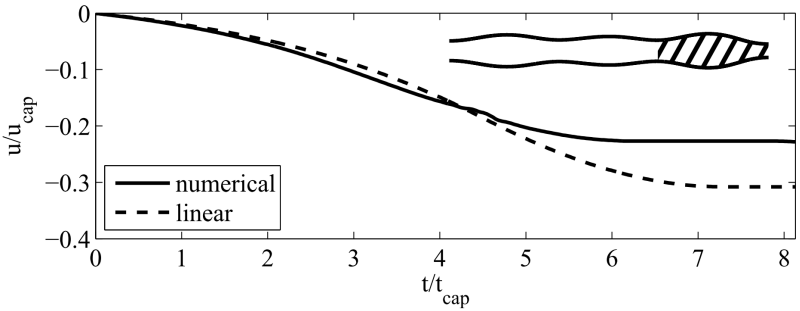

Figure 6.4: Time evolution of the relative velocity u/u_{cap} of a pinching transient droplet, during the final stages of the pinch-off. The Weber number for this jet is 151, i.e. the same as the jet in the later experimental figure 6.8. Also Oh $= 0.03$ *is the same as in experiment. The pinching transient droplet is shown as the shaded part of the jet in the contour in the upper right corner of the graph. The velocity induced by the surface tension (this velocity is relative to the jet velocity) is found by integrating the acceleration caused by the net capillary tension on the pinching transient droplet. For the linear result (dashed line), the ansatz of equations (6.9)-(6.10) is used. For the numerical result (solid line) a simulation is performed with the same initial parameters as for the linear ansatz. In the linear approximation, the integral on the capillary forces results in a relative velocity that is 36% higher (modulo-wise) than the numerical result of the full nonlinear model.*

linear interactions that cause the satellite formation have a significant quantitative influence on the relative velocities of the small droplets.

For this comparison the net capillary forces on the pinching droplets within the full nonlinear model and the (analytical) linear approximation thereof are calculated. For both cases we used the same initial conditions, namely the ansatz for small amplitude perturbations, equations (6.9)-(6.10). The numerical results are obtained with a numerical implementation of equations (6.1)-(6.4), cf. [40]. From equation (6.3) the capillary tension in the axisymmetric liquid jet and also in the formed droplets is known until pinch-off. The last droplet to merge is the droplet next to the anti-node of the beat signal. The merge time

of this last droplet with the rest of the droplets scales inversely with its relative velocity. In figure 6.4 we show the velocity change of the last droplet to merge for both the full nonlinear solution and the linear approximation thereof. The part of volume that will form this droplet is shown as the shaded part of the jet shape. The velocity change of the pinching droplet is determined by integrating the accelerations $a = F/m$ over time, where m is the mass of the pinching droplet, and F is the force due to the capillary asymmetry around the pinching droplet. We assured that we can ignore viscous stresses and the momemtum flux through the edges of the pinching droplet. The result of this integral (figure 6.4) shows that the relative velocity is 36% larger (modulo-wise) within the linear approximation. We thus conclude that the non-linear terms have a significant influence on the final relative droplet velocity. For the comparison with experiments we thus use the full nonlinear (and therefore only numerical) model, rather than the analytical result which we can obtain within the linear approximation.

6.4 Experimental Setup

The continuous liquid jet is ejected from a Microdrop AD-K-501 micropipette. Such a pipette consists of a glass capillary of which the end is shaped like a nozzle. The nozzle radius is $15\,\mu$m. Part of the capillary is surrounded by a tubular piezoelectric actuator. Note that the jet radius R_0 is smaller than the nozzle radius. There are two mechanisms that increase the average velocity after the fluid leaves the nozzle. The main effect is the relaxation of the Poisseuille profile inside the nozzle into a plug flow profile of the jet. A second reason for the contraction is the sinusoidal velocity perturbation, which causes the average momentum-flux to be higher than the momentum-flux of an unperturbed jet [94]. A calibrated Shimadzu LC-20AD HPLC pump supplied degassed micropore filtered water at a constant flow rate. The fluid properties used in the calculations are density $\rho = 1000\,\mathrm{kgm}^{-3}$, surface tension $\sigma = 0.072\,\mathrm{N/m}$, and dynamic viscosity $\mu = 0.001\,\mathrm{Pas}$. All measurements were done in a conditioned room at $20 \pm 0.5\,^{\circ}\mathrm{C}$. For the experiments the flow rate was $Q = 1.00\,\mathrm{ml/min}$ in figure 6.8 and $0.90\,\mathrm{ml/min}$ in figures 6.6, 6.7, 6.9, 6.10, and 6.11. With the piezoelectric element of the micropipette we applied periodic pressure perturbations to the fluid. The electric signals for these perturbations are

supplied by a 40 MHz Wavetek Waveform Generator (Model 195), amplified 50 times with a Falco Systems DC-5MHz High Voltage Amplifier WMA-500. The two sinusoidal signals are generated separately, using an integer number of clock steps to ensure precise setting of the frequencies and the common period, such that no unwanted phase changes occur. The two signals are then summed on a third channel. The technical implementation of the method is discussed in detail in Appendix 6.A.

Since the jet perturbation is periodic, a single flash stroboscopic setup suffices to record the complete jet evolution, see figure 6.5. We used the JetXpert, the drop-in-flight visualization and analysis system from ImageXpert, which is equipped with a Stingray F-080 camera and a blue pulsed LED. The measurement setup is driven such that one image is made at the time. By sweeping the delay between the waveform and the LED trigger over one period of the beat signal, we record the jet evolution at a high temporal resolution.

6.5 Numerical simulations

We use the full nonlinear slender jet approximation (equations (6.1)–(6.4)), to verify that the jet-breakup is indeed fully governed by the two imposed sinusoidal perturbations. The numerical implementation of those model equations was previously developed by some of us [40]. In this approach, the initial conditions at the inlet of the simulations have to be determined from the experimental data. However, we cannot use the data directly at the nozzle. First of all, the distortions directly behind the nozzle are so small that they are hard to experimentally detect. Secondly, close to the nozzle the flow is still influenced by the Poisseuille profile inside the nozzle [47], but in the slender jet approximation plug flow was assumed. Instead of starting the simulations directly at the nozzle, we start the simulations at a location where we can optically detect the perturbations. We call this distance sufficiently far from the nozzle x_{dis}. From that location we can integrate our dynamical model equations (6.1)–(6.4) backwards in space and time, to deduce the initial distortion at the nozzle. We will use this approach in subsection 6.6.1.

In this section, we integrate the dynamical model equations (6.1)–(6.4) forward in space and time, starting from the position x_{dis}, and

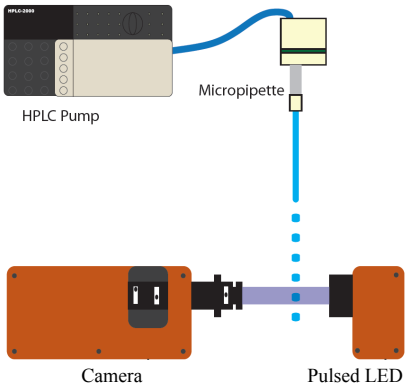

Figure 6.5: Schematic representation of the experimental setup. A continuous jet is emitted through a nozzle at the end of a glass capillary. A pressure perturbation is applied by a piezo electric actuator mounted on the glass capillary. The drop formation is recorded using a camera and a pulsed LED. The drive signal to the LED is coupled electrically to the piezoelectric actuator. By changing the delay time between the signal to the piezoelectric actuator and the LED, the complete evolution of a periodically perturbed jet is recorded.

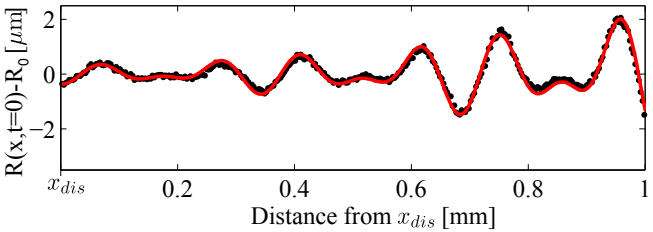

Figure 6.6: The radius perturbation along the jet, obtained from the stroboscopical recordings (black dots). The Weber number of this jet was 107, and $x_{dis} = 1.46\,\text{mm}$. The amplitude and phase of the two perturbations are found with a linear fit (solid red line) to equation (6.15). This linear fit of the complete perturbations is possible in the regime where the amplitude is small compared to the jet radius R_0 and, as seen, describes the experimental data very well.

assuming that the radial and velocity perturbation are linear, according to equations (6.9)–(6.10). These two perturbations are applied simultaneously, both with their own amplitude and phase:

$$\begin{aligned} R(x_{dis},t) = R_0 \quad & -R_{a,1}\cos(u_0 k_1 t - k_1 x_{dis} - \phi_1) \\ & -R_{a,2}\cos(u_0 k_2 t - k_2 x_{dis} - \phi_2) \qquad (6.13) \\ u(x_{dis},t) = u_0 \quad & +u_{a,1}\sin(u_0 k_1 t - k_1 x_{dis} - \phi_1) \\ & +u_{a,2}\sin(u_0 k_2 t - k_2 x_{dis} - \phi_2). \qquad (6.14) \end{aligned}$$

Here $R_{a,1}$ and $R_{a,2}$ are the radial perturbation amplitudes, $u_{a,1}$ and $u_{a,2}$ are the velocity perturbation amplitudes, and ϕ_1 and ϕ_2 are the phases of the two separate Rayleigh-Plateau-unstable modes, all taken at the distance x_{dis} from the nozzle, where the four perturbation amplitudes are already much larger than at the nozzle.

To experimentally determine these parameters, we first determine the jet contour of the recorded jet with sub-pixel accuracy [89]. Note that the contour that we determine in this way, has an a priori unknown offset normal to the real liquid interface. Since the offset is constant in space, we can subtract the average jet radius from the contour, to obtain the beat signal (see figure 6.6). This beat signal is linearized,

$$\begin{aligned} R(x,t=0) - R_0 = {} & R_{a,1}\cos(k_1 x + \phi_1)\exp\left(\omega_1 \frac{x}{u_0}\right) \\ & + R_{a,2}\cos(k_2 x + \phi_2)\exp\left(\omega_2 \frac{x}{u_0}\right), \end{aligned} \qquad (6.15)$$

and the fitting parameters u_0, $R_{a,1}$, $R_{a,2}$, ϕ_1, and ϕ_2 are adjusted to well describe the measured beat signal. The fit is basically indistinguishable from the data itself, see figure 6.6. The remaining parameters R_0, ω_1, ω_2, k_1 en k_2, are dependent on u_0, Q, and the distortion frequencies. Note that in this way R_0 is determined with a much higher precision than optically, simply by employing the relation

$$Q = \pi R_0^2 u_0, \qquad (6.16)$$

as we know the volume flux Q with a very high precision. The whole procedure obviously only makes sense after temporal transients have died out, which we assured.

6.6 Results

We now present our main results, namely that the perturbation of a continuous jet with the two distortion modes chosen according to our scheme (figure 6.1) leads to widely spaced droplets, with a radius much larger than the jet radius. We start this section by first demonstrating that the method indeed works, namely by comparing the experimental and numerical results for $n = 2$. The comparison is performed for two different cases. The first case is characterized by We = 107, the second by We = 151. The differences between these two cases are discussed in the appendix. In section 6.6.2 we use the case for We = 107 for further investigation of the presented method and demonstrate how the droplet size and inter-droplet spacing can be controlled using the presented method. In section 6.6.3 we show, also for the case We = 107, how the phase difference between the two modes influences the coalescence process.

6.6.1 Breakup and coalescence for n=2

First we show the comparison between the experiment and the numerical result of the drop formation for a Weber number of 107. In figure 6.7 the experimentally observed jet is shown together with the numerical simulation thereof. The jet is ejected from the nozzle, and after traveling a distance of 3 mm the jet breaks up in a stream of small droplets. After traveling another 2 mm, the small droplets coalesces into larger droplets, widely spaced by the shortest common wavelength λ_0. After traveling a distance of 3 mm from the nozzle the jet breaks up. The three main droplets merge within 5 λ_0 after the breakup distance. In the numerical simulation the three main droplets merge slightly later than in the experiment. From figure 6.7 we conclude that indeed we succeed to produce large widely spaced droplets with our method, and that experiment and numerical results reasonably agree.

It is interesting to deduce how large the radial and velocity distortions, which lead to the observed distortions at x_{dis} (figure 6.6 and 6.7), were at the nozzle $x = 0$. When we assume that at x_{dis} we are still in the linear regime, we can simply apply equation (6.9) and from our measured values $R_{a,1}(x = x_{dis}) = 0.21\,\mu$m and $R_{a,2}(x = x_{dis}) = 0.15\,\mu$m we obtain the initial distortion $R_{a,1}(x = 0) = 10\,$nm for mode 1, and $R_{a,2}(x = 0) = 7.4\,$nm for mode 2. The radial distortions at the noz-

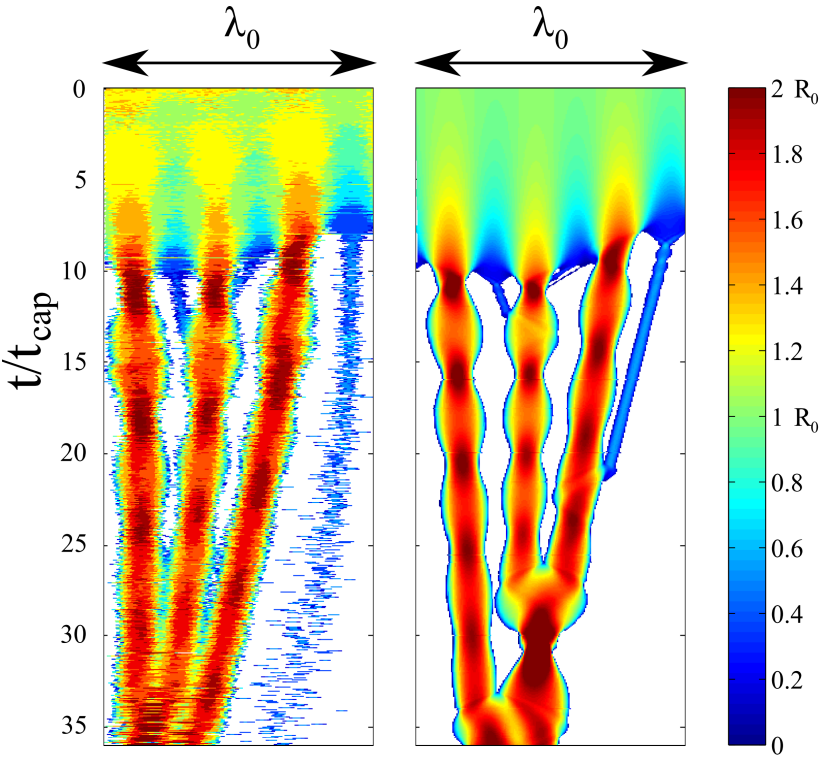

Figure 6.7: Experimental (top) and numerical (bottom) results for a jet (We = 107) *perturbed with two Rayleigh-Plateau-unstable modes for* $n = 2$. *The perturbation frequencies were 133 kHz for mode* χ_1 *and 200 kHz for* χ_2. *For each shortest common period, three main droplets are generated and one satellite droplet. All droplets merge into one big droplet after a short time. The phase and amplitude of the two Rayleigh-Plateau-unstable modes fully determine the breakup of the liquid jet and the coalescence of the resulting small droplets.*

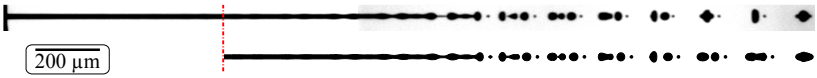

Figure 6.8: Comparison of the experimental (left) and numerical (right) results with the experimental results for n=2. The Weber number for this jet is 151, and the perturbation frequencies for the two perturbations were 162.6 kHz and 243.9 kHz, respectively. The periods of the applied perturbations are integer multiples of the time step of the 40 MHz waveform generator. The values for the phases ϕ_1 and ϕ_2 where 0.23 and -1.44 radians respectively. The data for $R(x,t)$ are shown as a space-time plot, moving along with one common period of the two perturbations. The color shows the radius. In these graphs, the evolution of one common period of the two perturbations is shown, moving along with the jet. First the jet breaks up into main and satellite droplets, later the droplets merge into one droplet per common period. Until after breakup, the experimental and numerical results agree within experimental precision.

zle are indeed very small compared to the jet radius of $R_0 = 14.5\,\mu$m, and clearly not detectable using visible light. The corresponding velocity perturbations at the nozzle follow from equation (6.7) and are $u_{a,1}(x = 0) = 1.8\,$mm/s and $u_{a,2}(x = 0) = 0.87\,$mm/s for mode 1 and 2 respectively, again small, now compared to the jet velocity $u_0 = 22.8\,$m/s.

In figure 6.8, we show the results for the case with We = 151. In the figure we get a detailed view on the growth of the perturbation, the jet-breakup and on the coalescence process. Here we use a space-time plot, moving along with the shortest common period of the perturbations on the jet. The periodicity of the experiment allowed us to use many different recordings of the jet for the construction of this plot. The experimental data for this plot are processed only at a pixel-level accuracy, therefore the color does not match in the initial stages of the comparison. Since the initial conditions for the numerical model are determined at sub-pixel accuracy [89], this does not influence the later stages of the comparison.

Directly after breakup, the position and size of the droplets match

very well. The droplet velocities are slightly different. This results in minor differences in the coalescence process. The three large droplets in the experiment merge simultaneously, whereas the two droplets in the front merge slightly earlier in the numerical result. We believe that the minor differences between the droplet velocities are caused by a small error in the determination of the phases of the different modes. In section 6.6.3 we will show that the droplet velocities are very sensitive to the phase difference between the two signals that form the initial conditions of the simulations.

Summarising this subsection, we conclude that the breakup and merging dynamics of the experiment and the numerical simulation match for both analysed cases $\mathrm{We} = 107$ and $\mathrm{We} = 151$. From this comparison we can conclude that the drop formation is indeed solely governed by the two imposed distortion modes.

6.6.2 Drop size modulation for higher n

The volume of the droplets in the final droplet stream scales with the shortest common wavelength of the two perturbations. When the two wavenumbers approach each other in the k-space, the shortest common wavelength increases. The wavenumbers required for optimal performance of the method were already derived in section 6.3.2. In figure 6.9, we show the jet-breakup and coalescence for the modes $n = 3$, $n = 4$, and $n = 5$. The amplitude and phase of all perturbations are set as explained in appendix 6.A.1. For higher n, the aspect ratio, being the ratio between the merging distance and the nozzle radius, can become very large. This means that it becomes impossible to capture the whole process in one image. We constructed one image of the complete breakup and coalescence process by stitching together recordings at different heights. We have chosen to show the jet breakup and coalescence in the frame of reference of the jet velocity. From top to bottom, the camera shifts with λ_0 away from the nozzle for each next row, while the phase of the perturbations remains fixed. The time between two frames is λ_0/u_0. The jet breakup and coalescence process can be observed in great detail in this way. Note that due to the increase of λ_0 with n, the time between two lines in the figure increases with n.

The fluid motion displayed in figure 6.9 is shown relative to the jet velocity. For all three cases we first observe the jet breakup into main and satellite droplets. Over time, the droplets coalesce into one

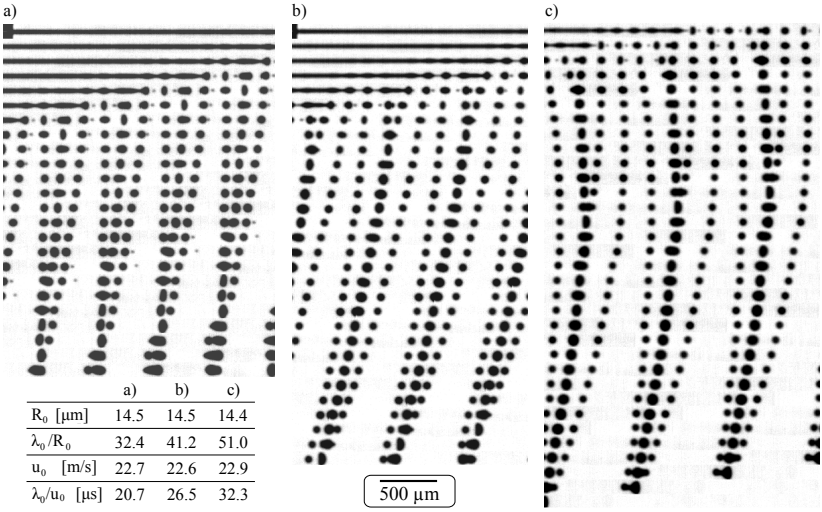

	a)	b)	c)
R_0 [µm]	14.5	14.5	14.4
λ_0/R_0	32.4	41.2	51.0
u_0 [m/s]	22.7	22.6	22.9
λ_0/u_0 [µs]	20.7	26.5	32.3

Figure 6.9: Experimental results for the coalescence dynamics of the transient droplets for modes n = 3, 4, and 5. The Weber number for all three jets was 107. The perturbation periods for mode n = 3, 4, and 5 were: 144.93 kHz & 193.24 kHz, 105.94 kHz & 188.68 kHz, and 155.04 kHz & 186.05 kHz respectively. Note that the periods of all applied perturbations are integer multiples of the time step of the 40 MHz waveform generator. To show the evolution of the breakup and merging, the camera moves along with the jet, at the velocity of the relaxed jet u_0. The time between the consecutive recordings is λ_0/u_0. In order to get this image the phase locked droplet streams were captured at different distances from the nozzle, and then pasted below each other. Small corrections in height were applied, all within the error margin of the linear motor which controlled the nozzle position. The superposition of two Rayleigh-Plateau modes provides a robust method to control the size and the inter-droplet spacing of continuous streams of droplets.

big droplet per shortest common period of the perturbations. As n increases, the merge time increases. In the experiments presented in figure 6.9 the merge time for n = 3, 4, and 5 is 331 μs, 689 μs, and 969 μs, respectively. There are two reasons for this increase: First as the common wavelength becomes longer as n increases, the transient droplets have to travel larger distances. Second, the relative amplitude difference between the local minima near the anti-node of the beat function is smaller. The smaller asymmetry results in a smaller net capillary force on the pinching droplet. Hence these droplets, which have to travel from the anti-node to the node, do this at a smaller velocity for higher n.

As the merge time increases, the influence of air drag becomes significant for the droplet motion. Indeed, for n = 4 and n=5, the curved droplet trajectories in space and time show that the droplet velocities clearly decrease in time, and we attribute this deceleration to the air drag. The curvature of the trajectories of the small droplets is higher, since they are more sensitive to air drag.

6.6.3 Phase dependence

The droplet formation depends strongly on the phase difference between the two perturbations. In figure 6.10 we show the experimental and numerical results of a phase shift between the two modes. We added schematic contours to explain the different phases. Before discussing the results, we first explain how the phase differences are defined. As a result from the wavenumber selection (see section 6.3.2), λ_1 fits n times into λ_0 and λ_2 fits $n+1$ times into λ_0. Therefore, by shifting χ_2 over χ_1 there are $n(n+1)$ possible phases in λ_0 for which the two modes are in phase. The shown phase scan was done for the case $n = 2$, hence there are 6 different phase shifts for ϕ_1 that give the same beat signal. The minimal sector for the phase shift, that contains all possible phase combinations, is $2\pi/6$ from the period of the beat signal. The equivalent in the periodicity of mode χ_1 is two times larger, since χ_1 fits two times in the beat wavelength at $n = 2$. In the experiments of figure 6.10 the phase shift was implemented by setting ϕ_2 to an arbitrary fixed value, and shifting ϕ_1 over a domain of $[0 \dots 2\pi/3]$. The actual phases were determined with the linear fit afterwards. The resulting values of ϕ_1 were shifted with $-\phi_2$, so that the phase difference is given by the value of ϕ_1 alone (ϕ_2 is zero after this shift). For the numerical result,

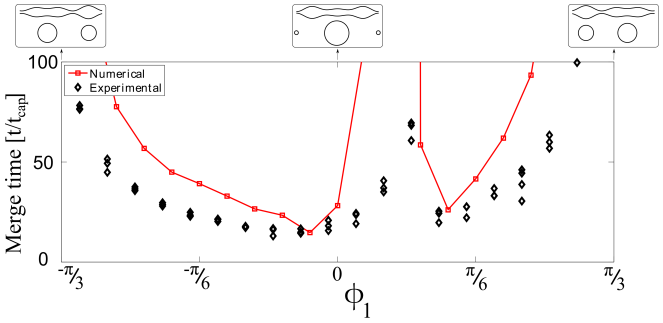

Figure 6.10: The merge time as a function of the phase shift between the two sinusoidal perturbations, determined numerically (□) and experimentally (◊) for mode n = 2. The Weber number was 107. The merge time has two local maxima as a function of the phase difference between the two modes. At $\phi_1 = 0$ the two modes are in phase at a local minimum. In this case, a satellite forms at the anti-node of the beat signal, which travels at the same velocity as the coalesced droplets (see figure 6.2). At $\phi_1 = \pm\pi/3$ the two modes are in phase at a local maximum. In this case, the beat signal has two equal minima per common period. This results in two large droplets that travel at the same velocity. The merge time exceeds 10 000 capillary times close to these phase values. In the experiment, interaction with air inhibits these extremely long merge times. This graph demonstrates that the phase shift can have a large influence on the merge time of the droplets.

we fixed $\phi_2 = 0$ and shifted ϕ_1 over the domain $\phi_1 = [-\pi/3 \ldots \pi/3]$. To compare both results, we show the merge time in the domain of $\phi_1 = [-\pi/3 \ldots \pi/3]$.

The merge time in the numerical result becomes very large for some phase differences. This leads to a huge aspect ratio for which we need to calculate the droplet motions. To shorten the calculations, we assumed that the droplets become spherical after the surface oscillations have dampened out, and that they travel at constant velocity until they coalesce with another droplet. With this extra trick, we only need to solve the nonlinear slender jet equations until all droplets in one λ_0 have broken up from the jet. The merge time was then found using an event-driven hard-sphere coalescence model, where the droplets coalesce when they collide.

The phase scan in figure 6.10 shows that the merge time varies strongly for different phases. There are two phase differences at which the merge time peaks, namely near $\phi_1 = 0$ and near $\phi_1 = \pm\pi/3$. We immediately observe that these peaks are not symmetric around $\phi_1 = 0$. Note that this also holds for the peak around $\phi_1 = \pm\pi/3$, which is less evident from this graph. These asymmetries are caused by the finite Weber number of the jet. As the jet moves away from the nozzle, the perturbation amplitude increases, hence the amplitude of the beat function grows in space. This puts an extra asymmetry over the pinching droplets. In the case of an infinite Weber number, the perturbation amplitude would be constant in space, and growing only in time. In figure 6.2 we have already shown the case of an infinite Weber number, with $\phi_1 = 0$. In the next two paragraphs we explain the physics behind the two peaks in the phase scan. For readability, we ignore the extra asymmetry caused by the finite Weber number for this explanation; it does not play a role to understand the mechanism.

At $\phi_1 = \pm\pi/3$ the two perturbations are in phase at a local maximum. The contours under the graph show that in the case of $\phi_1 = \pm\pi/3$, two large droplets of different size are formed simultaneously, since there are two equal local minima per λ_0. Due to this equal amplitude on both sides of these pinching droplets, there is no net capillary force on the pinching droplets. Their velocities after pinch-off are equal.

At $\phi_1 = 0$, the two perturbations are in phase at a local minimum. This means that there is one global minimum per λ_0, hence from the linear growth we expect all droplets to move away from this global minimum after pinch-off. Due to non-linear interactions however, a

satellite droplet forms at this location. When the two perturbations are exactly in phase, the symmetry around this satellite is not broken, and it does not gain any net velocity from the surface tension. The initial velocity of the merged main droplets and the satellite droplet is the same. From figure 6.2 we can see that the satellite droplet moves at the same velocity as the merged main droplets combined at $\phi_1 = 0$.

An identical initial velocity would mean that the droplets never collide in the absence of air. Hence in the numerical results there are two values for ϕ_1 for which the merge time diverges. The exact values for these two phases depend on the Weber number; they converge to $\phi_1 = 0$ and $\phi_1 = \pm\pi/3$ as $\mathrm{We} \to \infty$. In the experiment however, the merge time is finite due to the interaction with air.

6.7 Conclusion and outlook

The superposition of two Rayleigh-Plateau-unstable modes is an efficient and robust method to generate a periodic stream of droplets, that allows for control of the droplet sizes and distances. The method is efficient because it uses the available surface energy of the continuous jet to induce the coalescence. The method is robust because the wavenumbers of the employed Rayleigh-Plateau-unstable modes are close to the fastest growing mode. By extracting the amplitudes and phases of the two Rayleigh-Plateau-unstable modes from the detailed experimental data and using them as the initial conditions at the inlet of the numerical simulation, we showed that the drop formation is governed by only these two frequencies. The acoustic properties of the device for jet generation and modulation are not needed for the analysis when the images of the drop formation are used to tune the settings of the perturbation signals. By tuning the phase difference between the two modes, the coalescence pattern is controlled. The phase difference with the shortest merge time is not the one for which the two perturbations are in phase at a minimum, due to the presence of satellite droplets. The final droplet size, spacing and merge time increase with the beat number n.

6.7.1 Dropsize modulation for high-speed droplet streams

That it is difficult to generate a steady stream of widely-spaced monodisperse droplets with only *one* Rayleigh-Plateau unstable mode, has two main reasons: Firstly, the growth rate of the long wavelengths is so low that the drop formation can be dominated by noise [88], and, secondly, the relative size of the satellite droplets increases rapidly for increasing perturbation wavelengths [24, 19]. These satellite droplets form an extra nuisance at high Weber numbers, since they tend to travel at approximately the same velocity as the main droplets [95], causing a bi-disperse drop size distribution. By altering the actuation signal, satellite droplets can be prevented, for example by using high amplitude perturbations, or by exciting higher order modes on top of the unstable mode of choice [83].

With the presented droplet size modulation method, it is simple and energetically cheap to prevent satellite droplets. In section 6.6.3 we demonstrate that the phase difference between the two modes strongly influences the velocity of the satellite. This makes it easy to let the satellite quickly merge with the larger droplets. Since the complete drop formation is governed by the two chosen unstable modes, and since the energy needed for the coalescence of the droplets comes from the available surface energy, the presented method is very suitable for droplet size modulation in high-speed laminar fluid jets.

6.7.2 Interaction with air

When comparing the experimental and numerical results, we observed that the interaction with air has an influence on the coalescence pattern of the small droplets. For applications under ambient pressure, it is relevant to quantitatively investigate the interaction between the droplets and the surrounding air. For the ever decreasing droplet size and ever increasing droplet velocity the effect of air drag will become increasingly important.

6.A Experimental implementation of the optimal perturbations

In this chapter we used the results of two different experiments. These two experiments are characterized by their Weber numbers, namely We = 107 and We = 151. We employed different procedures for these experiments. For the experiment with We = 107, the wavenumber selection is optimized for merging time. The experiment with We = 151 has an easier implementation, but gives a longer merging time.

6.A.1 Experiment with We = 107

The success of the method depends on the modulation of the beat signal near breakup. When the two signals have an equal amplitude near breakup, the beat signal is fully modulated there. In that case, the asymmetries that allow the surface tension to pull the droplets away from the anti-nodes of the beat signal are maximized. Since the radius and velocity of the jet are determined with a small experimental error, we do not a priori know if we applied two perturbations with exactly the same growth-rate. Furthermore, we do not know the acoustic and electrical transfer function of the micropipette. These frequency dependent transfer functions may induce extra phase shifts and amplitude differences between the two electrically imposed signals. When the jet velocity and the jet radius are known within experimental precision, we choose the perturbation frequencies according to the procedure explained in section 6.3.2. Using our setup we then tune the amplitude and phase of the two modes to ensure that the amplitudes of the two perturbations are equal near pinch-off, which minimizes the merge time when the two modes are combined.

First we tune the amplitudes of the two perturbations such that both modes have an equal breakup length (figure 6.11). In the experiments presented in this chapter, the difference in breakup length before tuning was generally around one beat signal wavelength λ_0. With the amplitudes matched, the phase of one of the perturbations is changed until the merge time is minimal. A good criterion to find the minimal merge time is when the two outer droplets, coming from the nodes of the beat signal, merge with the large droplet at the anti-node simultaneously.

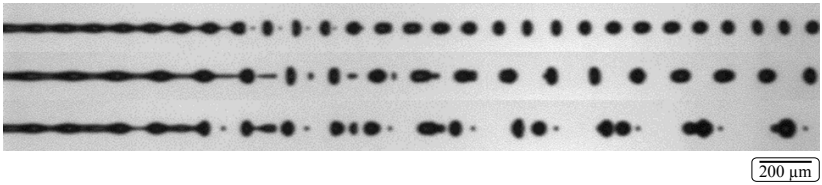

*Figure 6.11: The evolution of the perturbed continuous jet (*We = 107*), for $n = 2$. From top to bottom we show the jet perturbed with the χ_1 mode, the jet perturbed with the χ_2 mode, and a jet perturbed with the superposition thereof. The breakup lengths of the two modes are matched by tuning the actuation voltage of one of the distortions. The phase difference between χ_1 and χ_2 in the superposition of the distortion, is tuned to minimize the merge time. In these recordings, we show perturbed jets after the tuning, hence the separate perturbations from the upper two recordings have the same phase in the lower recording, where the two perturbations are applied simultaneously.*

6.A.2 Experiment with We = 151

In the procedure for the experiment with We = 151, we can choose the perturbation frequencies without knowing the jet velocity. This simplifies the implementation, at the cost of a larger merge time. We start by setting the amplitude of the electrical signal for driving the different modes to an equal voltage. Then we scanned the frequency domain to find two perturbations with a roughly equal breakup length, while obeying the $(n+1)\chi_1 = n\chi_2$ condition exactly. With the frequencies set, the phase of one of the perturbations is changed until the merge time is minimal. A good criterion to find the minimal merge time is when the two outer droplets, coming from the nodes of the beat signal, merge with the large droplet at the anti-node simultaneously.

We determined the values of R_0 and u_0 to find the perturbation wavenumbers a posteriori. With the dispersion relation (equation (6.8)) we then found the growth rates. The growth rate of χ_2 is 10% higher than the growth rate of χ_1 in the experiment with We = 151. The different growth rates imply that the beat signal is not fully modulated during its growth, resulting in a larger merge time then in the case of equal growth rates.

7 | Conclusions and recommendations

In this thesis we studied the stability of axisymmetric liquid bodies. A novel discretization scheme of the hydrodynamic model that describes the stability of an axisymmetric liquid body [6] was implemented. The novel feature of this implementation is the way in which the coalescence and pinchoff singularities are treated. These singular events are regularized by a modification of the capillary force in the model. The new implementation is validated by comparing its results quantitatively to analytical-, numerical-, and experimental results. Here we summarize the main validation cases:

- The model predicts the growth rate of viscous Rayleigh-Plateau instabilities (chapters 2, 6)

- The size of the droplets that result from a Rayleigh-Plateau instability induced breakup agree with experiment and other numerical results (chapters 2, 6).

- The contraction velocity of a liquid filament agrees with other numerical models and a simplified force balance model (chapters 2, 3)

After the validation, we use the numerical model to investigate the dynamics of viscous ligaments that occur in Drop on Demand inkjet printing (chapter 3, 4), and the drop formation resulting from the superposition of two Rayleigh-Plateau-unstable modes (chapter 6).

7.1 Viscous liquid filaments

The axi-symmetric liquid filament is the precursor of the final droplet formation in Drop on Demand inkjet printing. Driven by capillary tension, the filament contracts along its axis of symmetry. In chapter 3 we show that the contraction velocity of a smooth filament with a moderate viscosity is given by the capillary velocity $u_{cap} = \sqrt{\rho R_0/\sigma}$. During this contraction, the filament may break-up into droplets due to capillary instabilities. We found that the critical aspect ratio, above which the filament breaks up before it has contracted, is governed by the Ohnesorge number Oh_R for a given initial perturbation amplitude on the filament ϵ (chapter 4). At low viscosity, $\mathrm{Oh}_R < 0.1$, the critical aspect ratio is small due to end pinching. At higher viscosity, $\mathrm{Oh}_R > 0.1$, end pinching will not occur, but the filament may still break up due to the Rayleigh-Plateau instability. At very high viscosity, $\mathrm{Oh}_L \gg 1$, the filament collapse is stable. The transition to this regime is given by $\Gamma_L = \mathrm{Oh}_R^2$.

For a direct quantitative comparison with experiments, we developed a new experimental method that accurately determines the velocity distribution inside an ink droplet in flight (chapter 5). The droplets are imaged using laser induced fluorescence illumination, with very short illumination time (8 nanoseconds), allowing for detailed images without motion blur. The velocity is determined from the displacement of the volume over the time between two recordings of the very same droplet. To obtain a sufficiently high temporal resolution, we use a dual-cavity laser to excite the fluorescence and a dual-frame PIV camera for the recordings. The obtained velocity profiles agree very well with the results of the numerical simulation with our slender jet model, confirming the applicability of the method.

7.2 Continuous jets

Continuous laminar fluid jets are used in industrial applications to generate monodisperse droplet streams. In this application, a periodical perturbation at the nozzle induces a Rayleigh-Plateau-unstable mode. This unstable mode triggers the jet breakup, that results into a periodic stream of monodisperse droplets. In chapter 6 we present a robust and efficient method to control the droplet size resulting from

a continuous jet, by triggering two Rayleigh-Plateau-unstable modes simultaneously. The method is robust because the wavenumbers of the employed Rayleigh-Plateau-unstable modes are close to the fastest growing mode. The method is efficient because it uses the available surface energy of the continuous jet to induce the coalescence.

With a comparison between experimental and numerical results, we investigate whether the two induced unstable modes govern the complete drop formation process. From experimental data we obtained the phases and amplitudes of the two unstable modes, using the linear ansatz for the two Rayleigh-Plateau-unstable modes. The measured parameters formed the boundary conditions of the numerical simulation. From the good agreement between the simulations and the experiments, we conclude that the drop formation is indeed governed solely by these two frequencies. The final droplet size, spacing and merge time increase with the shortest common wavelength of the two modes.

The phase difference between the two induced unstable modes can have a large influence on the coalescence pattern. When the two distortions are exactly in phase, or exactly out of phase at a local minimum of one of the distortions, the merge time of the droplets can become very large.

7.3 Recommendations

Viscous filaments with high stretch rates

For the study of the stability of the filament, we assumed that the initial axial velocity gradient inside the filament is zero. In Drop on Demand inkjet printing however, the initial velocity gradient inside the liquid jet is very high just after the fluid leaves the nozzle. In our experiments we measured velocity gradients up to $du/dx = 10^6\, s^{-1}$ just after the ejection of the fluid jet, using the method explained in chapter 5. For the study towards understanding the stability of stretching filaments, it would be interesting to make a direct comparison between the recorded evolution of a single droplet, and the numerical simulation thereof.

The technical challenge for this study is to both determine the initial velocity inside the filament, and also record the later evolution of the very same droplet. The recording of the evolution of the very same droplet is necessary because the Rayleigh-Plateau-unstable modes that

cause the breakup of the stretched droplet are uncorrelated between the different droplets. This investigation would require at least a third recording of the same droplet after the first two recordings that give the initial velocity in the filament.

Rheology at high stretch rates

Technically it would be feasible to expand the setup, such that a series of three or more images of a single droplet are captured at high spatial and temporal resolution. A third recording of the same droplet would in principle already suffice to extract also the acceleration of the fluid. From the acceleration and the contour of the droplet, the forces that act on the liquid can be calculated. This implies that the method can be used as an extensometer to measure non-Newtonian properties and ink rheology at high-speeds and high-stretch rates encountered during inkjet drop formation.

Dropsize modulation in high-speed droplet streams

It is difficult to generate a steady stream of widely-spaced monodisperse droplets, using only one Rayleigh-Plateau unstable mode. This has two main reasons. Firstly, the growth rate of the long wavelengths is so low, that the drop formation can be dominated by noise [88], and, secondly, the relative size of the satellite droplets increases rapidly for increasing perturbation wavelengths [24, 19]. These satellite droplets form an extra nuisance at high Weber numbers, since they tend to travel at approximately the same velocity as the main droplets [95], causing a bi-disperse drop size distribution. By altering the actuation signal, satellite droplets can be prevented, for example by using high amplitude perturbations, or by exciting higher order modes on top of the unstable mode of choice [83].

With the presented droplet size modulation method, it is simple and energetically cheap to prevent satellite droplets. As we demonstrated in chapter 6, the phase difference between the two modes strongly influences the velocity of the satellite. This makes it easy to let the satellite quickly merge with the larger droplets.

Since the complete drop formation is governed by the two chosen unstable modes, and since the energy needed for the coalescence of the droplets comes from the available surface energy, the presented method

is very suitable for droplet size modulation in high-speed laminar fluid jets.

Interaction with air

In the comparison of the experimental and numerical results in chapter 6, we observed that the interaction with air has an influence on the coalescence pattern of the small droplets. For applications under ambient pressure, it is relevant to investigate the nature of the interaction between the droplets and the surrounding air.

8 | Summary

In this summary the cohesion between the separate articles, that form the main body of this thesis, is presented. Chapter 2, 3, and 4 of this thesis are a reproduction of [40], [39] and [35] respectively. Chapter 5 is to be submitted to Physics Review Applied and chapter 6 is submitted to the Journal of Fluid Mechanics.

The two main forms of Drop on Demand (DoD) printing are the Thermal- and Piezoelectric actuated inkjet printing. The experimental results for DoD printing in this thesis are generated with a piezo electric printhead. After a piezoelectric actuation, an ink-jet is ejected from the nozzle. When this jet breaks off from the ink in the nozzle, it forms an ink filament that flies towards the paper. In the printing process, the stability of the ink filament is an important factor. Due to the surface tension, the ink filament may contract into one droplet, or break up into multiple droplets. If the filament breaks up too early, several droplets are formed after a single pulse. This results in multiple dots on the print. Therefore, for the quality of the print is essential that the droplet volume and droplet velocity are known a priori. In this thesis we investigate the stability of the liquid filament.

We start the investigation by constructing a model, which accurately describes the dynamics of a liquid filament (chapter 2). For the model that describes the stability of the liquid filament, we apply 4 assumptions: *a*) The filament is an axially symmetric body of Newtonian fluid. *b*) The dynamics of the filament can be described in the slender jet approximation. *c*) The viscosity and the surface tension of the fluid are constant over time and space. *d*) We use the sharp interface approximation for the fluid-air interface. The sharp interface approximation leads to a singularity at pinchoff. The pinchoff singularity is regularized using a modification of the surface tension. This

modification conserves mass and momentum. With this regularization, the model can simulate jet breakup beyond the pinch-off.

The presented numerical model is validated by analytical, experimental and numerical results of the Rayleigh-Plateau instability. The Rayleigh-Plateau instability causes a liquid jet to break-up if the wavelength of the perturbation is longer than the circumference of the jet.

In inkjet printing the behaviour of a liquid filament is especially relevant. It is important that each actuation signal results in a single dot on the substrate. When the filament is unstable, it breaks up, in which case a single actuation results in multiple dots on the substrate. We use the presented numerical model to study the dynamics of liquid filaments. In chapter 3 we show that the speed at which a liquid filament contracts under the capillary tension, can be deduced from the force balance at the end of the cylindrical filament. This is demonstrated by a comparison with our numerical model, with an axi-symmetric implementation of the lattice Boltzmann Method and with a volume of fluid method (Flow3D).

In chapter 4 we extend the study of the contracting filament, by investigating the stability of the filament during its capillary contraction. We show that the stability of a viscous liquid filament can be explained with the Rayleigh - Plateau instability for long filaments, and with end-pinching for low viscous filaments. An important ingredient for this study, is the finite noise amplitude on the initial filament, which is omitted in most of the existing work. Without a finite initial amplitude, the Rayleigh-Plateau instability can not cause the filaments to break up as it was observed in experiments. Furthermore we show in this chapter that the contraction of a liquid filament is not necessarily stable when the Ohnesorge number has a value above 1.

Continuing the study of the liquid filament, we developed a method that can measure the velocity of the fluid inside a DoD generated filament (chapter 5). By recording the very same filament twice, we determine the ink velocity from the fluid displacement between the two recordings. The numerical model that we presented in chapter 2 is used to validate the given ink velocity. From the good agreement between the numerical and experimental results we conclude that the obtained velocity is accurate.

In addition to the study of the stability of ink filaments in Drop on Demand inkjet printing, the numerical model can also be used to look at the break-up of a continuous jet. In chapter 6 we present a robust

and efficient method to control the droplet sizes and spacing resulting from a periodically perturbed jet. At the nozzle we apply two periodical pressure perturbations simultaneously. These perturbations trigger two Rayleigh-Plateau-unstable modes along the jet. The beat function induced by the superposition of the two instabilities, causes the small droplets to merge in to a stream of bigger droplets. The spacing between the final droplets is given by the shortest common wavelength of the two imposed Rayleigh-Plateau instabilities. The presented method is compared with the results of our numerical model, and the agreement between the calculations and experiments shows that the droplet formation is indeed solely governed by the sum of the two signals imposed at the nozzle. We demonstrate that the method works for different shortest common wavelengths, and that the phase difference between the two unstable modes has a large influence on the coalescence process.

9 | Samenvatting

In deze samenvatting wordt de samenhang tussen de verschillende artikelen, die de hoofd-inhoud van dit proefschrift vormen, gepresenteerd. Hoofdstuk 2, 3, en 4 van dit proefschrift zijn een reproductie van respectievelijk [40], [39] en [35]. Hoofdstuk 5 wordt toegestuurd naar Physics Review Applied. Hoofdstuk 6 is toegestuurd aan Journal of Fluid Mechanics.

Bij Drop on Demand (DoD) inkjet printen wordt vloeibaar materiaal met grote nauwkeurigheid gedeponeerd op de gewenste locaties op het substraat. Door de druppels op afroep te genereren, wordt vrijwel alle inkt die door de printkop stroomt gebruikt voor de afdruk. De twee bekendste vormen van DoD printen zijn Thermisch printen en Piëzoelektrisch printen. De experimentele resultaten in dit proefschrift zijn afkomstig van een Piezoelektrisch print systeem. In een piëzo elektrisch print systeem, wordt met een een piëzo elektrisch kristal een drukgolf gegenereerd. In de nozzle wordt de inkt versneld door deze drukgolf, waarna de inkt uit de nozzle spuit. Wanneer de inktstraal van de nozzle afbreekt, hebben we te maken met een vliegende inktsliert. Door de oppervlakte spanning trekt de sliert samen tot een bol. Dezelfde oppervlakte spanning zorgt er echter ook voor dat de sliert opbreekt in losse druppels. Wanneer de inktsliert opbreekt voordat hij het substraat heeft bereikt, zullen er meerdere puntjes op het papier te zien zijn. Voor de kwaliteit van het printproces, is het dus essentieel dat het druppelvolume en de druppelsnelheid onder controle zijn. In dit proefschrift onderzoeken we de druppelvorming in inkjet printen.

We beginnen dit onderzoek door een model te maken van deze druppelvorming 2. In dit model doen we 4 aannames: (a) de vloeistofsliert is een axiaal symmetrisch vloeistof lichaam. (b) beweging in de axiale richting is dominant. (c) De viscositeit en oppervlakte spanning van de

vloeistof zijn constant in tijd en ruimte. (d) De overgang van inkt naar lucht door het oppervlak is abrupt. Deze laatste aanname leidt tot een singulariteit bij het opbreken van de sliert. In ons model wordt deze singulariteit voorkomen door de oppervlakte spanning aan te passen. Ondanks deze aanpassing is het model toch massa en traagheid behoudend. Doordat we de singulariteiten voorkomen, kunnen we het opbreken en samenkomen van axisymmetrische druppels berekenen.

Het gepresenteerde model wordt gevalideerd door de resultaten te vergelijken met analytische, experimentele en andere numerieke resultaten. Hiermee tonen we aan dat het model gebruikt kan worden om de stabiliteit van slierten te voorspellen. In hoofdstuk 2 wordt het model gevalideerd aan de hand van de klassieke Rayleigh-Plateau instabiliteit. De Rayleigh-Plateau instabiliteit veroorzaakt het opbreken van een vloeistofsliert, als de golflengte van de verstoring langer is dan de omtrek van de sliert. Er is veel experimentele en numerieke data beschikbaar voor de Rayleigh-Plateau instabiliteit. Een bijkomend voordeel is dat er een analytische oplossing bestaat voor de Rayleigh-Plateau instabiliteit.

In de praktijk zijn vloeistofslierten niet oneindig lang. Vooral in inkjet printen is het gedrag van een inktsliert met een eindige lengte relevant. In hoofdstuk 3 wordt aangetoond dat de snelheid waarmee een vloeistofsliert samentrekt af te leiden is uit de krachtenbalans aan het eind van de cylindrische sliert. Dit wordt aangetoond middels een vergelijking met het model beschreven in hoofdstuk 2, een axisymmetrische implementatie van de Lattice-Boltzmann methode en het commercieel beschikbare Flow3D. Dit hoofdstuk is interessant omdat er in de literatuur controversie was over deze contractie snelheid.

Om nog een stap dichter bij het begrijpen van de stabilieit van inktslierten in DoD printen te komen, wordt de stabiliteit van verstoorde inktslierten bestudeerd in hoofdstuk 4. De stabilieit van een visceuze cylindervormige sliert blijkt uit te leggen met behulp van de Rayleigh-Plateau instability, en het eind-insnoerings effect. Het feit dat de initiële amplitude van achtergrondruis op de sliert eindig is, blijkt hierbij van essentieel belang. Zonder deze ruis zou de Rayleigh-Plateau instabiliteit, zoals hij geobserveerd wordt in experiment en in simulaties, niet op kunnen treden. Verder wordt in dit hoofdstuk aangetoond, dat het samentrekken van een vloeistofsliert niet per definitie stabiel is wanneer het Ohnesorge getal een waarde heeft boven 1.

Voor het bestuderen van de vloeistofdynamica in een inktdruppel,

is het essentieel om te kunnen zien wat er in de druppels gebeurt. Door de druppels via een microscoop te fotograferen, worden gedetailleerde beelden van de druppels verzameld. De beelden worden kwantitatief geanalyseerd, zodat we op het tijdtip van de foto precies weten waar de inkt zich bevindt. In hoofdstuk 5 presenteren we een nieuwe experimentele methode, die in staat is om de snelheid te meten in een vliegende druppel. Door eenzelfde druppel twee keer vlak na elkaar te fotograferen, kan je uit de verplaatsing van de inkt de snelheid van de inkt in de druppel bepalen. Het numerieke model wat we in hoofdstuk 2 presenteren wordt gebruikt om de bepaalde snelheid te valideren. Voor het experiment wordt gebruik gemaakt van een model vloeistof, zodat alle parameters van de vloeistof bekend zijn. De enige onbekende parameters worden door de beeldverwerking bepaald, en als beginvoorwaarden gebruikt voor het numerieke model. Uit de goede overeenkomsten tussen de numerieke en experimentele resultaten concluderen we dat de experimentele methode goed werkt.

Naast de studie van de stabiliteit van inktslierten in inkjet printen, kan het model ook gebruikt worden om te kijken naar het opbreken van een vloeistofsliert die nog aan de nozzle vast zit. Hierbij komt er een continue straal vloeistof uit de nozzle, welke door middel van een periodieke verstoring tot een periodieke druppelvorming gedwongen wordt. Voor diverse toepassingen is het noodzakelijk dat de druppelgrootte, en de onderlinge afstand tussen de druppels ingesteld kan worden, zonder de nozzle geometrie aan te passen. In hoofdstuk 6 presenteren we een robuste en efficiente methode voor deze toepassing. In onze methode leggen we simultaan twee drukverstoringen op in de nozzle. Deze verstoringen induceren twee Rayleigh-Plateau instabiliteiten op de vloeistofstraal. De interferentie van de twee verstoringen veroorzaken een zweving in de radius, over de lengte van de jet. Door deze zweving zullen groepen van druppels samenkomen. De afstand tussen de uiteindelijke druppels is gegeven door de golflengte van de zweving. De gepresenteerde methode wordt nagerekend met het numerieke model, en uit de overeenkomst tussen de berekeningen en de experimenten concluderen we dat de druppelvorming volledig bepaald wordt door de som van de twee opgelegde signalen. Door het faseverschil tussen de twee signalen te veranderen, kunnen ongewenste satelliet druppels voorkomen worden.

Bibliography

[1] F. C. Krebs. Fabrication and processing of polymer solar cells: A review of printing and coating techniques. *Sol. Energ. Mat. Sol. C*, 93(4):394 – 412, 2009.

[2] R. P. Visconti, V. Kasyanov, C. Gentile, J. Zhang, R. R. Markwald, and V. Mironov. Towards organ printing: engineering an intra-organ branched vascular tree. *Expert Opin. Biol. Th.*, 10(3):409–420, 2010. PMID: 20132061.

[3] H. Wijshoff. The dynamics of the piezo inkjet printhead operation. *Phys. Rep.*, 491(4-5):77 – 177, 2010.

[4] J.W.S. Rayleigh. On the instability of jets. *P. Lond. Math. Soc.*, 1(1):4, 1878.

[5] J. Eggers and E. Villermaux. Physics of liquid jets. *Rep. Prog. Phys.*, 71(3):036601, 2008.

[6] J. W. S. Rayleigh. On the instability of a cylinder of viscous liquid under capillary force. *Philos. Mag.*, 34:145, 1892.

[7] J. Eggers. Nonlinear dynamics and breakup of free-surface flows. *Rev. Mod. Phys.*, 69(3):865–930, Jul 1997.

[8] J. Eggers and T. F. Dupont. Drop formation in a one-dimensional approximation of the navier-stokes equation. *J. Fluid Mech.*, 262:205–221, 1994.

[9] O. A. Basaran. Small-scale free surface flows with breakup: Drop formation and emerging applications. *AIChE Journal*, 48(9):1842–1848, 2002.

[10] W. D. Wu, K. C. Patel, S. Rogers, and X. D. Chen. Monodisperse droplet generators as potential atomizers for spray drying technology. *Dry. Tech.*, 25:1907–1916, 2007.

[11] W. D. Bennett, J. S. Brown, K. L. Zeman, S. C. Hu, G. Scheuch, and K. Sommerer. Targeting delivery of aerosols to different lung regions. *J. Aerosol Med.*, 15(2):179–188, 2002.

[12] R. J. LeVeque. *Numerical methods for Conservation Laws.* Birkhäuser Verlag, 1992.

[13] S. Popinet. An accurate adaptive solver for surface-tension-driven interfacial flows. *J. Comp. Phys.*, 228(16):5838–5866, 2009.

[14] V. Srinivasan, A. J. Salazar, and K. Saito. Numerical simulation of the disintegration of forced liquid jets using volume-of-fluid method. *Int. J. Comp. Fluid. Dyn.*, 24(8):317 – 333, 2010.

[15] A. Jafari, E. Shirani, and N. Ashgriz. An improved three-dimensional model for interface pressure calculations in free-surface flows. *Int. J. Comp. Fluid Dyn.*, 21:87 – 97, 2007.

[16] W. E. H. Sollie, O. Bokhove, and J. J. W. van der Vegt. Space-time discontinuous galerkin finite element method for two-fluid flows. *J. of Comp. Phys.*, 230(3):789 – 817, 2011.

[17] M. P. Brenner, X. D. Shi, and S. R. Nagel. Iterated instabilities during droplet fission. *Phys. Rev. Lett.*, 73(25):3391–3394, 1994.

[18] Ö. E. Yildirim and O. A. Basaran. Dynamics of formation and dripping of drops of deformation-rate-thinning and -thickening liquids from capillary tubes. *J. Non-Newton Fluid Mech.*, 136(1):17 – 37, 2006.

[19] N. Ashgriz and F. Mashayek. Temporal analysis of capillary jet breakup. *J. Fluid Mech.*, 291:163–190, 1995.

[20] Z. D. Skoula, A. G. L. Borthwick, and C. I. Moutzouris. Godunov-type solution of the shallow water equations on adaptive unstructured triangular grids. *Int. J. of Comp. Fluid Dyn.*, 20(621 - 636):16, 2006.

[21] T.A. Kowalewski. On the separation of droplets from a liquid jet. *Fluid Dyn. Res.*, 17(3):121, 1996.

[22] N. N. Mansour and T. S. Lundgren. Satellite formation in capillary jet breakup. *Phys. Fluids A: Fluid Dyn.*, 2(7):1141–1144, 1990.

[23] P. Lafrance. Nonlinear breakup of a laminar liquid jet. *Phys. Fluids*, 18(4):428–432, 1975.

[24] D. F. Rutland and G. J. Jameson. Theoretical prediction of the sizes of drops formed in the breakup of capillary jets. *Chem. Eng. Sci.*, 25(11):1689 – 1698, 1970.

[25] P. Vassallo and N. Ashgriz. Satellite formation and merging in liquid jet breakup. *Proc.: Math. Phys. Sci.*, 433(1888):pp. 269–286, 1991.

[26] H. González and F. J. García. The measurement of growth rates in capillary jets. *J. Fluid Mech.*, 619:179–212, 2009.

[27] M. Tjahjadi, H. A. Stone, and J. M. Ottino. Satellite and subsatellite formation in capillary breakup. *J. Fluid Mech.*, 243:297–317, 1992.

[28] E. P. Furlani and M. S. Hanchak. Nonlinear analysis of the deformation and breakup of viscous microjets using the method of lines. *Int. J. Num. Meth. Fl.*, 2010.

[29] E. D. Wilkes, S. D. Phillips, and O. A. Basaran. Computational and experimental analysis of dynamics of drop formation. *Phys. Fluids*, 11(12):3577–3598, 1999.

[30] J. Eggers. Universal pinching of 3d axisymmetric free-surface flow. *Phys. Rev. Lett.*, 71(21):3458–3460, Nov 1993.

[31] E. Villermaux. Fragmentation. *Ann. Rev. Fluid Mech.*, 39:419–446, 2007.

[32] P. Marmottant and E. Villermaux. Fragmentation of stretched liquid ligaments. *Phys. Fluids*, 16(8):2732–2741, 2004.

[33] N. Bremond and E. Villermaux. Bursting thin liquid films. *J. Fluid Mech.*, 524:121–130, 2005.

[34] F. Veron, C. Hopkins, E. L. Harrison, and Mueller J. A. Sea spray spume droplet production in high wind speeds. *Geophys. Res. Lett.*, 39:L16602, 2012.

[35] T. Driessen, R. Jeurissen, H. Wijshoff, F. Toschi, and D. Lohse. Stability of viscous long liquid filaments. *Phys. Fluids*, 25, 2013.

[36] R. M. S. M. Schulkes. The contraction of liquid filaments. *J. Fluid Mech.*, 309:277–300, 1996.

[37] H. A. Stone, B. J. Bentley, and L. G. Leal. An experimental study of transient effects in the breakup of viscous drops. *J. Fluid Mech.*, 173(1):131–158, 1986.

[38] P. K. Notz and O. A. Basaran. Dynamics and breakup of a contracting liquid filament. *J. Fluid Mech.*, 512:223–256, 2004.

[39] S. Srivastava, P. Perlekar, J. H. M. ten Thije Boonkkamp, N. Verma, and F. Toschi. Axisymmetric multiphase lattice boltzmann method. *Phys. Rev. E*, 88:013309, Jul 2013.

[40] T. Driessen and R. Jeurissen. A regularised one-dimensional drop formation and coalescence model using a total variation diminishing (tvd) scheme on a single eulerian grid. *Int. J. Comput. Fluid D.*, 25(6):333–343, 2011.

[41] L. D. Landau and E. M. Lifshitz. *Fluid Mechanics*. Pergamon, New York, 2nd edition, 1987.

[42] X. Shan and H. Chen. Lattice boltzmann model for simulating flows with multiple phases and components. *Phys. Rev. E*, 47:1815–1819, Mar 1993.

[43] X. Shan and H. Chen. Simulation of nonideal gases and liquid-gas phase transitions by the lattice boltzmann equation. *Phys. Rev. E*, 49:2941–2948, Apr 1994.

[44] X. He and G. D. Doolen. Thermodynamic foundations of kinetic theory and lattice boltzmann models for multiphase flows. *J. Stat. Phys.*, 107(1-2):309–328, 2002.

[45] W. van Hoeve, S. Gekle, J. H. Snoeijer, M. Versluis, M. P. Brenner, and D. Lohse. Breakup of diminutive rayleigh jets. *Phys. Fluids*, 22(12):122003, 2010.

[46] X. D. Shi, M. P. Brenner, and S. R. Nagel. A cascade of structure in a drop falling from a faucet. *Science*, 265(5169):219 –222, July 1994.

[47] F. J. Garcia and H. Gonzalez. Normal-mode linear analysis and initial conditions of capillary jets. *J. Fluid Mech.*, 602:81–117, 2008.

[48] S. Succi. *The Lattice Boltzmann Equation for Fluid Dynamics and Beyond*. Oxford University press, 2001.

[49] J. M. Schneider, N. R. Lindblad, C. D. Hendricks, and J. M. Crowley. Stability of an electrified liquid jet. *J. Appl. Phys.*, 38(6):2599–2605, 1966.

[50] F. Savart. Mémoire sur la constitution des veines liquides lancées par des orifices circulaires en mince paroi. *Ann. Chim.*, 53:337–386, 1833.

[51] J. Plateau. *Statique expérimentale et théorique des liquides soumis aux seules forces moléculaires*. 1873.

[52] C. Weber. Zum Zerfall eines Flüssigkeitsstrahles. *ZAMM*, 11(2):136–154, 1931.

[53] A. A. Castrejón-Pita, J. R. Castrejón-Pita, and I. M. Hutchings. Breakup of liquid filaments. *Phys. Rev. Lett.*, 108:074506, Feb 2012.

[54] J. Eggers and M. A. Fontelos. Isolated inertialess drops cannot break up. *J. Fluid Mech.*, 530:177–180, 2005.

[55] G. I. Taylor. The dynamics of thin sheets of fluid. part iii. disintegration of fluid sheets. *Proc. R. Soc. Lond. A*, 253:313–321, 1959.

[56] F. E. C. Culick. Comments on a ruptured soap film. *J. Appl. Phys.*, 31(6):1128–1129, 1960.

[57] M. P. Brenner and D. Gueyffier. On the bursting of viscous films. *Phys. Fluids*, 11(3):737–739, 1999.

[58] J. A. van der Bos, A. Zijlstra, E. Gelderblom, and M. Versluis. ilif: illumination by laser-induced fluorescence for single flash imaging on a nanoseconds timescale. *Exp. Fluids*, 51:1283–1289, 2011.

[59] R. F. Day, E. J. Hinch, and J. R. Lister. Self-similar capillary pinchoff of an inviscid fluid. *Phys. Rev. Lett.*, 80:704–707, Jan 1998.

[60] J. R. Castrejón-Pita, A. A. Castrejón-Pita, E. J. Hinch, J. R. Lister, and I. M. Hutchings. Self-similar breakup of near-inviscid liquids. *Phys. Rev. E*, 86:015301, Jul 2012.

[61] H. Dong, W. W. Carr, and J. F. Morris. An experimental study of drop-on-demand drop formation. *Phys. Fluids*, 18(7):072102, 2006.

[62] G. D. Martin, S. D. Hoath, and I. M. Hutchings. Inkjet printing - the physics of manipulating liquid jets and drops. *J. Phys. Conf. Ser.*, 105(1):012001, 2008.

[63] H. P. Le. Progress and trends in ink-jet printing technology. *J. Imaging Sci. Techn.*, 42:49–62, 1998.

[64] J. U. Park, M. Hardy, S. J. Kang, K. Barton, K. Adair, Deep K. Mukhopadhyay, C. Y. Lee, M. S. Strano, A. G. Alleyne, J. G. Georgiadis, P. M. Ferreira, and J. A. Rogers. High-resolution electrohydrodynamic jet printing. *Nat. Mater.*, 6(10):782–9, 2007.

[65] S. Mishra, K. L. Barton, A. G. Alleyne, P. M. Ferreira, and J. A. Rogers. High-speed and drop-on-demand printing with a pulsed electrohydrodynamic jet. *J. Micromech. Microeng.*, 20(9):095026, 2010.

[66] S. Gekle, J. Manuel Gordillo, D. van der Meer, and D. Lohse. High-speed jet formation after solid object impact. *Phys. Rev. Lett.*, 102:034502, 2009.

[67] H. Dong, W. W. Carr, and J. F. Morris. Visualization of drop-on-demand inkjet: Drop formation and deposition. *Rev. Sci. Instr.*, 77(8):085101, 2006.

[68] M. Versluis. High-speed imaging in fluids. *Exp. Fluids*, 54:1–35, 2013.

[69] S. T. Thoroddsen, T. G. Etoh, and K. Takehara. High-Speed Imaging of Drops and Bubbles. *Ann. Rev. Fluid Mech.*, 40(1):257–285, 2008.

[70] I. M. Hutchings, G. D. Martin, and S. D. Hoath. High speed imaging and analysis of jet and drop formation. *J. Imaging Sci. Techn.*, 51(5):438, 2007.

[71] J. de Jong, G. de Bruin, H. Reinten, M. van den Berg, H. Wijshoff, M. Versluis, and D. Lohse. Air entrapment in piezo-driven inkjet printheads. *J. Acoust. Soc. Am.*, 120(3):1257, 2006.

[72] J. de Jong, R. Jeurissen, H. Borel, M. van den Berg, H. Wijshoff, H. Reinten, M. Versluis, A. Prosperetti, and D. Lohse. Entrapped air bubbles in piezo-driven inkjet printing: Their effect on the droplet velocity. *Phys. Fluids*, 18(12):121511, 2006.

[73] B. Beulen, J. de Jong, H. Reinten, M. van den Berg, H. Wijshoff, and R. van Dongen. Flows on the nozzle plate of an inkjet printhead. *Exp. Fluids*, 42:217–224, 2007.

[74] R. Jeurissen, A. van der Bos, H. Reinten, M. van den Berg, H. Wijshoff, J. de Jong, M. Versluis, and D. Lohse. Acoustic measurement of bubble size in an inkjet printhead. *J. Acoust. Soc. Am.*, 126(5):2184–2190, 2009.

[75] A. van der Bos, A. Zijlstra, E. Gelderblom, and M. Versluis. iLIF: illumination by Laser-Induced Fluorescence for single flash imaging on a nanosecond timescale. *Exp. Fluids*, 51(5):1283–1289, 2011.

[76] J. W. Shan, D. B. Lang, and P. E. Dimotakis. Scalar concentration measurements in liquid-phase flows with pulsed lasers. *Exp. Fluids*, 36:268–273, 2004.

[77] J. Deppe, D. Michaelis, H. Voges, S. Wissel, and T. Berg. Comparison of particle size and velocity investigations in sprays carried out by means of different measurement techniques. *10th International Conference on Liquid Atomization and Spray Systems*, 2006.

[78] M. W. Davidson and M. Abramowitz. Optical microscopy. *Encyclopedia of Imaging Science and Technology*, 2:1106–1141, 2002.

[79] C. T. Chin, C. Lancée, J. Borsboom, F. Mastik, M. E. Frijlink, N. de Jong, M. Versluis, and D. Lohse. Brandaris 128: A digital 25 million frames per second camera with 128 highly sensitive frames. *Rev. Sci. Instr.*, 74(12):5026–5034, 2003.

[80] H. van Deventer, R. Houben, and R. Koldeweij. New atomization nozzle for spray drying. *Dry. Tech.*, 31(8):891–897, 2013.

[81] Joseph B. Keller, S. I. Rubinow, and Y. O. Tu. Spatial instability of a jet. *Phys. Fluids*, 16(12):2052–2055, 1973.

[82] Man-Chuen Yuen. Non-linear capillary instability of a liquid jet. *J. Fluid Mech.*, 33:151–163, 6 1968.

[83] K. C. Chaudhary and T. Maxworthy. The nonlinear capillary instability of a liquid jet. part 2. experiments on jet behaviour before droplet formation. *J. Fluid Mech.*, 96(02):275–286, 1980.

[84] H. Huynh, N. Ashgriz, and F. Mashayek. Instability of a liquid jet subject to disturbances composed of two wavenumbers. *J. Fluid Mech.*, 320:185–210, 1996.

[85] M. Orme and E. P. Muntz. The manipulation of capillary stream breakup using amplitude-modulated disturbances: A pictorial and quantitative representation. *Phys. Fluids A: Fluid Dyn.*, 2(7):1124–1140, 1990.

[86] G. Brenn and U. Lackermeier. Drop formation from a vibrating orifice generator driven by modulated electrical signals. *Phys. Fluids*, 9(12):3658–3669, 1997.

[87] M. Rohani, F. Jabbari, and D. Dunn-Rankin. Breakup control of a liquid jet by disturbance manipulation. *Phys. Fluids*, 22(10):107103, 2010.

[88] M. Orme. On the genesis of droplet stream microspeed dispersions. *Phys. Fluids A: Fluid Dyn.*, 3(12):2936–2947, 1991.

[89] J. A. van der Bos, M. P. van der Meulen, T. W. Driessen, H. Reinten, M. van den Berg, H. Wijshoff, M. Versluis, and D. Lohse. Velocity profile inside a piezo-acoustic inkjet droplet: Comparison between experiment and numerical simulation. *Submitted*, 2014.

[90] D. T. Papageorgiou and O. Orellana. Study of cylindrical jet breakup using one-dimensional approximations of the euler equations. *SIAM Journal on Applied Mathematics*, 59(1):286–317, 1998.

[91] P.-G. de Gennes, F. Brochard-Wyart, and D. Quere. *Capillarity and Wetting Phenomena*. Springer, 2004.

[92] H. H. Taub. Investigation of nonlinear waves on liquid jets. *Phys. Fluids*, 19(8):1124–1129, 1976.

[93] M. Orme and E. P. Muntz. New technique for producing highly uniform droplet streams over an extended range of disturbance wavenumbers. *Rev. Sci. Instr.*, 58(2):279–284, 1987.

[94] F. Takahashi, W. J. Schmoll, and J. L. Dressler. Characterization of a velocity-modulation atomizer. *Rev. Sci. Instr.*, 65(11):3563–3569, 1994.

[95] W. T. Pimbley and H. C. Lee. Satellite droplet formation in a liquid jet. *IBM J. Res. Develop.*, 21:385–388, 1977.

Acknowledgements

I want to thank Detlef Lohse for having me in the Physics of Fluids group at the University of Twente, from my bachelor assignment until now. I admire how Detlef is able to get the best out of every student. In the Physics of Fluids group, responsibilities are given to those young people who can handle them, allowing them to develop themselves rapidly. Besides the organizational structure he provided, Detlef invested in the translation of my theoretical results into digestible scientific output, either in writing or in presentation. I am grateful for my time at the Physics of Fluids group.

Roger Jeurissen was my mentor from the start of my master thesis onward. He showed me time after time how a new physics problem can be transformed into a solvable problem, by clearly defining the relevant parameters. His involvement in my project was motivated by his genuine interest in the topic of this thesis, and driven by his desire to transmit both knowledge and skill. I am grateful for his dedication to my project.

I want to thank Federioc Toschi for giving me the opportunity to work from Eindhoven, where I first was a guest in the MTP group, and later in the WDY group. In Eindhoven I shared my office with Sudhir Srivastava, who was always ready to discuss research– or politics related topics.

I want to thank Hiprins and Océ for funding my research, and Aart Polderman for organizing the bi-annual meetings of the Hiprins project group. Within this project, I want to thank Jaap van der Vegt, Onno Bokhove and Tatyana Medvedeva for the collaboration on the topic of axi-symmetric jet formation.

I always enjoyed my visits to Océ, where there was always a welcome atmosphere. Thank you Herman, Hans (Reinten and Gollatz), Wim,

Arjan, Bert, and Marc for the nice cooperation over the past five years. I also would like to thank Ramin Badie for his interest in our work, which was inspiring.

It was a delight to visit the Physics of Fluids group in Twente regularly. In this group I found enthusiastic researchers of all ages, trying to figure out the dynamics of the fluids that they are studying. The Journal club and the seminars provided a rich academic atmosphere. The vast inkjet experience of Frits Dijksman, and the discussions with Jacco Snoeijer on surface tension topics were always helpful.

For the experimental work in this thesis, I was dependent on my more practical colleagues, Mark-Jan, Tim, Pascal, Arjan and Marc. Thank you for the nice collaboration.

In the Physics of Fluids group in Twente, I resided in many different offices. I would like to thank all the people that I shared an office with for providing me with good company. I want to put a special thanks to Wolter, for rendering my 1D data to high definition 3D movies. One of these renderings made it to the cover of this thesis.

Thank you Joanita, Brigitte and Marjan for the operational management, Bas Benschop for a working computer and Angelique van Esch for a clean office and a nice chat in the morning.

During the past four years, I worked in different locations, where I met many inspiring people. Thank you Christian, Kundan, Mico, Joost, Hanneke, Tess, Sander, Alvaro, Claas-Willem, Erik-Jan, Oscar, Antonin, Henri, Rianne, Wilco, Raoul, Badr, Altug, Vitor, Florian (Günther and Janoschek), Günes, Sebastian, Mira, Judith, David, Özge, Jemil, Jos, Humberto, Berend, Stefan, Kees, Ariel, Anton, Oleskii, Valentina, Tak, Koen, Rody, Wemke, Jorinde, Laura, Abhineed, and many others.

I want to thank Eefje and the rest of the team for taking me into the Humanitas summer camp staff. The summer camp is another world to me, where scientific progress is utterly irrelevant. Only after this experience, I realized how lucky me and my peers are for growing up in a stable environment with access to basic needs.

And of course, thank you Lionel, Andras, Joost, Siqi, Joan, Alex, Theo and Elea, Tijs and Eliane, Koert and Ksenia, Justin, Jasper and Miriam, Koen and Charlotte, Sjef and Lotte, Balder and Eefje, Iliana and Socrates, Martha and Sobohendra, Aniruddha, Sudhir, Iris and Bastiaan, Danielle and Tom, Julliëtte and Ed, Edwin and Huan, and the old board of v.v. Drienerlo for our culinary get-togethers and other

acts of friendship.

Tijdens mijn promotie was mijn familie een grote steun voor mij. Ik wil speciaal mijn ouders bedanken voor hun (on)geduld, mijn grootouders voor relativeringsvermogen en perspectief, mijn broer en zussen voor hun onvoorwaardelijke steun en de rest van de familie voor hun oprechte interesse.

About the author

Theo Driessen was born on december 14, 1984 in Deurne, to Toon and Ria Driessen – Visser. He enjoyed the classical education at the St. Willibrord Gymnasium in Deurne. In 2003 he joined the University of Twente to study applied physics. For his bachelor assignment he recorded the collapse of laser induced bubbles near a wall in the Physics of fluids group. The image processing of the high speed recordings proved to be a both interesting and fun task. Theo continued his education under the supervision of the Physics of fluids group. During the internship at Mecal in Veldhoven he implemented a model order reduction algorithm for the ANSYS FEM package. He concluded his master research by investigating the drop formation in inkjet printing at Oce. This research was continued during his Phd project. The Phd project resulted in a numerical model that can predict droplet formation from an axi-symmmetric jet. The numerical model, and several applications thereof have been published in scientific journals.